INFLUENCES OF TERRAIN DRIVERS ON ECOSYSTEM DYNAMICS IN A POST-FIRE MOUNTAINOUS ENVIRONMENT: A CASE STUDY IN WATERTON LAKES NATIONAL PARK, CANADA

JESSICA FAITH VAN GAALEN
Bachelor of Science, University of Lethbridge, 2023

A thesis submitted
in partial fulfilment of the requirements for the degree of

MASTER OF SCIENCE

in

GEOGRAPHY

Department of Geography and Environment
University of Lethbridge
LETHBRIDGE, ALBERTA, CANADA

INFLUENCES OF TERRAIN DRIVERS ON ECOSYSTEM DYNAMICS IN A POST-FIRE MOUNTAINOUS ENVIRONMENT: A CASE STUDY IN WATERTON LAKES NATIONAL PARK, CANADA

JESSICA F. VAN GAALEN

Date of Defense: December 15, 2025

Dr. Chris Hopkinson Thesis Supervisor	Professor	Ph.D.
Dr. Laura Chasmer Thesis Examination Committee Member	Associate Professor	Ph.D.
Dr. Ryan MacDonald Thesis Examination Committee Member	Adjunct Professor	Ph.D.
Dr. Brandi Newton Thesis Examination Committee Member	Hydroclimatologist Government of Alberta	Ph.D.
Dr. Craig Coburn Chair, Thesis Examination Committee	Professor	Ph.D.

DEDICATION

To my parents, who have always supported me and fostered my love of the natural world and the mountains since before I could walk.

ABSTRACT

Mountain headwater snowpack is a critical water resource for Southern Alberta, and therefore monitoring changes to environments which support snowpack accumulation is imperative for informing land and water management decisions. Wildfires, such as the 2017 Kenow Wildfire in Waterton Lakes National Park, significantly alter vegetation and hydrological patterns. Post-fire vegetation and snowpack were modeled and monitored using multi-spectral airborne lidar to detect changes in distribution relative to local terrain drivers over time. Multi-scalar monitoring of vegetation regeneration showed that vegetation is significantly recovering at field, drone, and airborne scales of measurement. The vegetation models were stratified by terrain to find that factors such as elevation and local microtopography are influential on regeneration patterns. Snowpack models were also stratified by terrain to find that snowpack depth is greater in burned than in unburned areas, and the snowpack maximum depths shifts upslope as vegetation recovers over time. Quantifying the influences of terrain drivers on early post-fire ecosystem recovery is critical for understanding how ecosystems can be expected to recover under climate change conditions.

CONTRIBUTION OF THE AUTHORS

Chapter 2:

Conceptualization: Chris Hopkinson and Jessica Van Gaalen

Methodology: Jessica Van Gaalen

Data Acquisition: Jessica Van Gaalen, Chris Hopkinson, Laura Chamser, Jesse Aspinall

Validation: Jessica Van Gaalen

Formal analysis: Jessica Van Gaalen, Jesse Aspinall

Resources: Chris Hopkinson

Writing - original draft preparation: Jessica Van Gaalen

Writing - review and editing: Jessica Van Gaalen, Chris Hopkinson

Visualization: Jessica Van Gaalen

Supervision: Chris Hopkinson

Project administration: Chris Hopkinson

Funding acquisition: Chris Hopkinson

Chapter 3:

Conceptualization: Chris Hopkinson and Jessica Van Gaalen

Methodology: Jessica Van Gaalen

Data Acquisition: Jessica Van Gaalen, Chris Hopkinson

Validation: Jessica Van Gaalen

Formal analysis: Jessica Van Gaalen

Resources: Chris Hopkinson

Writing - original draft preparation: Jessica Van Gaalen

Writing - review and editing: Jessica Van Gaalen, Chris Hopkinson

Visualization: Jessica Van Gaalen

Supervision: Chris Hopkinson

Project administration: Chris Hopkinson

Funding acquisition: Chris Hopkinson

Chapter 4: Jessica Van Gaalen:

Author Contributions:

Conceptualization: Chris Hopkinson and Jessica Van Gaalen

Methodology: Jessica Van Gaalen

Data Acquisition: Jessica Van Gaalen, Chris Hopkinson

Validation: Jessica Van Gaalen

Formal analysis: Jessica Van Gaalen

Resources: Chris Hopkinson

Writing - original draft preparation: Jessica Van Gaalen

Writing - review and editing: Jessica Van Gaalen, Chris Hopkinson

Visualization: Jessica Van Gaalen

Supervision: Chris Hopkinson

Project administration: Chris Hopkinson

Funding acquisition: Chris Hopkinson

ACKNOWLEDGMENTS

I am so grateful to all the amazing people who have supported me in this work and writing this thesis. I want to give a huge thank you so my supervisor and mentor Chris, I really appreciate all the great advice and conversations throughout my master's journey. Thank you for the great field adventures and the drone work, you have taught me so much and I am beyond grateful to have been your master's student.

I also want to thank my amazing committee, Laura, Ryan, and Brandi, for your support throughout, for the fantastic suggestions and conversations, your experience and positivity and belief in my work was a huge support to me!

Thank you to my wonderful lab and field team: Celeste, Italo, Emily, Amanda, Jeanne, Natalie, Ben, Jesse, Linda, Taylor, Joe, Farnoosh, Danika, Kattie, Elan, and Brynn, for help with field work, computer assistance, bouncing ideas and good conversations, sharing data, general advice, team support and fellowship and community. It has been such a pleasure working and adventuring with you all!

Thank you to Mom and Dad, my sisters Serena, and Rayla, for listening to me ramble on about lidar and Waterton, and for always supporting and encouraging me. Thank you to my and friends and community at University Drive Alliance Church for listening to my research stories and for your consistent encouragement to me. Finally, and above all, thank you to my Lord and Saviour Jesus Christ for providing for me each day and for your endless grace and love.

TABLE OF CONTENTS

LIST OF TABLES

LIST OF FIGURES

LIST OF ABBREIVIATIONS

aNBR	active Normalized Burn Ratio
ANOVA	Analysis of Variance
CHM	Canopy Height Model
CV	Cameron Valley
DEM	Digital Elevation Model
DS	Dry Site
DSM	Digital Surface Model
GCC	Green Chromatic Coordinate
GNSS	Global Navigation Satellite System
GPS	Global Positioning System
IMU	Inertial Measurement Unit
KW	Kruskal-Wallis Test
LC	Lynx Creek
Lidar	light detection and ranging (also LiDAR in literature)
LSDM	Lidar Snow Depth Model
Masl	Meters above sea level
MS	Moist Site
MW	Mann-Whiteny Test
NDVI	Normalized Difference Vegetation Index
NIR	Near Infrared
NWS	Northwest Site
RGB	Red, Green, Blue
RPAS	Remotely Piloted Aircraft System
SES	Southeast Site
SWE	Snow Water Equivalent
SWIR	Shortwave Infrared
TC	Terrain Curvature
TPI	Topographic Position Index
WCW	West Castle Watershed
WLNP	Waterton Lakes National Park

1. Chapter 1: Introduction: Monitoring Ecosystem Dynamics in a Post-Fire Mountainous Environment

1.1. Water in a Changing Global Climate

Water is critical for supporting life, industry, agriculture, energy production, climate regulation, urban development, and recreation. Protecting this resource is of global importance as the freshwater supply is limited. Snowpack is a significant freshwater source which supplies surface water bodies including reservoirs, lakes, and rivers (Black, 1991; Koshkin et al., 2022). Depending on the global region, snowpack supplies between 20% and 80% of the available freshwater for downstream use (Koshkin et al., 2022; Maxwell & Clair, 2019; Pomeroy & Gray, 1995). Seasonal snowpack accumulates over the winter in mountain headwater regions and melts in the spring, recharging water storage locations. Since water is critical to maintaining functioning ecosystems and societies, it is important to understand how mountain snowpack headwaters change in environments impacted by different environmental phenomena, including climate change and wildfire.

Anthropogenic climate change is the phenomenon of increasing average global temperatures resulting from the addition of excess greenhouse gases (GHGs) to the atmosphere. These GHGs, such as carbon dioxide and methane, increase the "greenhouse effect" because the gases trap longwave radiation that would otherwise exit the atmosphere, resulting in an increase of global temperatures (Keeling, 1970; Koshkin et al., 2022; Lapp, 2002; MacDonald, 2008; Springer et al., 2015). This has widespread impacts, including increasing the frequency and intensity of wildfires (Giovando & Niemann, 2022; Maxwell & Clair, 2019; McGrath et al., 2023; Niemeyer et al., 2019) by increasing occurrences of 'fire weather', which describes weather conditions which are

hot and dry for an extended period, often combined with high wind speeds (Ellis et al., 2022; Jain et al., 2024; Jain et al., 2022).

These fires, in combination with higher global average temperatures, can reduce snowpack accumulation and advance peak snowmelt timing, shifting the expected hydrographs for a given region and potentially reducing the quantity and quality of freshwater (Gersh et al., 2022; Smoot & Gleason, 2021; Springer et al., 2015). Increasing occurrences of wildfire creates a positive feedback loop because fires release stored carbon, increasing global temperatures, which further dries fire fuels, which continue to increase the occurrence of fires (Koshkin et al., 2022).

Mountain environments can be heavily impacted by wildfire, as the fires can remove vegetation from an area, influencing the hydrology of the watershed. Naturally occurring wildfires of low intensity can promote new growth and allow for nutrient cycling (Lentile et al., 2006), but high intensity fires can burn organic soils, understory layers, and canopy cover (Gerrand et al., 2021). When vegetation is removed, the hydrology significantly changes because vegetation and water interactions are critical for water flow pathways in watersheds. Vegetation intercepts incoming precipitation, preventing excessive overland flow (Jean Louis & Hiatt, 2025). Interception also reduces the velocity of rain drops, reducing soil erosion, and increasing evapotranspiration (Williams et al., 2019). Root systems facilitate infiltration to groundwater resources including the unsaturated zone and the water table, and the photosynthetic reactions increases evapotranspiration (Bladon et al., 2014; Burles & Boon, 2011; Davis, 2012; Silins et al., 2009). Vegetation is also important in determining snow distribution, which is critical for water supply and runoff timing (Pomeroy, Gray, et al., 1998). Maximum snow depth occurs approximately at treeline on mountain slopes because of the

combination of greater volumes of precipitation at higher elevation and the snow trapping effect (Cartwright, 2018; Hopkinson et al., 2012). The snow trapping effect is when snow cannot move downslope from wind or gravity, due to the presence of vegetation (Cartwright, 2018). Snow that has low water content is highly mobile in the wind, and therefore the snow can be redistributed following the initial snowfall (Barnes & Hopkinson, 2022b; Vionnet et al., 2021). As the snow is redistributed, it is often caught in the needles or leaves of vegetation (Pomeroy & Gray, 1995; Pomeroy, Gray, et al., 1998). Additionally, vegetation can act as a wind breaker, and therefore the snow is trapped in areas with thick vegetation and starts to form drifts. High elevation areas, while they tend to be colder, promoting more snow precipitation, also have reduced vegetation. Often, these high elevation areas also experience high wind speeds, promoting snow redistribution, pushing the snow downslope, where it is trapped by the vegetation(Cartwright et al., 2020). When vegetation is removed from mountain slopes, it is expected that the snow will shift downslope because there is reduced vegetation to catch the mobile snow, however, this pattern has not been previously quantified.

Since snow is important in hydrological systems, studying how snow distribution and depth are impacted by changes in post-fire regions is critical to understanding water resources. One way of studying and measuring changes in snow and vegetation is to use remote sensing technology, such as light detection and ranging (lidar; (Bares & Hopkinson, 2022a; Hopkinson, Sitar, et al., 2004)). This active remote sensing technology allows for continuous mapping of ground surface elevation, vegetation structural characteristics, and when non-snow-covered elevation is available, snow depth. These measurements allow for mapping over the same area in consecutive years for analysis of spatiotemporal changes (Hopkinson et al., 2024). Measuring the changes in

mountain snowpack due to fire is challenging due to limited site accessibility and potential hazards in mountainous environments, including rapidly changing weather conditions and remote communications. Additionally, it is difficult to measure the full range of variability of snow depth using field data collection methods. However, these mountain systems are important because they supply much of western Canada's water and support ecosystems. The main objective of this thesis is to analyze changes in early-stage post-fire vegetation recovery and snowpack dynamics relative to the terrain in a mountain valley environment, specifically in the Cameron Valley (CV) of Waterton Lakes National Park (WLNP) in Alberta, Canada.

1.2. Vegetation and Snowpack in the Canadian Rockies

The Canadian Eastern Slopes of the Rocky Mountains (Figure 1.1) extend from the prairie ecozone to the alpine ecozone and support a wide diversity of vegetation species. Some of these species include grasses such as crested wheat grass (*Agropyron cristatum*) and rough fescue (*Festuca scabrella*), five-needle conifers including white-bark pine (*Pinus albicaulus*) and limber pine (*Pinus flexilis*), and other conifers such as lodgepole pine (*Pinus contorta),* subalpine fir (*Abies lasiocarpa),* and Engelmann spruce (*Picea engelmannii*) (Kuijt, 1982). Vegetation communities are influenced by various factors including soil type, moisture, climate, and topography (Andrus et al., 2018; Odum, 1969). Water availability is important in determining the type of vegetation and growth locations. For example, vegetation that grows in the alpine regions is better adapted to colder temperatures, exposure to sun and wind, limited quantities of soils and therefore limited nutrients and water, and very short growing seasons (McCaffrey, 2018; Odum, 1969). In the valley, the area is sheltered from the wind, and the growth seasons are slightly longer due to warmer temperatures resulting from lower elevations (Brockway,

1998; Day et al., 1989). Additionally, increased soil depth at lower elevation can increase water availability and nutrient availability. These factors among other can support increased species diversity, tree height, and biomass volume in the lower elevation zones (Brockway, 1998). Therefore, within a few kilometers of distance and a few hundred meters of elevation, the vegetation species and structure can vary significantly.

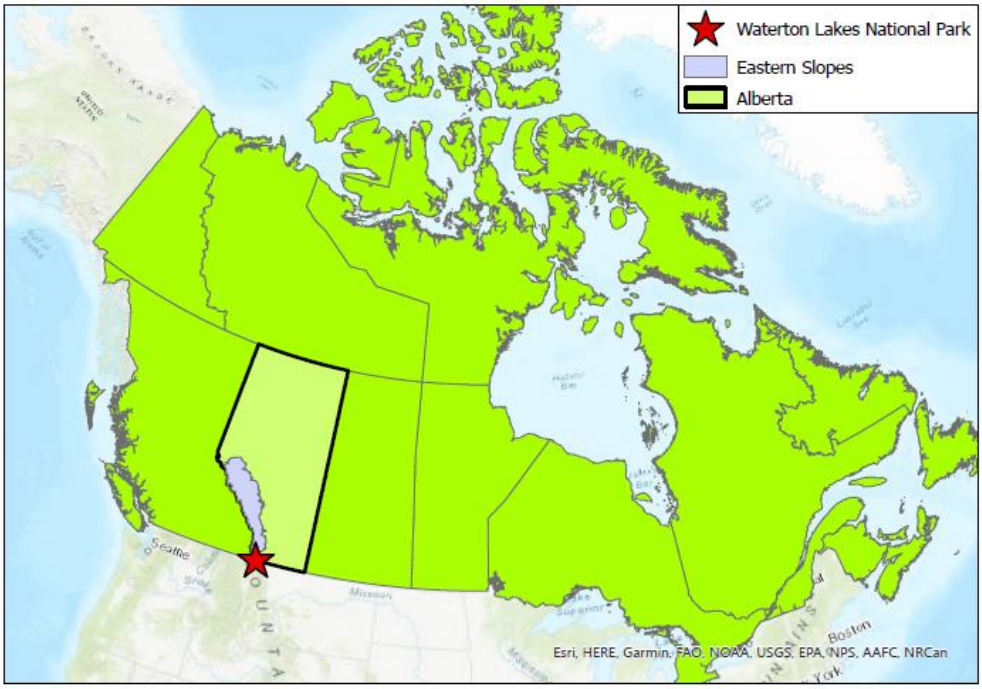

Figure 1.1 : The location of the Eastern Slopes of the Canadian Rocky Mountains in Alberta, highlighting the location of Waterton Lakes National Park.

In mountain environments, a substantial portion of the available water is supplied by seasonal snowpack accumulation (Grünewald et al., 2010; Oldman Watershed Council, 2023). Measuring water fluxes is important for predicting water resources downstream. Precipitation is the main input into a water system, and in Canadian Rockies, precipitation is highly seasonal, with most occurring as snowfall in the winter months between November and March (Barnes et al., 2025; Williams et al., 2019). In the summer, there is significantly more evapotranspiration (ET) than in the winter due to increased temperatures and greater leaf surface area (Black, 1991). Soil moisture in the vadose zone

is important to supporting vegetation, because as water percolates through the soils, it is pulled towards the root systems (Krzic et al., 2021).

Roots absorb a significant amount of water to support photosynthetic processes in vegetation. Vegetation tends to lower the water table and allow the soil to accept more water via infiltration and percolation Additionally, vegetation creates friction in many processes, slowing hydrological flow pathways. For example, vegetation intercepts significant proportions of rain and snow, slowing the speed of precipitation hitting the ground, increasing evaporation and sublimation (Black, 1991). The remaining overland flow that does not evaporate or percolate into groundwater resources flows eventually into a surface water body such as a river or lake. Overland flow includes water moving in rivers and streams, as well as excessive water in flood events, which usually occur in the spring melt-off season in May and June.

Snow is the main form of precipitation in the winter months, and the accumulation distribution of this snowpack is critical in determining the melt timing, amount of water, and potential for flood events and avalanches (Deems, et al., 2013). Snow can be measured in a variety of different ways. Snow course surveys measure snow depth and density are directly in the field, usually along transects (Pomeroy & Gray, 1995). Remote sensing methods and technologies, including lidar, satellite imagery, and microwave data can be used to determine snow cover and depth (Bhardwaj et al., 2016; Hopkinson, Sitar, et al., 2004). Additionally, installing in-situ equipment that measures the environment throughout the winter can be useful for determining snow density or depth in a specific location over time. (e.g. snow pillows, sonic ranging devices).

Snow mesurement methods are dependent on the environment, accessibility, terrain, and amount of snow (Pomeroy & Gray, 1995). For example, if the question about

the snowpack is related to spatial coverage, a remote sensing method may be more suitable, while in-situ field measurements may be more applicable for answering a question regarding snow density. Sometimes remote sensing is the only option if the site is difficult to access on foot (i.e. steep slopes or remote locations), while other times, a long history of field data is more valuable to analyze change in snowpack from year to year. Some methods, such as field snow density, also require a deeper snowpack to successfully collect a data point (Pomeroy & Gray, 1995; Pomeroy et al., 2002a).

1.3. Wildfire and Post-Fire Recovery

Anthropogenic climate change has been increasing the frequency and severity of wildfires (Cunningham et al., 2024; Giovando & Niemann, 2022; Maxwell & Clair, 2019; McGrath et al., 2023; Niemeyer et al., 2019), which reduces snowpack accumulation and causes the snowpack to melt out earlier (Gersh et al., 2022; Smoot & Gleason, 2021; Springer et al., 2015). Additionally, vegetation management and fire suppression activities have reduced the occurrence of natural fires in the past century in North America (Eisenberg et al., 2019; Parks et al., 2025), resulting in forests of older trees with greater volumes of biomass, and often reduced biodiversity (Lentile et al., 2006). Furthermore, increasing average temperatures in North America have increased the frequency of wildfires because some regions are warmer and drier than they have been in the past century. Therefore, when these fire suppressed areas burn, there is a lot more fuel, increasing the intensity of the fire (Aspinall, 2023; Chappell & Agee, 1996; Chasmer et al., 2017; Fiera Biological Consulting Ltd, 2014; Gerrand et al., 2021).

Wildfires are naturally occurring events which periodically remove dead vegetation from the landscape and allow for new vegetation to grow. Fires also support new biomass growth, and add nutrients to the soil through ash layers (Lentile et al.,

2006). Low intensity fires prevent the excessive accumulation of fire fuels and therefore prevent high intensity fires, which are often more severe (Cunningham et al., 2024). Wildfires can remove the organic material in the topsoil, the groundcover, understory, and the canopy (Aspinall, 2023; Flannigan et al., 2005; Gerrand et al., 2021).

The first species to return following a severe fire include herbaceous vegetation (i.e. grasses and annual flowering plants), with conifer species growing in later (Aspinall, 2023; Grandpre et al., 1993). Some early post-fire recovery species include fireweed (*Epilobium angustifolium)* and willow species (*Salicaceae spp;(*Kuijt*,* 1982*)*). Some conifer species, such as the lodgepole pine (*Pinus contorta),* require the heat of a wildfire to open the serotinous cones to release the seeds for germination, so this species begins to recover its population within a few years of the fire (Logan & Powell, 2001). Additionally, as woody shrubs and perennial plants recover, they provide shade for the shade-tolerant plants to regenerate.

Mountain snowpack is influenced by the removal of vegetation during wildfire. Decreased albedo due to ash and soot and increased solar radiation input on the snow surface due to reduced canopy cover, influence snow accumulation and ablation rates (Burles & Boon, 2011). When coniferous trees are removed from the landscape, the snow interception is reduced due to reduced leaf surface area, which decreases sublimation, and therefore increases the accumulation of snow on the ground. While snow tends to be deeper in open areas than in canopy covered areas (Pomeroy & Gray, 1995), the reduced vegetation increases the amount of wind redistribution of the snowpack, and it allows for more shortwave solar radiation to directly melt the snow (Broxton et al., 2021; Pomeroy, Gray, et al., 1998; Smoot & Gleason, 2021). These together tend to increase ablation and cause snow to melt more rapidly and earlier in the year, resulting in increased flood risk

in the spring due to rapid melt, and drought risk in the summer due to a longer snow-free season (Bladon et al., 2014).

1.4. Environmental Drivers of Post-Wildfire Regeneration

Several factors influence the regeneration of vegetation in post-fire mountain environments. Environmental drivers such as latitude, elevation, aspect, slope, topographic position index (TPI), solar radiation, water availability, soil availability, temperature, soil moisture, and terrain curvature (TC) all are important in local vegetation regrowth (Aspinall, 2023; Cartwright et al., 2020; Day et al., 1989; McCaffrey, 2018; Silins et al., 2009). These factors influence the species of vegetation, the rates of regrowth, and the condition of the returning vegetation (Odum, 1969). Some of these terrain drivers can act as proxies for understanding the micro-climatological conditions in the local landscape. For example, increasing elevation is often associated with decreasing air temperature increasing precipitation rates due to decreasing vapour pressuring (Barnes et al., 2025; Black, 1991; Cartwright, 2018).

Additionally, while wildfire influences snow accumulation, the previously listed environmental drivers also local snowpack accumulation distribution in the mountains(Cartwright, 2018; Pomeroy et al., 2002b). Other sites in the Rockies have shown that elevation and aspect are significant factors in determining snow depth (Barnes & Hopkinson, 2022a). To what extent each of these drivers influence snowpack accumulation distribution in the case study site is unknown.

1.5. Airborne Laser Scanning and Environmental Modelling

Lidar (light detection and ranging) is a useful remote sensing tool for collecting three-dimensional (3D) high spatial resolution data over relatively large areas in a short amount of time. Lidar is an active remote sensing technology that uses a sensor which

emits laser pulses of electromagnetic radiation at specific wavelengths, and records the time for the pulse to reflect off the target and return to the sensor (Baltsavias, 1999; Wehr & Lohr, 1999) . The sensor records the return time at the point at which a voltage of a certain threshold is recorded from the return pulse (Baltsavias, 1999) . The travel time, the speed of light, and the known position of the sensor from global navigation satellite system (GNSS) gives the range of the target, or the distance that the target is from the sensor (Hopkinson, Sitar, et al., 2004). When a lidar system is mounted on an airplane or remotely piloted aircraft system (RPAS), the range represents the height of the target. These ranges are converted into points in a 3D space, called a point cloud (Figure 1.2). The position of the aircraft in space is crucial to processing the data, so lidar data collection requires a sophisticated GNSS, inertial measurement unit (IMU), and ground control points (Baltsavias, 1999; Hopkinson, Sitar, et al., 2004).

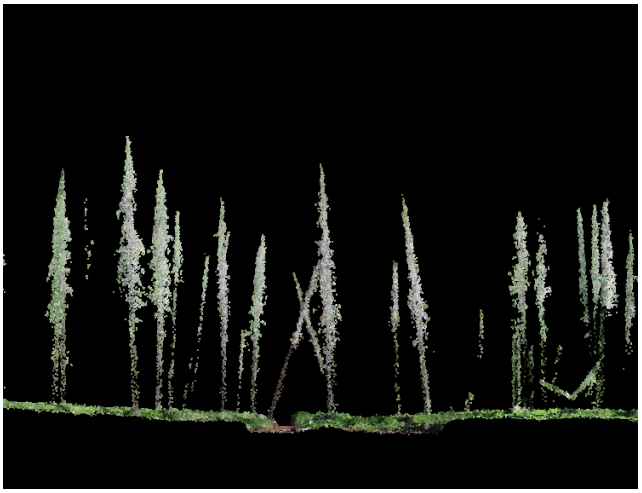

Figure 1.2: A photo of an example cross-section of a colourized RPAS lidar point cloud from Waterton Lakes National Park

One pulse that is emitted from the lidar system can give multiple return pulses, allowing for vertical measurements. Multiple returns are the result of one emitted lidar pulse returning many readings at different elevations at the same coordinate position

(Hopkinson et al., 2006; Hopkinson, Sitar, et al., 2004). These pulses occur in extremely rapid succession to develop complex and highly detailed 3D point clouds. Using multiple returns, the canopy, understory, and the ground surface for one horizontal position can be recorded (Figure 1.3). These returns can be classified for further processing in either a 2D or 3D format at a high spatial resolution (Hopkinson, Sitar, et al., 2004). Lidar point accuracy is highly dependent on the flight parameters, vegetation density, and terrain type (Hopkinson et al., 2008). As lidar technology has developed, the accuracy, pulse frequency, and the number of wavelengths increased, and the types of analysis became more sophisticated (Baltsavias, 1999; Hopkinson et al., 2016; Hopkinson et al., 2006).

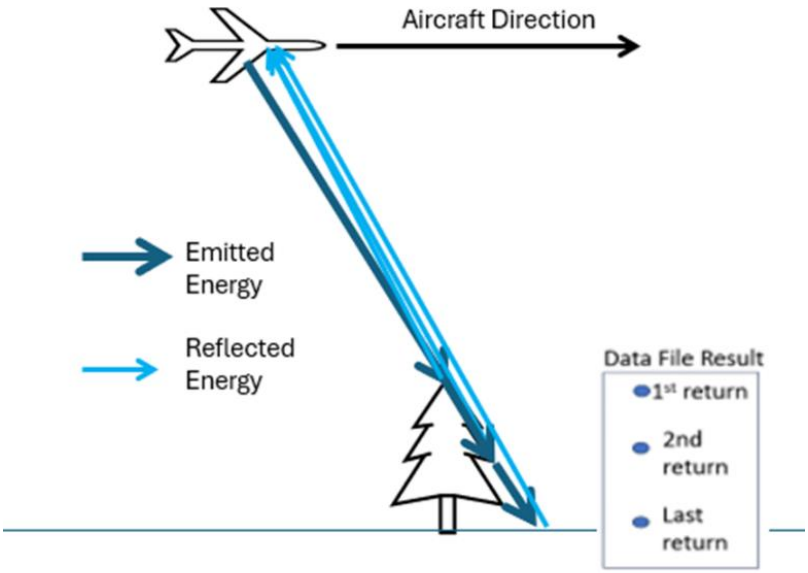

Figure 1.3: A basic schematic of airborne lidar, showing multiple returns from a scanner, and the point cloud that would result from a single pulse, showing first, intermediate, and last returns.

Multi-spectral lidar is a technology that involves scanning the area using more than one wavelength of laser pulses. For example, the “Titan” sensor (Teledyne Optech, n.d., Canada), has three different wavelengths, mounted at different angles, to measure the environment using multiple energy bands (Chasmer et al., 2017; Hopkinson et al.,

2016). Multi-spectral lidar allows for increased analysis options because multi-spectral indices can be created to determine different properties about the target. The active normalized burn ratio (aNBR) is an index for measuring wildfire severity, created by ratioing the shortwave infrared (SWIR) wavelengths (1550nm) with the near infrared (NIR) wavelengths (1064 nm) (Chasmer et al., 2017). Having three wavelengths can also increase the point density of the lidar, which provides further detail about the landscape that was not previously available.

Lidar can be used in combination with other remote sensing technologies, including air photos and satellite imagery. These passive remote sensing methods utilize solar energy to record a reflective response from the target, usually resulting in red-green-blue (RGB) or multispectral imagery (Lüdeke et al., 1996; Woebbecke et al., 1995). One way of interpreting remote sensing images is to create indices which compare wavelengths of different energy levels. Vegetation indices are often used for change detection analysis. For example, the greenness of vegetation can be measured using the normalized difference vegetation index (NDVI), which compares the red reflectance and near infrared reflectance in an image to determine the chlorophyll response, which is a proxy for vegetation health (Glenn et al., 2008; Nijland et al., 2014; Okhrimenko & Hopkinson, 2019; Reid et al., 2016). Another similar index is the green chromatic coordinate (GCC), which compares the green reflectance to the sum of the red, green, and blue reflectance of an image to determine the greenness of vegetation (Aspinall, 2023; Reid et al., 2016; Woebbecke et al., 1995). Passive optical and lidar data can be compared to validate results and observed environmental patterns at multiple scales.

Lidar provides an advantage to airborne photography and satellite imagery in this case in the mountains, due to the logistical constraints surrounding passive imagery

systems in this environment. Lidar is advantageous because it is an active remote sensing technology, and therefore it provides its own illumination source, and is not reliant on sky conditions (Baltsavias, 1999; Hopkinson et al., 2006). Airborne photography is highly influenced by sky and atmospheric conditions, including cloud cover, time of day, time of year, and other sources of shadowing that influence the reflectance energy response. Therefore, rather than using the NDVI derived from aerial photography, the aNBR from multi-spectral lidar can be used to determine vegetation change over time, due to the consistency in the lighting conditions provided by the active remote sensing technology.

Snowpack lidar surveys began in the early 2000s because snowpack monitoring became more important for measuring avalanche and flood risk (Yousefi et al., 2020), snow water equivalent (Hopkinson et al., 2024), and snow accumulation (Hopkinson, Sitar, et al., 2004). Lidar is a useful way of measuring snowpack because of the multiple return capabilities for detecting both the snow surface and obstacles including buildings and vegetation, and because it allows for measurements of otherwise inaccessible areas (Deems et al., 2013). For example, lidar has been used to study several features of snowpack dynamics in the American and Canadian Rockies, including snow water equivalent (SWE), accumulation, and effects of canopy and disturbances on snowpack (Bhardwaj et al., 2016; Deems et al., 2005; Kirchner et al., 2014; Tinkham et al., 2014). Snow lidar surveys provide spatially continuous data of snow depth, which is highly advantageous for mapping snow and water resources. Snowpack is highly variable and lidar surveys provide a snapshot in time of the snow depth, which is an important parameter in water resource calculations, especially if the survey is conducted at maximum snowpack accumulation. Snow depth of a region is determined by subtracting a "snow-off" ground surface from a "snow-on" ground surface (Barnes & Hopkinson,

2022a; Hopkinson, Sitar, et al., 2004). Snow lidar is highly susceptible to multipath errors due to the reflectivity of the snow, and there are additional errors inherent in mountainous areas and regions with steep terrain and vegetation, resulting in overestimations of snowpack (Deems et al., 2013). Despite the potential for errors in snowpack lidar models, they have been effective for furthering understanding of water resources in mountain headwaters (Barnes, 2023; Cartwright et al., 2020).

1.6. Study Area: Waterton Lakes National Park

Waterton Lakes National Park (WLNP) is a valuable area for multiple reasons, including international relationships, ecosystem habitat, cultural history, and water resources for Southern Alberta (Figure 1.4). WLNP was originally established in 1895 as Canada's fourth national park to create an area to protect the physical environment and wildlife (Parks Canada, 2023b). In 1932, WLNP was joined with Glacier National Park in the United States to create the Waterton-Glacier International Peace Park (Pringle, 1986). This park presents a unique ecotonal region between the prairie grasslands to the parkland forests, which then shifts into montane forests, up to alpine vegetation and bare rock. The park supports at least 60 species of mammals, 250 birds, 10 reptiles, and 24 fish, and over 1000 vascular plant species, with several endemic species (Parks Canada, 2023c).

Waterton Lakes National Park is also important hydrologically to the Oldman River Basin (ORB), which supports many cities and towns in Southern Alberta. The park contains many streams, lakes, and creeks which eventually flow into the ORB. The basin has a mean annual flow of over two million decameters (Swenson, 2002). The watershed supports over 210,000 people directly in the ORB area, as well as people outside of the basin because the ORB is a smaller region of the larger South Saskatchewan Watershed (Oldman Watershed Council, 2023). WLNP has at least fifteen tributary lakes and

streams to the ORB. These streams and lakes are fed by seasonal snowpack, especially the higher elevation regions, that used to be glacial lakes before all of the glaciers melted in the park. Two other local watersheds were also included in the study as comparison regions to WLNP, these are Lynx Creek (LC) and West Castle Watershed (WCW). These areas also flow into the ORB and different ecosystems dynamics have been studied in these regions (Barnes, 2023; Cartwright, 2018; McCaffrey, 2018)

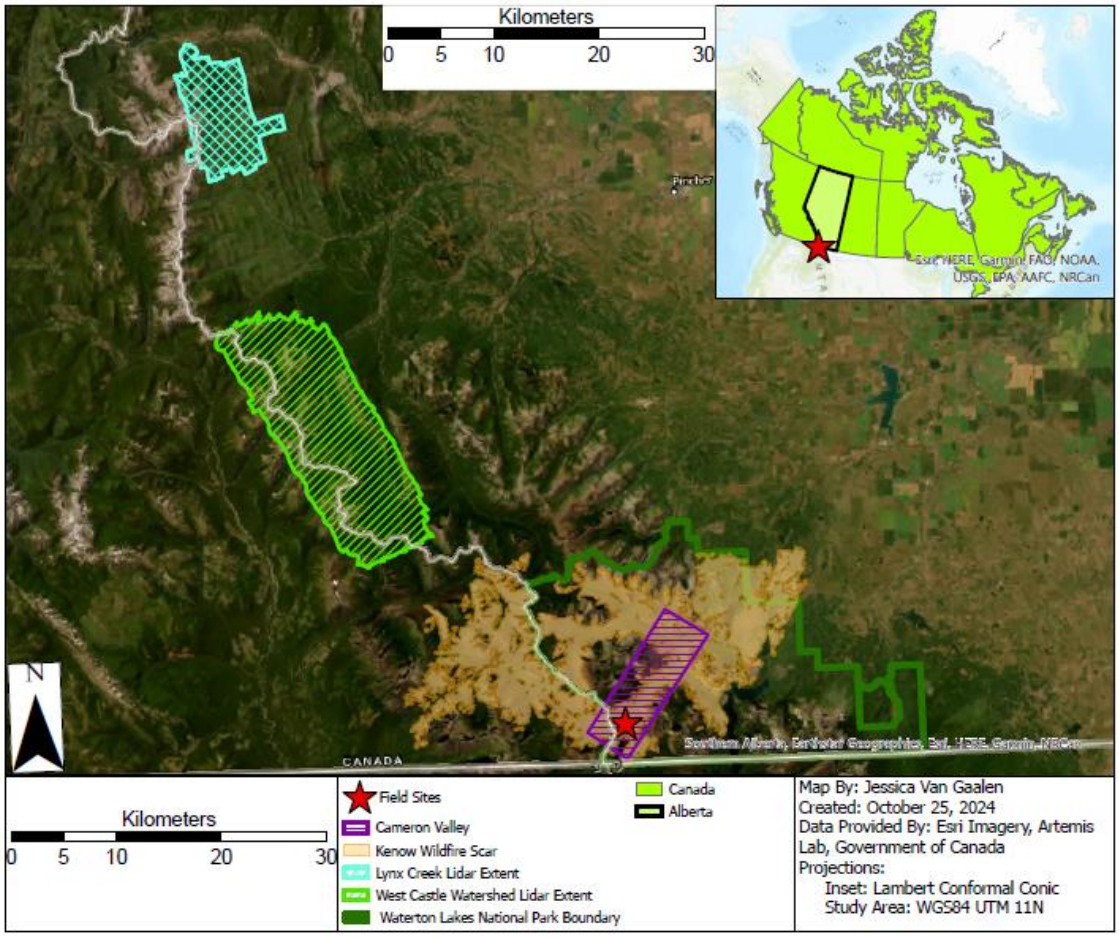

Figure 1.4: A map of the study areas for this research, showing the locations of WLNP, CV, the field data collection area, and the comparison sites of Lynx Creek and West Castle Watershed.

The Kenow Wildland Fire (KWF) burned 38% percent of WLNP (19 303 hectares), as well as regions in British Columbia (BC) and Alberta that extended beyond the park boundary (Parks Canada, 2023a). Prior to the 2017, fire suppression and land

management techniques had been applied for over a century, with the most recent fire occurring in 1919 (MacDonald, 2000), These practices increased the fuel load, resulting in hotter and more severe fires (Eisenberg et al., 2019; Parks et al., 2025). The KWF was started by a lightning strike on Kenow Mountain in BC on August 30th, 2017 (Figure 1.5), and it quickly spread eastward due to high-speed wind and hot, dry weather that had occurred all summer (Parks Canada, 2023a). The fire took over a month to get under control, and the townsite and surrounding areas were evacuated. This fire removed much of the vegetation in CV, including the treeline in many areas. However, a few locations were left untouched by the fire in Lineham and Rowe valleys, and these areas will be old growth forest comparison regions.

Figure 1.5:A photo of the Kenow Wildland Fire in the Cameron Valley, facing northeast from Cameron Lake (Parks Canada, 2023a).

CV was selected for research because it represents a wide range of elevations, aspects, slopes, burned and unburned areas, moisture levels, temperatures, vegetation diversity, and it is relatively accessible (Figure 1.4). This area receives snowpack from October to May (Barnes et al., 2025), and the plants grow quickly between June and

September. Additionally, airborne lidar data has been collected for this area at least once per summer and at least once in most winters since 2018, creating a chronosequence for observing growth and change in the early-stage post-fire environment. This region also is part of the ORB headwaters, and because of the fire, it is possible that headwater snowpack has changed, which would influence the water supply to this basin, and therefore would impact the people and ecosystems downstream.

1.7. Research Objectives and Overview of the Thesis

The goal of this research is to model spatial changes to vegetation and snowpack distribution relative to terrain drivers in Waterton Lakes National Park (WLNP) since the Kenow Wildfire Fire in 2017, to better understand ecosystem dynamics in this post-fire environment. While it is expected that the hypsometric snowpack distribution will differ between burned and unburned areas, this difference has not been explicitly quantified for Cameron Valley. It is not known how the vegetation will regenerate across Cameron Valley following this fire, or whether there will be a consistent pattern to its distribution. Correlations between snow distribution and regenerating vegetation have not previously been established in the post-fire Cameron Valley environment. Several environmental drivers influence snowpack and vegetation in burned environments in other regions and on smaller scales (Aspinall, 2023; Burles & Boon, 2011; Cartwright, 2018; Davis, 2012). Therefore, it is important to determine if these drivers apply in this region by developing a new model, as snow models are highly subject to spatial variability, and decrease in accuracy if extrapolated on (Grunewald et al., 2013). The post-fire valley-to-alpine region of Waterton Lakes National Park requires observation and analysis to relate snow and vegetation for predicting early-stage post-fire recovery in similar regions that could burn in the future.

The objective of this thesis was to determine the rates of change and spatial patterns in post-fire vegetation regeneration and snowpack distribution in WLNP relative to the local mountainous terrain using lidar. This objective was met by using lidar to A) develop a new monitoring framework for post-fire vegetation regeneration, B) quantify the changes in vegetation height, greenness, and cover relative to the terrain, and C) to quantify the changes in snowpack accumulation depth and distribution in Cameron Valley since the fire relative to vegetation regeneration and terrain. The list below includes the main questions and associated hypotheses that focused the research:

A) Can a combination of field, RPAS, and airborne lidar data be used to develop an effective multi-scalar post-fire vegetation monitoring framework based on the height and cover measurements of the vegetation?

   H_0: The combination of data does not allow for effective modeling of post-fire vegetation regeneration across the area.

   H_a: The combination of data allows for effective modeling of post-fire vegetation regeneration across the area.

B) Is the distribution of vegetation regeneration across Cameron Valley significantly related to one or more terrain driver(s)?

   H_0: Vegetation regeneration is not significantly related to any terrain drivers.

   H_a: Vegetation regeneration is significantly related to one or more terrain driver(s).

C) Is snowpack distribution in the post-fire environment of Cameron Valley significantly related to vegetation cover or any of the terrain drivers in the early vegetation regeneration stages?

   H_0= Snowpack distribution patterns are not significantly related to vegetation cover or terrain drivers.

H_a= Snowpack distribution patterns are significantly related to vegetation cover and/or terrain drivers.

This thesis is organized with chapter 1 as the introductory chapter, including a literature review and a description of how this research is relevant and significant in a wider context. Chapter 2 is the first paper from this thesis, discussing vegetation monitoring frameworks at multiple scales using various data. Chapter 3 discusses vegetation regeneration in WLNP and the stratification of vegetation growth with terrain drivers using the multi-scalar models developed in Chapter 2. Chapter 4 discusses snowpack distribution and depth differences between burned and unburned areas over time, relative to terrain and vegetation drivers. Chapter 5 concludes the thesis with a discussion of all the previous chapters and suggestions for future research. Appendix A includes further field data results not presented in Chapter 2, Appendix B discusses adjustments to the lidar data due to atmospheric attenuation, and Appendix C demonstrates alternate methods that lead to an independent validation of the results presented in Chapter 2.

2. Chapter 2: Monitoring Post-Fire Vegetation Height and Cover in a Mountain Park using Field, Remotely Piloted Aircraft System, and Multi-spectral Airborne Lidar Data

2.1. Abstract

Wildfires significantly alter mountain forest environments, and monitoring the post-fire recovery patterns and rates is critical in informing land management decisions. Monitoring frameworks of post-fire vegetation regeneration often are either missing the detail of the field scale or the breadth of the remote sensing scale. A multi-scalar vegetation monitoring framework was developed in the burn scar in Waterton Lakes National Park, Canada, using a combination of in-situ, remotely piloted aircraft system (RPAS), and multi-spectral airborne lidar survey data. The objectives were to use multiple types of data to predict vegetation cover and height from field to airborne scales surveys to accurately model vegetation regeneration over time. Vegetation height and 'greenness' as a proxy for fractional cover were measured at each scale during peak phenology each year to determine rates of vegetation recovery. Height models were not effective for transfer across scales in the study period due to high variance in height due to debris, but height models are expected to become effective as the seedling heights increase. Greenness is an effective proxy for fractional cover across scales from field to RPAS to airborne (r^2>0.89). Using a combination of scales and spectral indices was effective for developing a transfer function for predicting fractional cover in the burned region in the first seven years of post-fire regeneration. Cover reached saturation within 5 years in the riparian site, and 7 years in the upland site. Therefore, the recommended monitoring framework for early-post fire regeneration is to use a multi-scalar approach that focuses on cover measurements within the early years, then shift to height models as the cover models saturate.

2.2. Introduction

Wildfires have been occurring more frequently and often with higher severity in the Canadian Rocky Mountains in the past couple of decades (Aspinall, 2023; Baron et al., 2022; Jain et al., 2024). The severity of wildfires is connected to the amount of biomass removed and the degree to which the environment has been altered (Baron et al., 2022; Cunningham et al., 2024). Higher intensity fires can occur as a result of increased average temperatures in the area, drier weather, and fire suppression activities in the past century which have prevented smaller, lower intensity wildfires (Eisenberg et al., 2019; Parks et al., 2025). A combination of these factors resulted in excessive fire fuel loading in the region, causing hotter and larger wildfires than have been observed in the past century (Parks et al., 2025). These intense wildfires can remove high proportions of the vegetation and organic soils from an environment (Gerrand et al., 2021).

Vegetation is critical for regulating the local hydrological cycle through processes such as evapotranspiration and groundwater infiltration (Black, 1991), for slowing geomorphological processes such as mass movement and erosion (Bladon et al., 2014; Silins et al., 2009), and for supporting ecological processes including habitat formation and species diversity (Kuijt, 1982). Post-fire vegetation recovery also influences the environment regarding ecological succession and hydrology (Robinne et al., 2020; Schoennagel et al., 2003). Additionally, local vegetation species diversity has been known to change following mountain forest fires, which can change the ecosystem communities and dynamics in the region (Schoennagel et al., 2003; Turner et al., 1997). Therefore, quantifying and modelling post-fire vegetation in severely burned regions is critical for understanding changes in the environment.

Lidar (light detection and ranging) is a useful remote sensing technology for many forestry applications, including detecting and quantifying fire fuels (Bright et al., 2022; Cameron et al., 2021), and quantifying vegetation metrics including height and cover (Lim et al., 2003; McCaffrey, 2018). Airborne lidar utilizes laser technology to determine the position of targets relative to the position of the aircraft carrying the laser senser based on measuring the timing between laser pulse emission and reception, and has the benefit of multiple returns, resulting in a three-dimensional (3D) scan of the surface (Baltsavias, 1999). These lidar measurements are interpreted as height measurements,, and these points allow for the development of models of elevation, terrain, and vegetation height (Baltsavias, 1999; Chasmer et al., 2017; Hopkinson et al., 2016; Wehr & Lohr, 1999). The Titan multi-spectral lidar system (Teledyne Optech, 2023) uses three different laser wavelengths to scan the surface, allowing for increased point density and therefore increased spatial resolution compared to some systems, and multiple wavelengths allow for different optical measures of the same features on the Earth's surface. Another benefit of multi-spectral lidar is the ability to develop normalized spectral indices such as the active normalized burn ratio (aNBR), which can be used to determine brightness of vegetation and the severity of fire (Hopkinson et al., 2016).

Lidar data can be collected using multiple platforms, including aircraft and remotely piloted aircraft systems (RPAS), and is validated using field data. Therefore, each scale and type of data, (field, RPAS, and airborne) should provide similar information, and this is true in mature forests (Hopkinson et al., 2016). However, in early post-fire regenerating mountain environments, a method of model transfer between scales using field, RPAS, and multi-spectral airborne lidar data has not been attempted. It is

critical to model vegetation regeneration at different spatial scales to further understand the complexities and influences that this early vegetation may have on water resources and ecology. Using a combination of height and cover measurements is expected to be useful, as at all scales, height can be determined from structural information collected in the field and from the lidar data, and cover can be determined from a spectral index until the index saturates. Determining the utility of both measurements of vegetation regeneration is expected to improve the long-term capability of modeling the growth across the region.

This research combines multispectral airborne lidar, RPAS lidar, RPAS passive optical, in-situ vegetation height measurements, and in-situ vegetation RGB photography, to develop a multi-scalar post-fire monitoring framework that captures the detail and extent of information needed to determine rates of vegetation recovery. Therefore, the main objectives are to a) develop a multi-scalar vegetation monitoring framework for post-fire environments, using metrics of height and cover, b) to model vegetation regeneration over time to predict the point in time at which cover measurements reach saturation and when height becomes the more reliable measure of vegetation growth. Further understanding of post-fire recovery of vegetation can help with predicting future recovery in headwater regions and can increase our understanding of the effects of wildfire on vegetation and therefore water resources.

2.3. Methods

2.3.1. Study Area

Waterton Lakes National Park (WLNP, 113° 54' 46.38" W, 49° 2' 54.98" N), is in the southwestern corner of Alberta, Canada, and borders British Columbia and Montana, USA (Figure 2.1). The park was burned in an intense fire in 2017, affecting 38% (19,3030

ha) of the area (Parks Canada, 2023b). This national park is an important headwater source for the downstream Oldman River Basin (ORB) which directly supports over 210,000 people as well as irrigation and industry (Oldman Watershed Council, 2023). The park is also supports multiple important ecosystems for many endemic plant species and supports a wide variety of flora and fauna, due to the wide range of ecozones from prairie grasslands to alpine environments(Government of Alberta, 2005).

WLNP was compared to two other local watersheds which have each burned at different times previously. The Lynx Creek (LC) watershed burned in 2003 and shows a post-fire regrowth trajectory for up to 22 years. West Castle Watershed (WCW) last burned in 1936 and is an old-growth forest. These regions represent two stages of post-fire regeneration, with a timeline of forest and ecosystem recovery of 19-22 years, and a timeline of 83-89 years, respectively. There are also comparison areas within Cameron Valley that did not burn due to water bombing and the fire patterns in the region, which show what the forest was like prior to the burn (Figure 2.1).

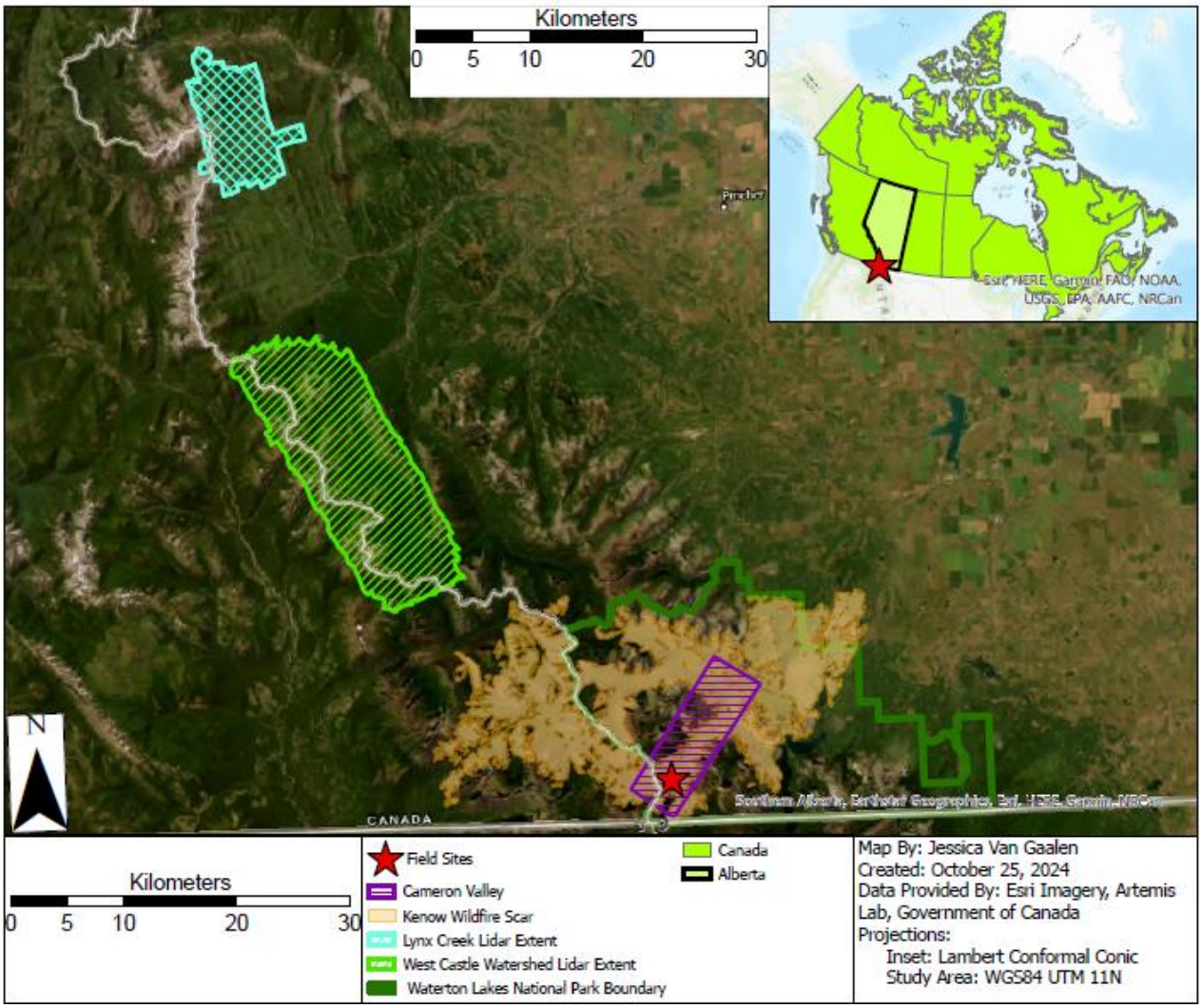

Figure 2.1 A map of the study area, showing the field sites and airborne lidar survey polygons in the southern Alberta Rockies.

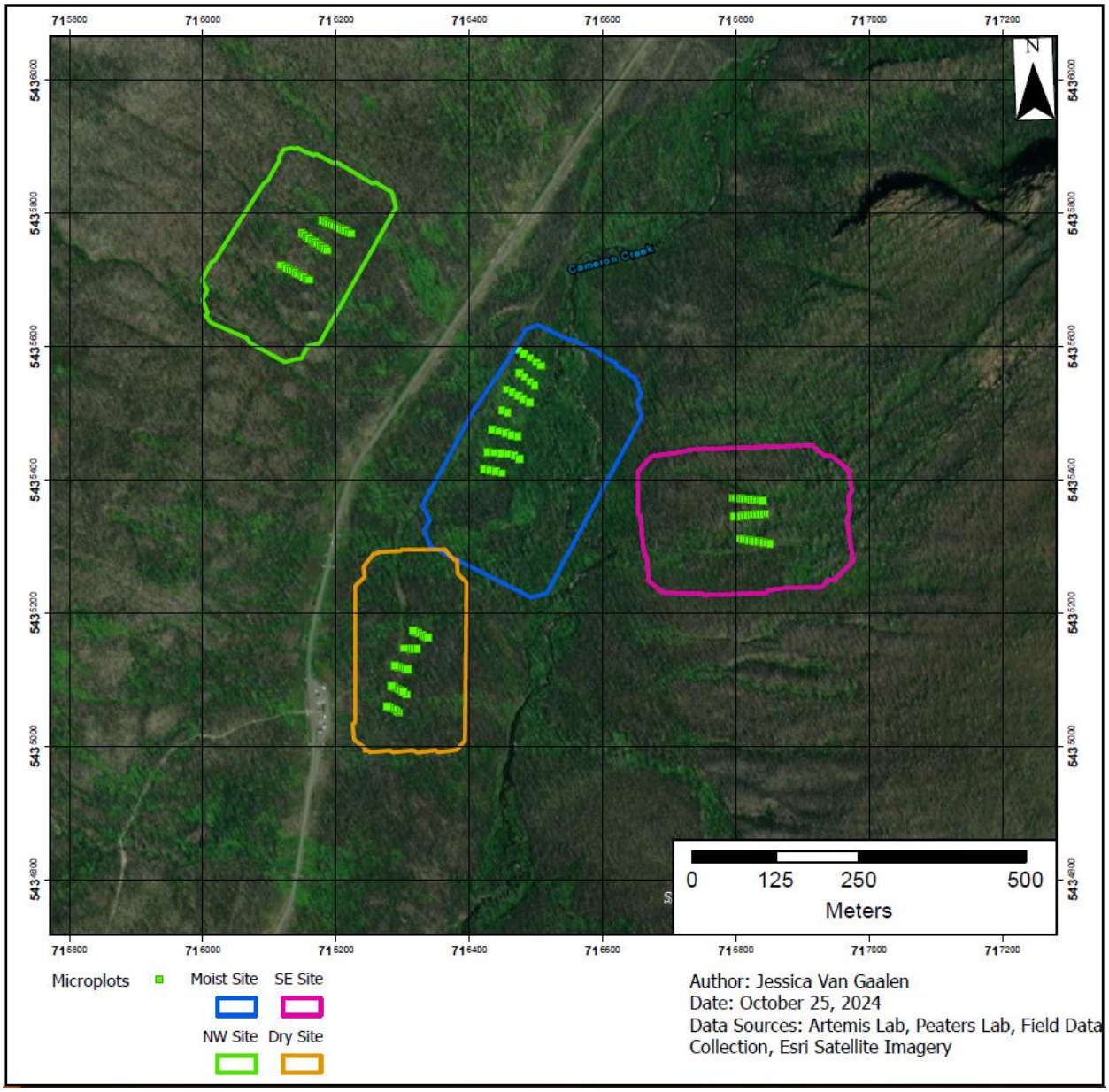

Figure 2.2: RPAS lidar polygons and field microplot sites in the south end of Cameron Valley, in Waterton Lakes National Park.

2.3.2. Data Collection

2.3.2.1 Field Measurements.

Field measurements were collected in Cameron Valley in four survey areas, the moist site, dry site, northwest site, and southeast site (Figure 2.2; Table 2.1). Height data were collected by measuring within approximately 1m² plots, on the west, center, and east sides of the plot, and taking the mean height (Aspinall et al., 2025). The maximum height

was also measured. For each plot, a RGB photo was taken using either a digital camera or cell phone camera, facing nadir, with north at the top (Figure 2.3). The precise locations of these plots were collected using either a Topcon GNSS (valley bottom sites) or a Hemisphere GNSS receiver system (hillslope sites) and precise point positioning techniques. A total of 445 plots were measured over 7 years, as presented in Table 2.1. and in Appendix A.

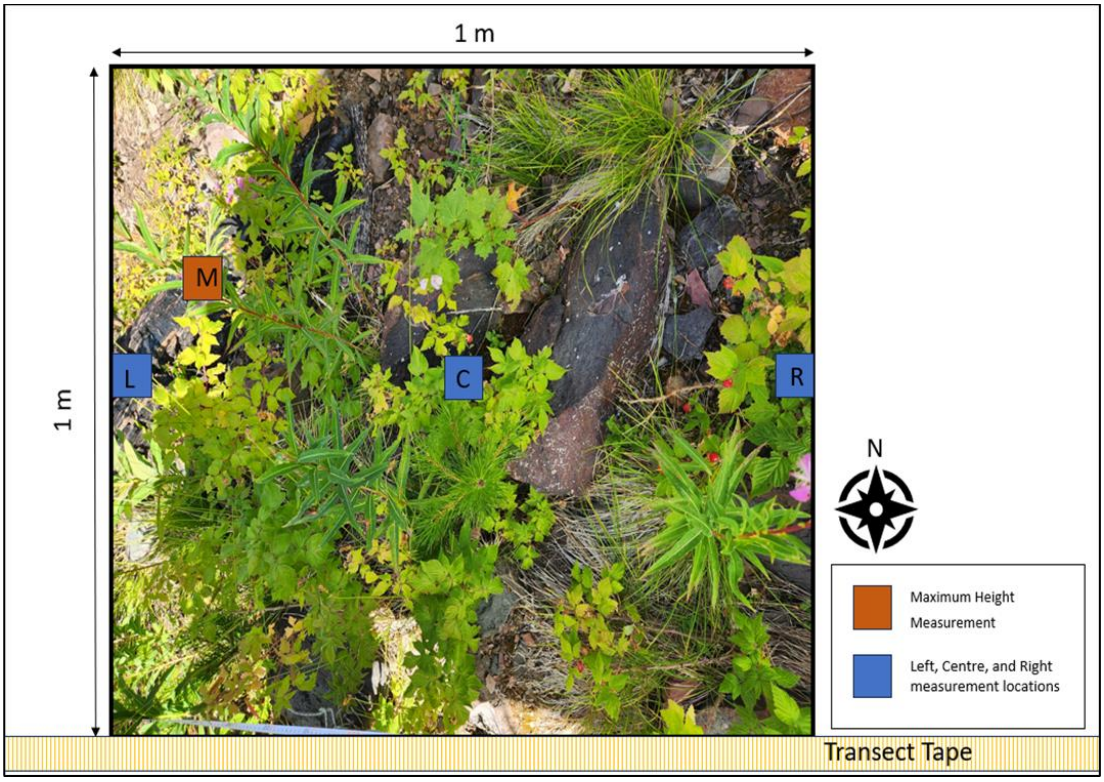

Figure 2.3: An example in-situ field microplot, showing height measurement locations and the overhead nadir photo, taken at 1.3m in height above ground level using a standard digital or cell phone camera

Table 2.1: The location, date, and number of field plots collected in July in each area: where MS =Moist Site, DS =Dry Site, SES =Southeast Site, and NWS= Northwest Site

Site ID	Date (DD-MMM-YY)	Number of Plots
MS	18-Jul-19	31
MS	19-Jul-20	31
DS	19-Jul-20	29
MS	08-Jul-21	16
DS	08-Jul-21	16
MS	21-Jul-22	31
DS	21-Jul-22	29
MS	19-Jul-23	29
DS	19-Jul-23	29
SES	24-Jul-23	39
NWS	26-Jul-23	39
MS	16-Jul-24	31
DS	16-Jul-24	29
SES	12-Jul-24	33
NWS	08-Jul-24	33

2.3.2.2 RPAS Surveys

RPAS surveys were conducted over the four sites: moist site (MS), dry site (DS), southeast site (SES), and the northwest site (NWS), (Figure 2.2). Table 2.2 describes the surveys and instruments used. Optical RGB imagery and structure from motion (SfM) data were collected each year, while lidar was only collected for 2022-2024. The surveys were conducted coincident with the airborne lidar data collection and the field surveys. Each RPAS survey polygon covered approximately 2.5 ha.

Table 2.2: The location, date, aircraft, sensor, and data types from each of the RPAS surveys in the CV.

Site ID	Flight Date (DD-MMM-YY)	Aircraft	Sensor	Data Output
MS	16-Jul-18	Mavic Pro 1	FC220_4.7_4000x3000 (RGB)	Orthos, SfM
DS	16-Jul-18	Mavic Pro 1	FC220_4.7_4000x3000 (RGB)	Orthos, SfM
SES	16-Jul-18	Mavic Pro 1	FC220_4.7_4000x3000 (RGB)	Orthos, SfM
NWS	16-Jul-18	Mavic Pro 1	FC220_4.7_4000x3000 (RGB)	Orthos, SfM
SES	07-Jul-19	Mavic Pro 2	L1D-20c_10.3_5472x3648 (RGB)	Orthos, SfM
NWS	07-Jul-19	Mavic Pro 2	L1D-20c_10.3_5472x3648 (RGB)	Orthos, SfM
MS	29-Jul-21	Mavic Pro 2	L1D-20c_10.3_5472x3648 (RGB)	Orthos, SfM
DS	29-Jul-21	Mavic Pro 2	L1D-20c_10.3_5472x3648 (RGB)	Orthos, SfM
NWS	29-Jul-21	Mavic Pro 2	L1D-20c_10.3_5472x3648 (RGB)	Orthos, SfM
SES	29-Jul-21	Mavic Pro 2	L1D-20c_10.3_5472x3648 (RGB)	Orthos, SfM
MS	08-Jul-22	Matrice	DJI Zenmuse L1	Lidar, Orthos, SfM
DS	08-Jul-22	Matrice	DJI Zenmuse L1	Lidar, Orthos, SfM
MS	19-Jul-23	Matrice	DJI Zenmuse L1	Lidar, Orthos, SfM
DS	19-Jul-23	Matrice	DJI Zenmuse L1	Lidar, Orthos, SfM
NWS	19-Jul-23	Matrice	DJI Zenmuse L1	Lidar, Orthos, SfM
SES	19-Jul-23	Matrice	DJI Zenmuse L1	Lidar, Orthos, SfM
MS	16-Jul-24	Matrice	DJI Zenmuse L1	Lidar, Orthos, SfM
DS	16-Jul-24	Matrice	DJI Zenmuse L1	Lidar, Orthos, SfM
SES	16-Jul-24	Matrice	DJI Zenmuse L1	Lidar, Orthos, SfM
NWS	16-Jul-24	Matrice	DJI Zenmuse L1	Lidar, Orthos, SfM

2.3.2.3 Airborne Lidar Surveys.

Airborne lidar data were collected during peak phenology each year (July) from 2018 to 2024 over the 6,507 ha WLNP lidar polygon (Figure 2.1; Table 2.3) within approximately a week of field and RPAS surveys. The surveys were scheduled to attempt to capture the maximum vegetation growth, both in height from the point cloud and in intensity in the multispectral channels, which include a green channel (532 nm), a near infrared (NIR) channel (1064 nm), and a short-wave infrared (SWIR) channel (1550 nm)

(Teledyne Optech, 2023). Additionally, lidar data were collected in Lynx Creek and West Castle Watershed in several years as comparison sites for WLNP (Table 2.3).

Table 2.3: An overview of the airborne lidar surveys: WCW =West Castle Watershed, WLNP= Waterton Lakes National Park, and LC= Lynx Creek.

Year	Date	Region
2018	July 16	WLNP
2019	July 22	WLNP
2019	July 23	LC
2020	July 29	WLNP, WCW
2021	July 15	WLNP, LC
2021	July 16	WCW
2022	July 20	WLNP, WCW
2023	July 19	WLNP
2024	July 5	WLNP, LC, WCW

2.3.3. Data Analysis

2.3.3.1. Pre-Processing and Quality Control

Pre-processing of the RGB imagery from both the field and RPAS data included light normalization procedures and involved either removing direct sunlit areas in the field photos, or shadows from the RPAS orthophotos. RPAS imagery was aligned in ArcGIS Pro (Esri, 2025), based the airborne lidar data. The imagery from the field plot cameras and the associated RPAS surveys sensors were compared directly by aligning the photos to the same spatial location to check for potential systematic biases in the spectral responses of the systems. Existing bias in the spectral response may influence the results of the greenness and cover products derived from the spectral response.

Airborne lidar, RPAS lidar and SfM data were aligned and classified using Terrascan (Soininen, 2023; Terrasolid Inc., 2024) and Quick Terrain Modeller (Applied Imagery, 2024). The 3D point clouds for each year were gridded using a triangulated irregular network (TIN) for developing 1m spatial resolution digital elevation models

(DEMs) representing the ground surface in LasTools (rapidLasso, 2024). Digital surface models (DSMs) were developed using a local maximum elevation value to 1m spatial resolution. Airborne lidar data channels were also processed individually and gridded to 1m in LasTools to develop intensity rasters for the SWIR and the NIR to calculate aNBR. These intensity rasters were later further aggregated to a 5m grid cell to increase spatial coverage. Quality control processes were applied to all datasets to remove anthropogenic effects and to remove artifacts in the data including below ground and air points. Additionally, the airborne lidar data were divided into burned and unburned area based on the burn scar polygon (Government of Alberta, 2023).

2.3.3.2. Height Calculations and Model Scale Transfers

For the in-situ data, the vegetation heights were directly measured in the field, and the mean and standard deviation of the height measurements were calculated for each plot for each year. For RPAS and airborne lidar datasets, vegetation height was calculated by taking the bare earth digital elevation model (DEM) and subtracting it from the digital surface model (DSM) to develop a canopy height model (CHM) with a 1m grid cell resolution (Equation 2.1 (St-Onge & Achaichia, 2001)). All grid cells that returned a negative result were set to zero. To remove cells that had height measurements indicative of tall dead standing vegetation in the burned area, the maximum height was set to 3m above ground level, based on the maximum height of live vegetation observed in the field. This attempt to remove dead standing stems improves the accuracy of the live canopy height model. This process also ensured the removal of overhanging cliffs and crags that were incorrectly classified as forest vegetation.

Equation 2.1: CHM =DSM-DEM

Height model transfer across scales was performed at the individual grid cell spatial scale. The mean height of each field plot was calculated and compared to the nearest neighbour CHM value from the RPAS surveys. The RPAS CHMs were aligned to the airborne lidar CHMs at a 1m spatial resolution for direct comparison.

2.3.3.3. Greenness Calculations from Spectral Information

Greenness values from field based RGB photography and the RPAS surveys were calculated using the green chromatic coordinate (GCC, Equation 2.2). This is an index of green reflectance compared to the total reflectance of the sum of red, green, and blue bands (Reid et al., 2016; Woebbecke et al., 1995; Wyszecki & Stiles, 1967). This index was selected over other vegetation indices because it effectively suppresses the lighting and species differences, and includes RGB wavelengths found in standard digital and cell phone cameras (Liu et al., 2022; Nijland et al., 2014; Reid et al., 2016). Each RGB band was extracted individually, and Equation 2.2 was applied to develop the per-pixel GCC for each image for both the field and RPAS scales. The field photo GCC was recorded as one mean value over each image, each of which cover an area of approximately 1m on the ground. RPAS GCC was calculated as a per pixel value at a spatial resolution of approximately 2 cm.

Equation 2.2: GCC = green/ (red + green + blue)

To calculate the greenness from the airborne lidar data, the active normalized burn ratio (aNBR) was determined from intensity values collected from the survey (Equation 2.3, (Chasmer et al., 2017)). The intensity bands calculated from the NIR and SWIR lasers are ratioed in aNBR, as the NIR light reflects strongly from vegetation, with little response on dark surfaces. SWIR light reflects strongly from darker surfaces, including

water and blackened, sooty surfaces. Therefore, lower aNBR responses indicate reduced vegetation and a more blackened area, and higher aNBR responses indicate increased vegetation and reduced soot. This index is similar to the differenced normalized burn ratio (dNBR), which is typically used as an indicator of burn severity using passive imagery (Chasmer et al., 2017). The advantage of aNBR over dNBR is that it uses its own illumination source and therefore is not impacted by shadowing from dead standing stems, clouds, and mountainous terrain. This index can also be used to estimate vegetation regeneration in early stage post-fire years, as the index becomes 'less negative' as the surface brightens following a fire, often due to vegetation growth (Aspinall et al., 2025).

Equation 2.3: aNBR = (SWIR-NIR)/(SWIR+NIR)

The aNBR values for the 2019 flights were originally about 10% higher across the region in both WLNP and LC than the 2018 and 2020 datasets, as determined by comparing 40 pseudo-invariant features including roadways, bare rock cliff areas, and highly dense vegetation areas, for each year. This indicated that the 2019 survey was falsely indicating significant growth in one year. Therefore, after testing several transformations, the 2019 datasets were adjusted down by a linear scale of 10%. This is likely due to attenuation in the SWIR channel response, caused by an increase in relative humidity during the survey by approximately 10% compared to the relative humidity during the surveys for all other years (Government of Alberta, 2025). Further discussion of this correction application is presented in Appendix B.

To compare the two indices, a linear regression was applied to the field and RPAS GCC, then to the RPAS GCC and airborne lidar aNBR. Since the RPAS orthophotos have

a high spatial resolution (average grid cells size <0.02 m), the GCC of each pixel was calculated, then the pixels were aggregated using the mean to a 1 m resolution. The field and RPAS GCC values were related using the GNSS positions of the field plots and finding the nearest neighbour 1 m RPAS GCC grid cell. Then, the RPAS GCC was aggregated to a 5 m grid cell from the 1 m dataset, using the mean GCC value, and these aggregated datasets were related to the 5 m and airborne lidar aNBR using a direct spatial join function between the surveys.

2.3.3.4. Fractional Cover Predictions for Each Scale and Model Scale Transfers

The fractional cover (Fcov) for each survey was determined based on the initial relationship developed at the field image scale relating GCC to Fcov using a binary threshold. A threshold was applied the GCC to develop a proxy for vegetation cover over each field photo, since Fcov tends to be a more accurate measure of vegetation cover than GCC (Liu et al., 2022). Several potential GCC threshold values determined through endmember sensitivity analysis were tested on 15 field images analysis to narrow down the accurate 'covered' or 'not covered' threshold for the GCC in each pixel of the field imagery, which had a sub-centimeter spatial resolution. This was done by manually assessing images, and a threshold value of 0.38 on a GCC scale of 0-1 was selected. Each binary value raster (Figure 2.4d) was compared to the original image (Figure 2.4a) to manually assess the correctness of the threshold. In the field photos, the Fcov of the image is represented as a percentage of the total area surveyed based on the green to non-green ratio (Figure 2.4).

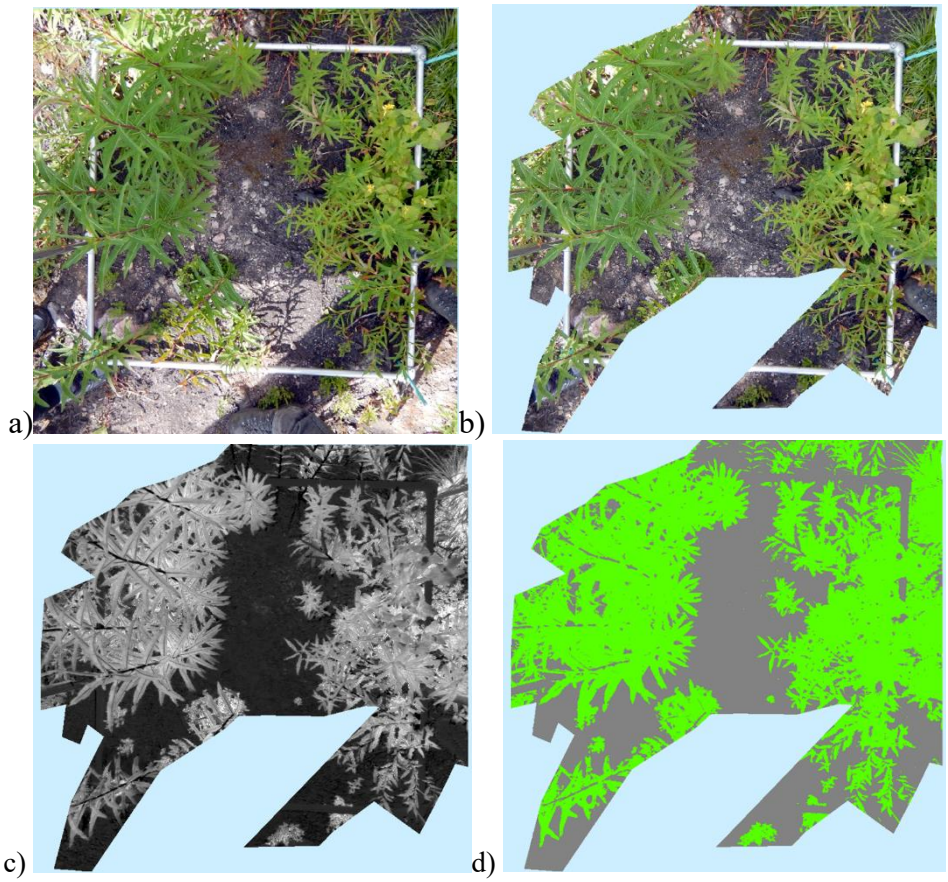

Figure 2.4: An example of the vegetation cover proxy calculation from GCC in the field, showing all steps from the original field photograph (a), the light normalized photo (b), the GCC (c), and the vegetation cover proxy derived from the binary threshold (d). The blue area indicates no data.

The Fcov values for the RPAS data were calculated by comparing the RPAS GCC from the ortho imagery to the Fcov values from the field photos over the same area. The RPAS GCC was related to the Field Fcov to predict RPAS Fcov at the 1m grid cell using the nearest neighbour distance to determine the closest related RPAS GCC pixel to the location of the field plots. Once the relationship was established between Field Fcov and RPAS GCC, the GCC value which predicts a value of zero Fcov was determined using the original linear regression equation to increase the accuracy of the model, as the original relationship predicted a vegetation presence in known regions of no vegetation growth, such as on large boulders and in rivers. This zero Fcov prediction was found to occur at an RPAS GCC threshold value of 0.325. Therefore, any values in the corrected

1m RPAS GCC less than the threshold were set to have an Fcov value of zero, and values greater than the threshold were used in the equation.

To improve the prediction of RPAS Fcov, RPAS GCC had to be corrected to include the zero Fcov prediction, using a threshold value. The original RPAS GCC values at the spatial resolution of 2cm grid cells were used for correction to preserve the pixel values, as at this scale, the effects of mixed pixels are reduced. This improved the results as spatial resolution reduced as the area of interest increased. A natural breaks threshold was applied to each survey to determine pixels which were 'vegetated' or non-vegetated.' To allow for zero predictions using this threshold, the GCC value for zero Fcov prediction (0.325) was subtracted from the entire RPAS GCC dataset. The binary 2 cm RPAS GCC raster was aggregated using the mean to a 1m raster to allow for comparison with the field plots. The original relationship equation between Fcov and RPAS GCC was applied to get a RPAS Fcov raster with a spatial resolution of 1 m which was used to predict Fcov for the full range of values.

Finally, to transfer the Fcov prediction to the airborne scale, the RPAS Fcov at 1 m was aggregated by mean to match the 5 m aNBR raster. Again, a threshold was required to determine the value at which Fcov would be predicted to be zero at a certain aNBR value, to consistently predict zero cover in areas which are known to have no vegetation based on ground observations, such as areas beyond treeline, and roads and cleared paths. This allows for the full range of Fcov values to be predicted. Once this threshold was established, the relationship between aNBR and RPAS Fcov was applied to the aNBR datasets to create airborne scale Fcov maps and descriptive statistics for each year of observation. Figure 2.12 is a summarization figure of the logic followed to achieve the

final equation series for the Fcov model transfer from the field to the airborne lidar scale. Independent methods and validations of the results of this transfer function are described in Appendix C.

2.3.3.5. Final Monitoring Framework Development

The monitoring framework developed for estimating vegetation regeneration at multiple scales includes both data collection and data analysis sections. Data collection includes field observations, RPAS surveys, and airborne lidar surveys, described in Section 2.3.2. Data analysis includes developing vegetation height datasets and cover datasets for comparison across measurement scales and types, as described in the previous sections. Detailed scale transfer information is presented in Figure 2.5. The overall monitoring framework developed and then applied to the datasets in Cameron Valley is presented in the results in Section 2.4.1 in Table 2.4.

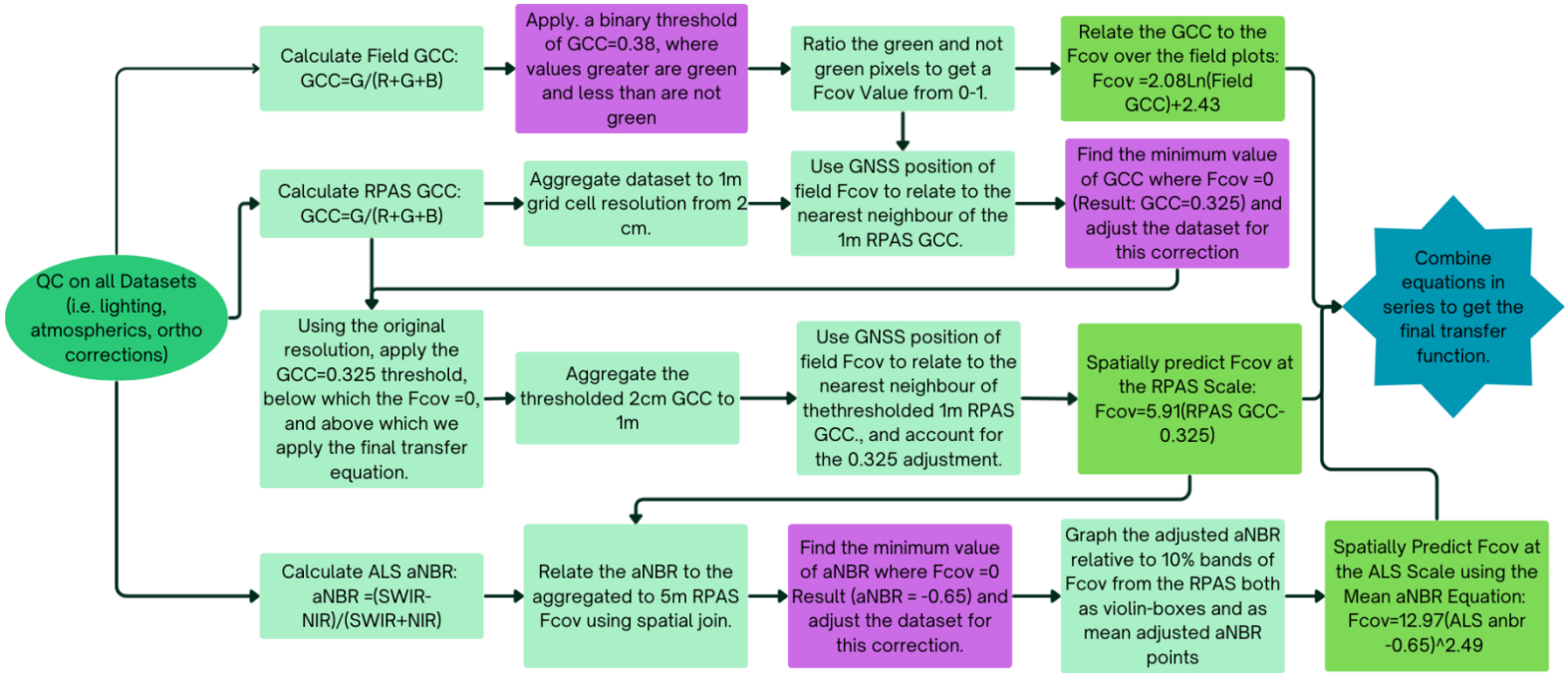

Figure 2.5: A flowchart diagram of the logic employed, and the resulting functions taken to scale Fcov measurements from a sub-centimeter grid cell resolution at the field photography scale, to Fcov predictions at 5m airborne resolution, using the RPAS imagery as an intermediate scale. The dark green circle represents pre-processing, mint green boxes describe processes, purple highlights threshold decisions, lime green highlights equation results, and the blue star shows the final product.

2.3.3.6. Vegetation Growth Trajectories and Spectral Index Saturation

Once the models for height and Fcov were developed for each year in Cameron Valley (CV) since the fire, these equations were applied to the unburned regions of CV and the burned areas of Lynx Creek and West Castle Watershed, to develop a hypothetical timeline for estimating future Fcov and height changes. These comparison areas, which represent different stages of post-fire regeneration, can provide insights into what the vegetation regeneration trajectories could look like as CV continues to recover in the next 10 to 100 years. Additionally, future vegetation growth trajectories provide insight as to when measuring vegetation height becomes the more useful measure of vegetation growth rather than vegetation cover, as vegetation cover will saturate once the area is 100% covered, or there is no more space or capability of the land to increase in vegetation cover based on other natural constraints such as soil type, water availability, and local terrain.

Saturation rates for Fcov were determined using all scales of data, to determine at what point in time the Fcov in each site reaches maximum cover. This was done by first running a Kruskal-Wallis test (KW) on the field data to determine whether there was any significant difference in growth between or within any years within the sites as this test compares differences between and within sets of non-parametric data. Then a Mann - Whitney (MW) test was applied to find if there was a significant difference in vegetation growth between two years at a time to determine the point at which there is no significant increase in vegetation greenness and cover in the field plots. Regeneration trajectories regarding saturation rates of greenness and cover were calculated using a linear function

comparing cells over the same location, and the point at which the greenness no longer demonstrated a significant increase from year to year was determined as the saturation point. At this point, it is expected that greenness and cover have reached the maximum possible value. Since some areas were never vegetation covered prior to the fire, the site cannot reach 100% greenness or cover. Therefore, the point of saturation is defined as the time at which there is no significant difference in greenness or cover between at least two years or comparison time periods. Beyond this point, height becomes the more useful metric of vegetation growth. Future trajectories of vegetation greenness and height were developed using the aNBR and CHMs from West Castle Watershed and Lynx Creek, as well as the unburned areas of CV.

2.4. Results

2.4.1. The Developed Monitoring Framework

Table 2.4 describes the developed framework used to monitor post-fire vegetation, which was applied in this study. This framework is the general overview of all methods applied. Specific methods related to the scale transfer function are described in Section 2.3.4.4. and Figure 2.5.

Table 2.4: The stepwise framework developed and applied to monitor vegetation changes in Cameron Valley. This framework is used in conjunction with the transfer methods described in Figure 2.5

Step	Dataset	Methods
Data Collection 1	Field Data	Measure vegetation height, take photos
Data Collection 2	RPAS Data	Fly surveys to collect lidar and photos
Data Collection 3	Airborne Lidar Data	Fly survey to collect multi-spectral lidar
Data Correction 1	All Datasets	Georeference all data
Data Correction 2	RPAS and Airborne Height	Set grid cells >3m tall to null in the burned areas
Data Correction 3	Photography and Lidar Spectral Information	Correct lighting conditions, compare cameras
Data Analysis 1	Height information all scales	Regress height from field to RPAS, then RPAS to airborne
Data Analysis 2	Field and RPAS Photography	Calculate GCC at the original resolution
Data Analysis 3	Airborne lidar NIR and SWIR	Calculate aNBR at a 1 m grid from the point cloud; aggregate the 1 m grid to a 5 m grid using the mean
Data Analysis 4	Field GCC	Apply a binary threshold of GCC= 0.38 to determine Fcov for each photo (approximiately 1m²)
Data Analysis 5	RPAS GCC	Aggregate by mean to a 1 m grid cell
Data Analysis 5	Field Fcov and RPAS GCC (1 m)	Directly relate RPAS GCC with Field Fcov photos, generate a prediction model, correct the RPAS GCC to predict from 0 to 100% Fcov
Data Analaysis 6	RPAS Fcov (1m)	Aggregate by mean to a 5 m grid cell
Data Analysis 7	RPAS Fcov (5m) and aNBR	Directly relate RPAS Fcov to the aNBR, adjust the aNBR to predict from 0 - 100% Fcov
Final Product	Airborne Fcov (5m)	Apply the derived equations for calculating Fcov from lidar to each dataset of interest for comparisons over time

2.4.2. Pre-processing Camera Band Comparison

Systematic bias detection results between combinations of handheld field cameras and RPAS imagery are presented in Figure 2.6 and Table 2.5. The camera system combinations were substantially similar and therefore no calibration equations were applied to the sensors prior to use in greenness calculations.

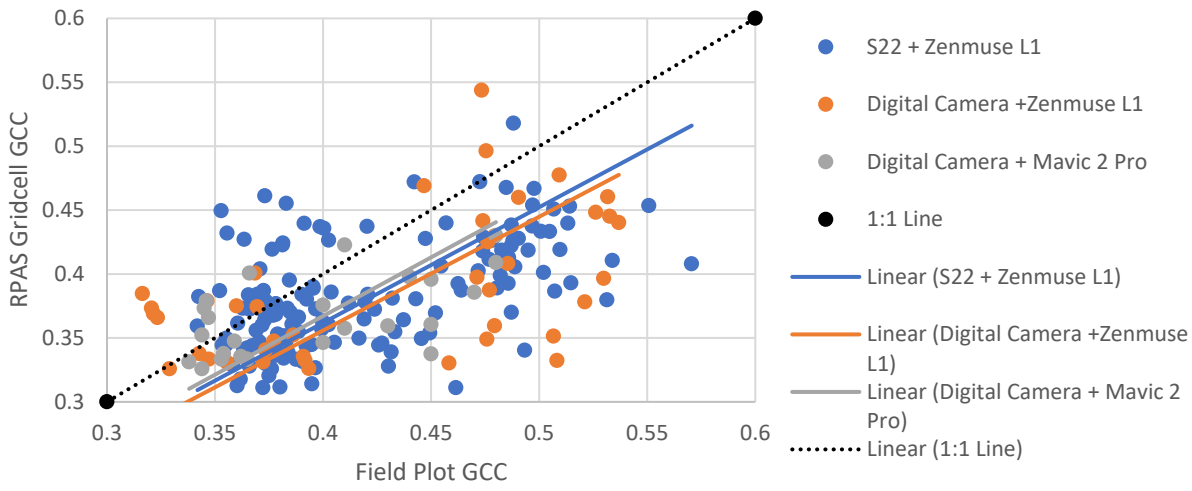

Figure 2.6: The field camera and RPAS sensor combinations, comparing the GCC of the field plot data to the corresponding RPAS GCC value at a 1m grid cell, demonstrating no significant differences between the sensors regarding potential for systematic bias in the spectral response.

Table 2.5: The associated camera systems, r^2 values, and equations of the linear regression between the field camera and the RPAS camera demonstrated in Figure 2.6.

Camera Systems	**Equation**	**r^2**
S22+Zenmuse L1	0.905x	0.99
Digital Camera +Zenmuse L1	0.890x	0.97
Digital Camera +Mavic 2 Pro	0.918x	0.99

2.4.3. Multi-scalar Height Comparisons

The resulting calculations of the field and RPAS height descriptive statistics are included in Appendix A, and they show that height measurements from year to year had high variance. The height measurements over the period of 2018 to 2024 over the Cameron valley did not scale well between spatial scales and types of data. Figure 2.7 and Figure 2.8 show the relationships between the field, RPAS, and airborne lidar height measurements over zonal and grid cell scales. The best performing model had an r^2 of 0.08, but this model also had an RMSE of 0.40 which is high for the scale of the data range, indicating that this model is too noisy to be useful within the first several years following the fire.

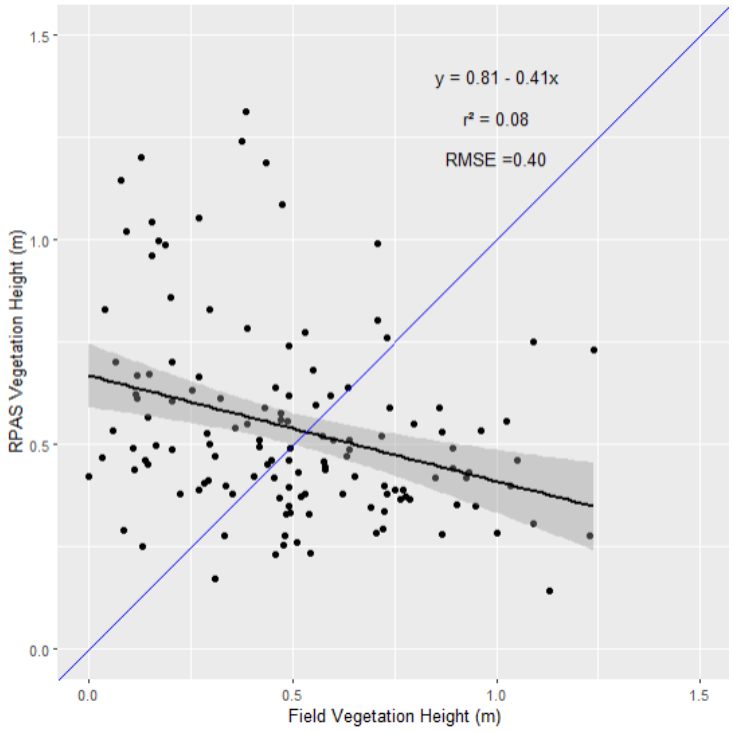

Figure 2.7: Comparison of field plot height measurements and RPAS CHM grid cell height measurements. The red line is the linear relationship with the shaded portion representing the confidence interval, and the blue dashed line is the 1:1 relationship.

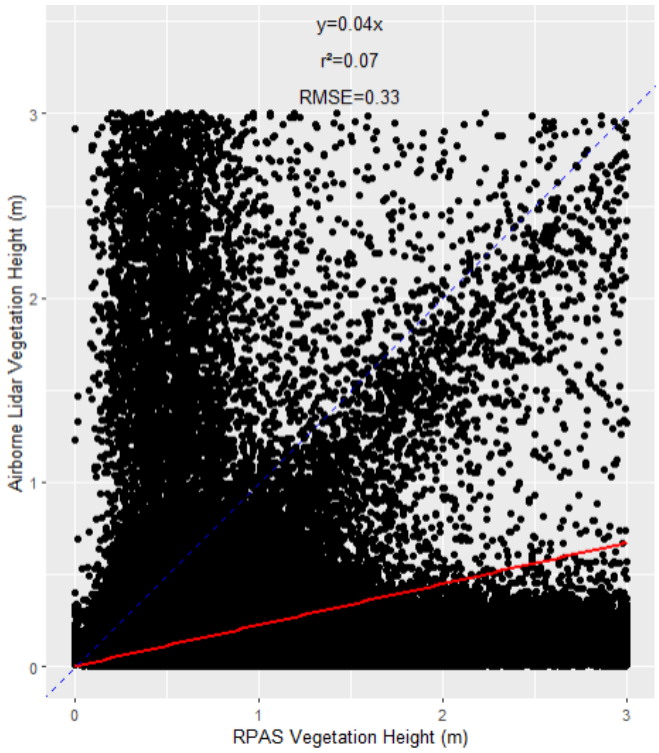

Figure 2.8: Comparison of RPAS CHMs at the 1m grid cell spatial resolution to airborne lidar CHMs over the RPAS polygons.

Height measurements are highly variable in the first seven years following a fire due to interannual hydrometeorological conditions and the mix of herbaceous and woody vegetation in the species succession. Once the vegetation regime is dominated by tall woody vegetation, as observed in Lynx Creek, West Castle Watershed, and the unburned regions of Cameron Valley, structural lidar measurements become more effective. Therefore, it is expected that height measurements in the burned area will become more accurate and robust after ten to fifteen years of post-fire regeneration (Figure 2.9), when the seedlings become more established and grow consistently taller than the annual herbaceous vegetation.

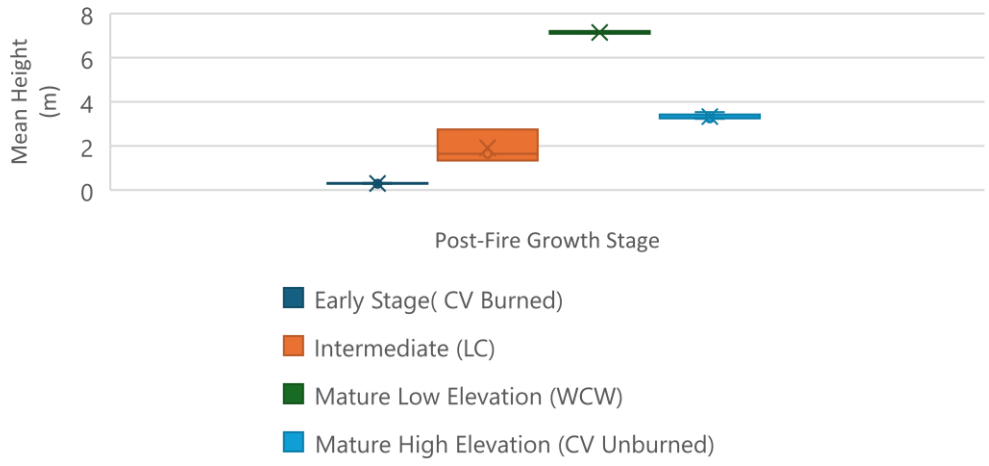

Figure 2.9: Box plots representing CHM distributions at the different regeneration stages. Early stage refers to the first 7 years following the fire, intermediate is a 20-year recovery state, late stage is approximately 90 years, and mature forest is the unburned area of CV, which burned over 100 years ago, and most of the region is above 1800masl to treeline at 2300masl, and therefore the trees are shorter in this area.

2.4.4. Transferring Greenness and Fractional Cover Between Scales

The greenness indices were significantly related between measurement scales, demonstrating a consistent measure of greenness change over time between the sensors and scales (Figure 2.10).

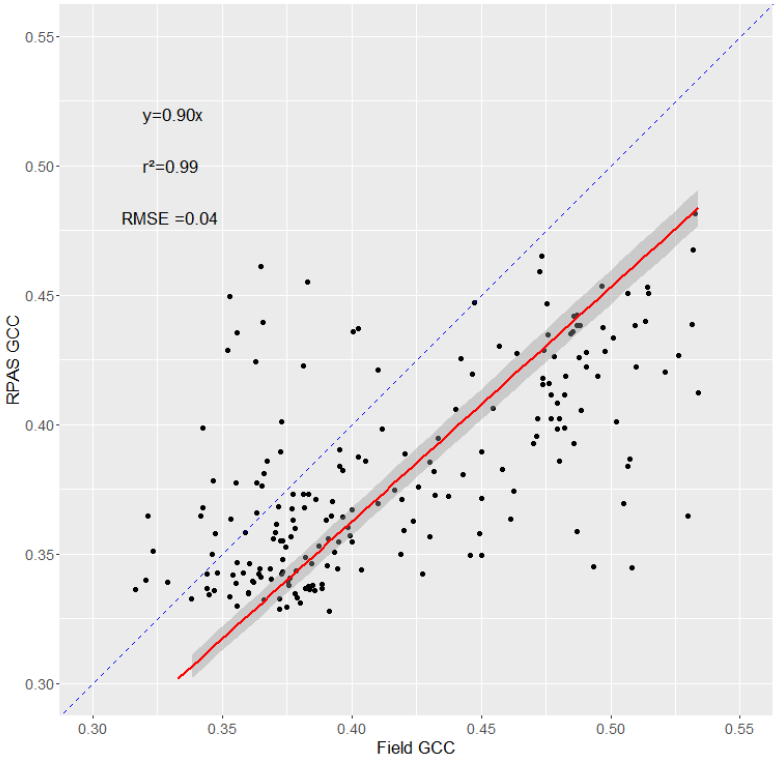

A)

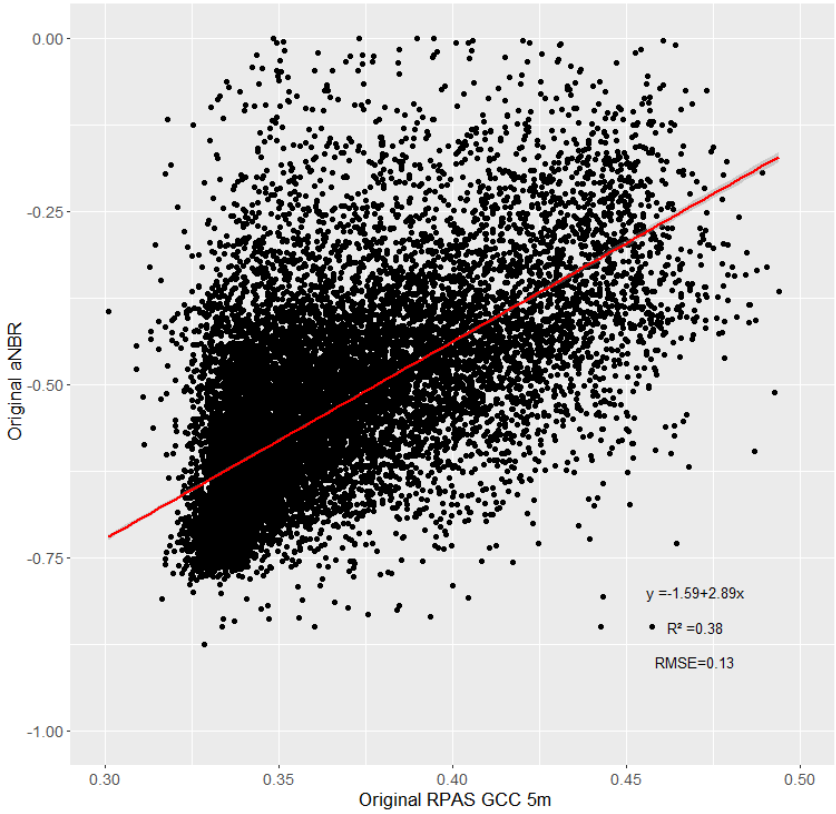

B)

Figure 2.10: A comparison of the greenness indices across scales, from field GCC to RPAS GCC (A) then RPAS GCC to airborne lidar aNBR (B).

Since the spectral indices relate well between scales, the transfer function for Fcov started with the field plot scale, as demonstrated in Figure 2.11, which compares the field photo mean GCC to the Fcov ratio generated from the binary threshold of green and non-green pixels. The relationship in Figure 2.11 is the basis for the rest of the model transfer, as the resolution is high enough to resolve many of the mixed pixel effects, therefore giving a clear measurement of Fcov.

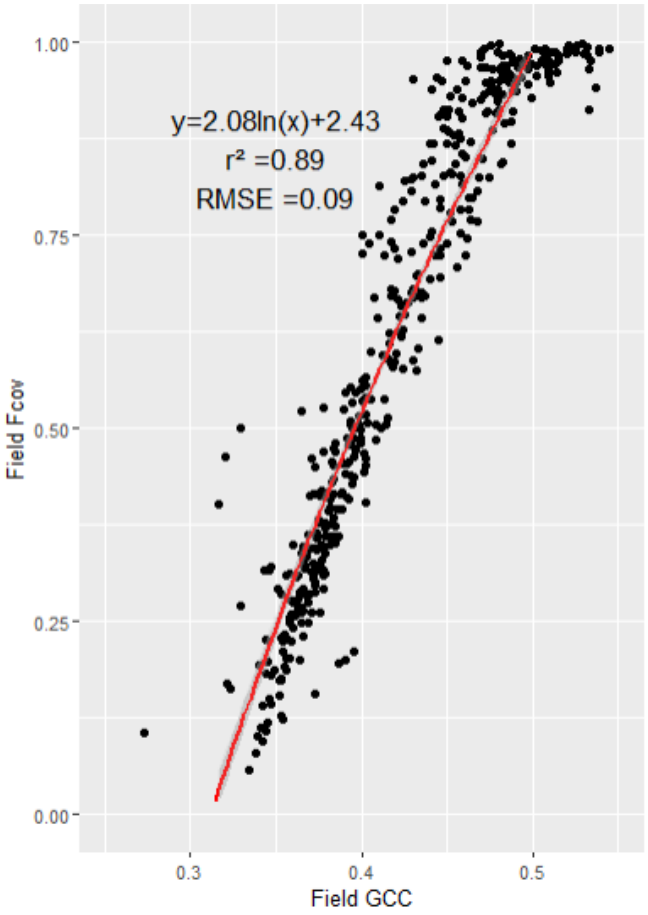

Figure 2.11: The relationship between the mean field photo GCC and the calculated Fcov derived from the ratio of the binary threshold photo.

Figure 2.12 utilizes the relationship developed in Figure 2.11(y=2.08ln(x) +2.43) to find the GCC value at which a Fcov of zero is predicted, and shows the adjusted

relationship using this value, moving the prediction scale to run from 0 to 0.3, and a shift in the equation for predicting RPAS Fcov from the field Fcov to GCC relationship, as presented in Table 2.6.

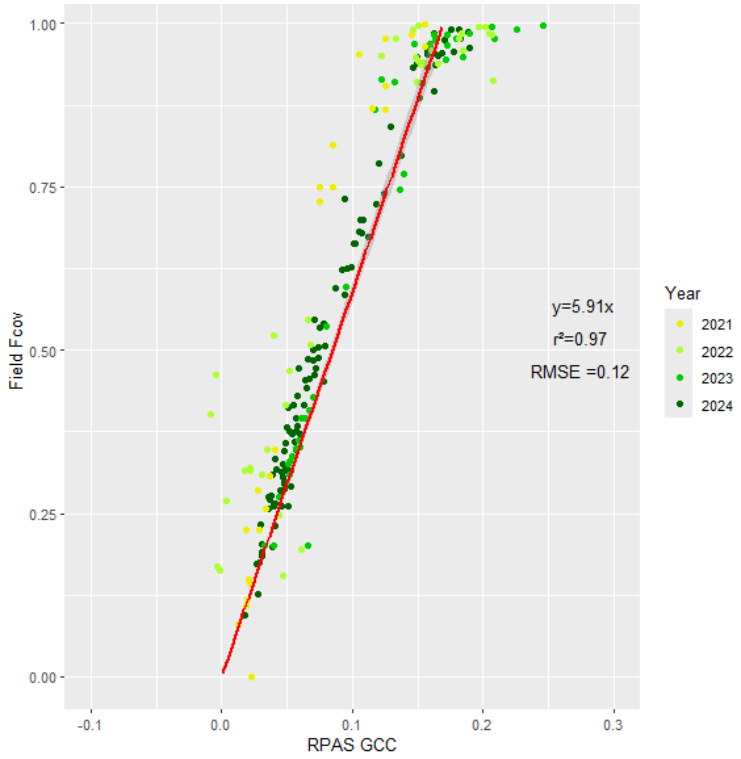

Figure 2.12: The adjusted prediction for Fcov at the RPAS scale using the corrected GCC values, with points colourized by year of data collection.

Table 2.6 and Figure 2.13 show the results of predicting Fcov from the RPAS GCC datasets based on the field GCC to Fcov model demonstrated in Figure 2.12. This model was selected as the basis for predicting Fcov at all scales due to the high spatial resolution reducing the mixed pixel effect. Table 2.6 also shows the resulting Fcov values for each RPAS dataset at the 5 m spatial resolution, which are critical for the final upscaling process to airborne lidar.

Table 2.6: The information resulting from transforming the RPAS GCC to Fcov, then relating to the aNBR data over the same area. This includes the dataset specific natural breaks threshold for determining the zero percent cover value in the GCC raster, the ranges of each spatial resolution for each step of upscaling, and aggregation multiplier to get from approximately 2 cm raster to 1m raster.

Dataset	**Binary Threshold Natural breaks at approximately 2cm resolution**	**2cm GCC Range**	**Aggregation from 2cm to 1m Cell Factor Multiplier**	**1m GCC Range**	**1m GCC - 0.325 range**	**Fcov Range 1m**	**Fcov Range 5m**	**aNBR Range 5m**
DS18	0.36	0.289-0.556	77	0.325-0.431	0-0.106	0-0.628	0-0.495	-0.737 – -0.328
DS21	0.358	0.251-0.56	67	0.325-0.427	0-0.102	0-0.601	0-0.514	-0.654 – -0.113
DS22	0.384	0.172-0.866	63	0.325-0.4875	0-0.163	0-0.960	0-0.88	-0.585 – -0.091
DS23	0.38	0.094-0.926	58	0.325-0.480	0-0.155	0-0.919	0-0.864	-0.632 – -0.007
DS24	0.381	0.033-0.9189	55	0.325-0.480	0-0.155	0-0.919	0-0.869	-0.624 – -0.101
MS18	0.359	0.222-0.778	78	0.325-0.452	0-0.127	0-0.749	0-0.528	-0.726 – -0.113
MS21	0.377	0.252-0.606	60	0.325-0.449	0-0.124	0-0.734	0-0.668	-0.605 – 0.011
MS22	0.404	0.127-0.848	39	0.325-0.518	0-0.193	0-1.141	0-1.060	-0.501 – 0.009
MS23	0.406	0.083-0.875	52	0.325-0.492	0-0.167	0-0.985	0-0.903	-0.506– 0.034
MS24	0.392	0.080-0.900	50	0.325-0.506	0-0.181	0-1.071	0-0.767	-0.554– -0.120
SE18	0.343	0.309-0.442	33	0.325-0.385	0-0.030	0-0.365	0-0.267	-0.736– -0.400
SE19	0.378	0.138-0.833	57	0.325-0.509	0-0.184	0-1.087	0-0.920	-0.757– -0.134
SE21	0.357	0.260-0.542	51	0.325-0.441	0-0.116	0-0.686	0-0.506	-0.652– -0.229
SE23	0.380	0.133-0.824	40	0.325-0.478	0-0.153	0-0.905	0-0.817	-0.625– -0.118
SE24	0.383	0.048-0.938	39	0.325-0.481	0-0.156	0-0.922	0-0.863	-0.634– -0.198
NW18	0.358	0.297-0.511	48	0.325-0.429	0-0.104	0-0.612	0-0.492	-0.733– -0.347
NW19	0.381	0.178-0.773	70	0.325-0.523	0-0.198	0-1.171	0-0.936	-0.712- -0.114
NW21	0.362	0.268-0.588	58	0.325-0.431	0-0.106	0-0.624	0-0.517	-0.655- -0.053
NW23	0.379	0.103-0.950	60	0.325-0.486	0-0.161	0-0.950	0-0.821	-0.633- -0.106
NW24	0.392	0.038-0.959	56	0.325-0.497	0-0.172	0-1.014	0-0.924	-0.625- -0.184

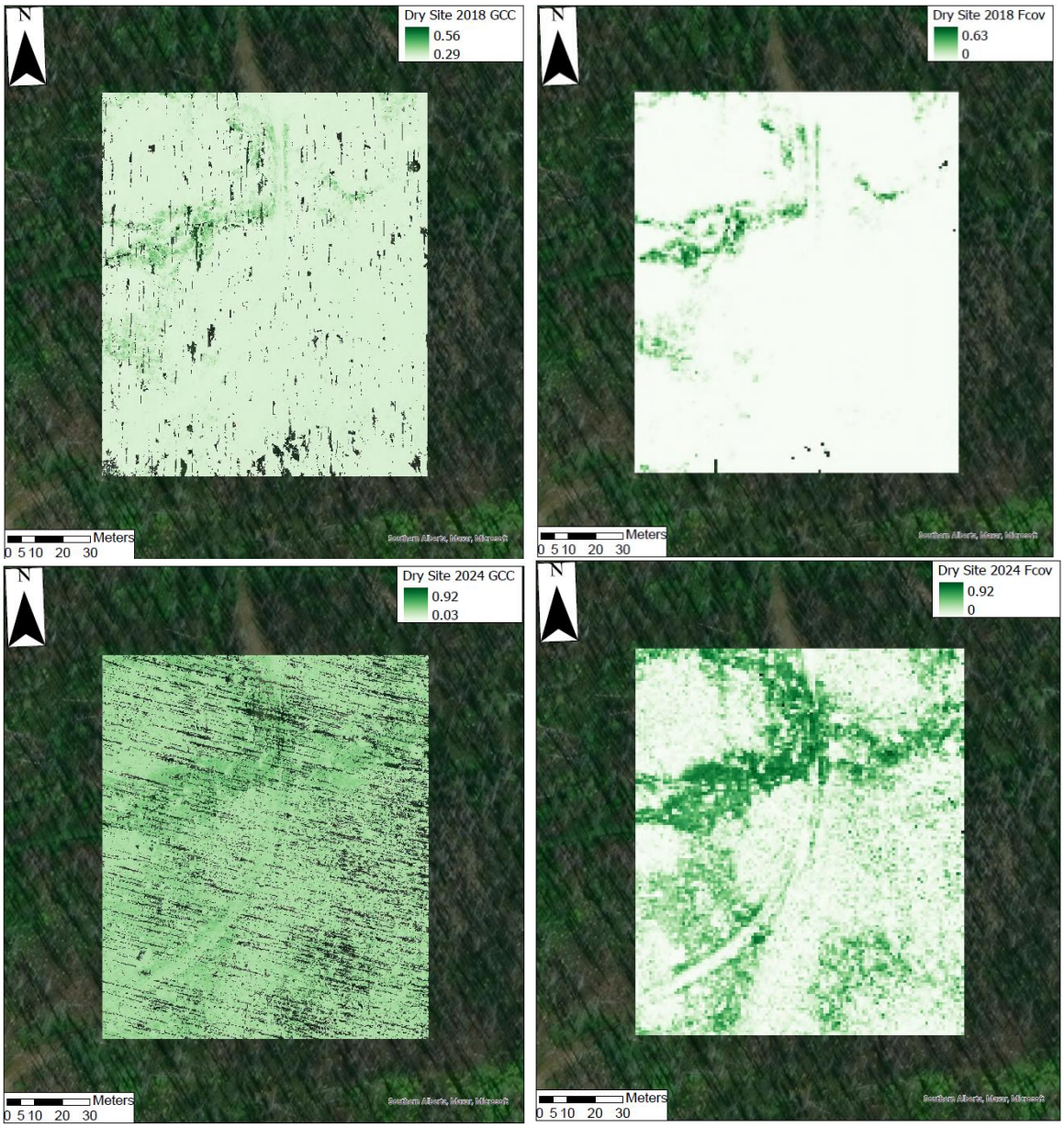

Figure 2.13: The GCC (2cm) and Fcov (1m) for 2018 and 2024, demonstrating the spatial prediction of Fcov from GCC at the RPAS scale in the Dry Site.

Figure 2.14 shows the relationships developed between RPAS Fcov and aNBR over a 5 m grid cell. The second model presented was adjusted to allow for accurate prediction of zero Fcov from aNBR. The resulting airborne lidar dataset descriptive statistics following the aNBR transform into Fcov using the relationship between aNBR and RPAS Fcov at a 5m grid cell are presented in Table 2.7.

Figure 2.15 shows the relationship equation used for predicting Fcov spatially, and it is based on the RPAS values after parsing into 10% increment bands, and the adjusted aNBR as presented in Table 2.6 and Figure 2.14b.

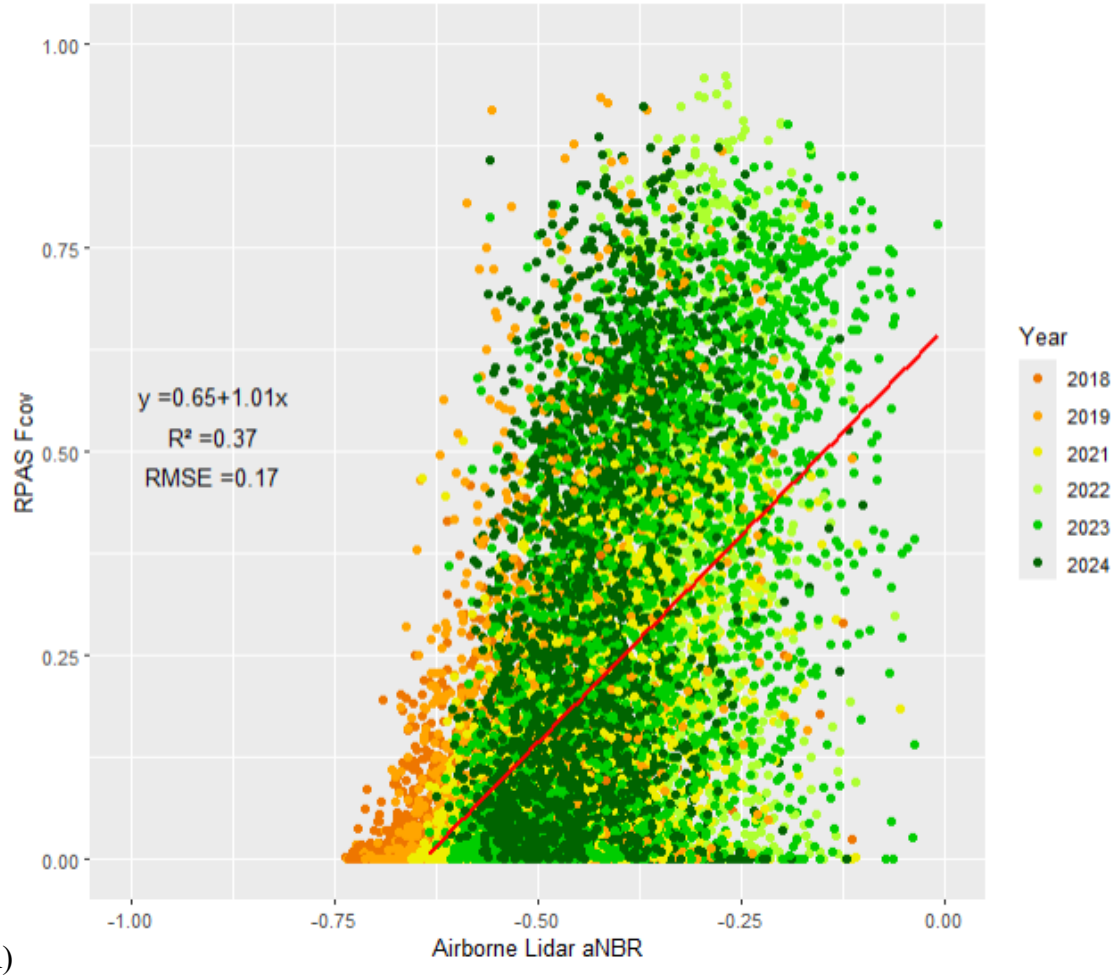

A)

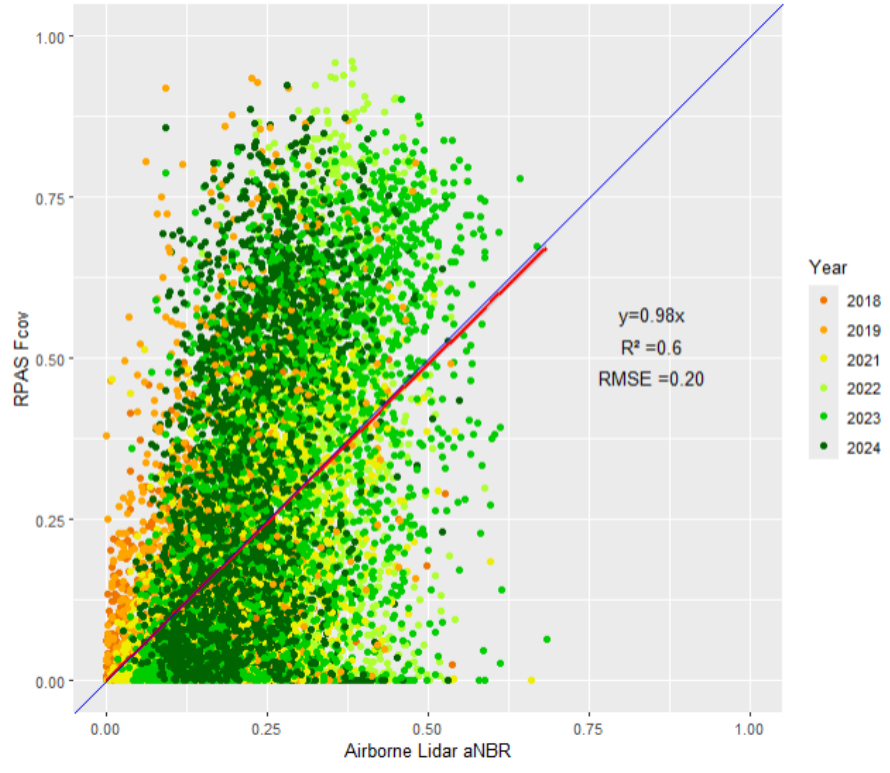

B)

Figure 2.14: The relationship between airborne lidar aNBR and RPAS Fcov at a 5m grid cell resolution for the purpose of predicting Fcov at the airborne lidar scale, using a) the original aNBR values, and b) the adjusted values using the x intercept of model A for predicting regions of zero cover.

Table 2.7: The numerical results of the aNBR to Fcov transformation based on the upscaling equation system in the burned area of CV.

Dataset	aNBR Original Range	aNBR Original Mean	aNBR Original Standard Deviation	aNBR Adjusted (+0.65) Range	aNBR Adjusted for 0-1 Range Mean	aNBR Adjusted for 0-1 Range Standard Deviation	Fcov Mean	Fcov Standard Deviation
2018	-0.998 0.999	-0.594	0.098	-0.344 1.64	0.065	0.089	0.07	0.17
2019	-0.938 0.778	-0.476	0.149	-0.388 1.328	0.104	0.116	0.15	0.25
2020	-0.900 0.925	-0.480	0.112	-0.250 1.575	0.171	0.110	0.25	0.29
2021	-0.926 0.966	-0.484	0.111	-0.276 1.616	0.167	0.110	0.33	0.29
2022	-0.996 0.981	-0.416	0.117	-0.347 1.631	0.234	0.115	0.41	0.34
2023	-0.833 0.782	-0.461	0.108	-0.183 1.432	0.189	0.108	0.29	0.30
2024	-0.823 0.919	-0.443	0.111	-0.173 1.569	0.207	0.108	0.33	0.31

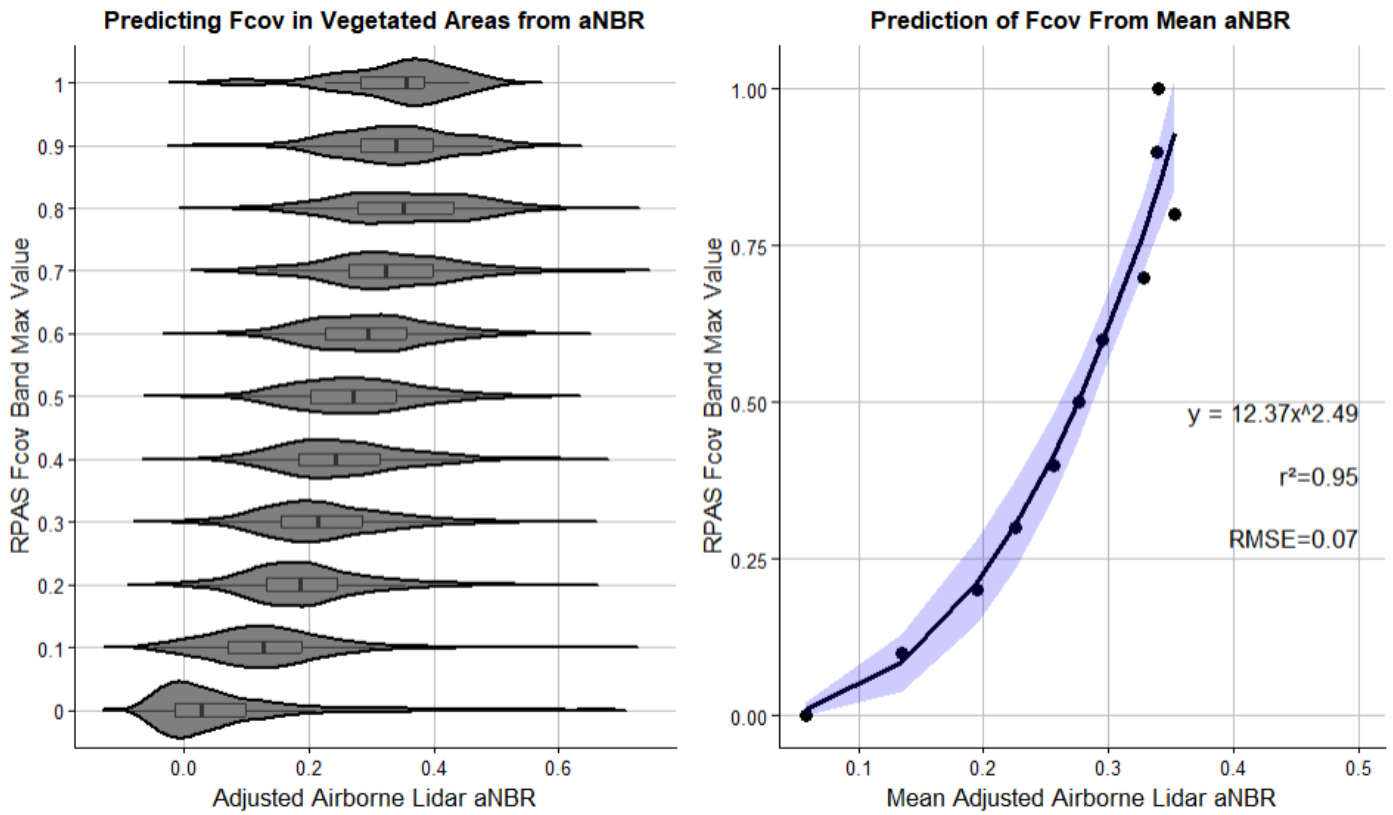

Figure 2.15: The 5m grid cell resolution comparison between a) RPAS GCC and aNBR, with the data binned per 0.1 total cover, showing the mean, distribution, and standard deviation of each bin b) RPAS Fcov and airborne lidar Fcov for all sites and years (with a confidence interval in blue).

Since Fcov can be transferred between measurement scales at the grid cell level using the series of functions presented in

Figure 2.15, the final function which demonstrates the transfer of field information to airborne lidar information is demonstrated in the equation series in Equation 2.4.

Equation 2.4: The series of equations below for the transfer of Fcov between scales for values of Fcov >0:

$$\text{Field Greenness to Cover: } Fcov = 2.43+2.08Ln(\text{Field GCC})$$

$$\text{Transfer to RPAS: } Fcov = 5.91(\text{RPAS GCC}-0.325) : \text{where GCC} \geq 0.325$$

$$\text{Transfer to Airborne lidar: } Fcov = 12.37(\text{aNBR} +0.65)^{2.49} : \text{where aNBR} \geq -0.65$$

The resulting Equation series 2.4. was applied to the datasets to generate spatial predictions of Fcov across the entire Cameron Valley, as demonstrated in Figure 2.16. The equation was applied to the unburned areas in Cameron Valley, as well as the burned areas of LC and WCW to see the saturation rates, as shown in Figure 2.17. The unburned region demonstrated consistent Fcov values as expected. However, since much of this area is above treeline for capturing short, high alpine vegetation, such as that observed on the slopes of Mount Carthew in the southeast region of the lidar of CV, it is expected that the Fcov is lower in this area than in the valley areas of the comparison sites, as shown in Figure 2.17.

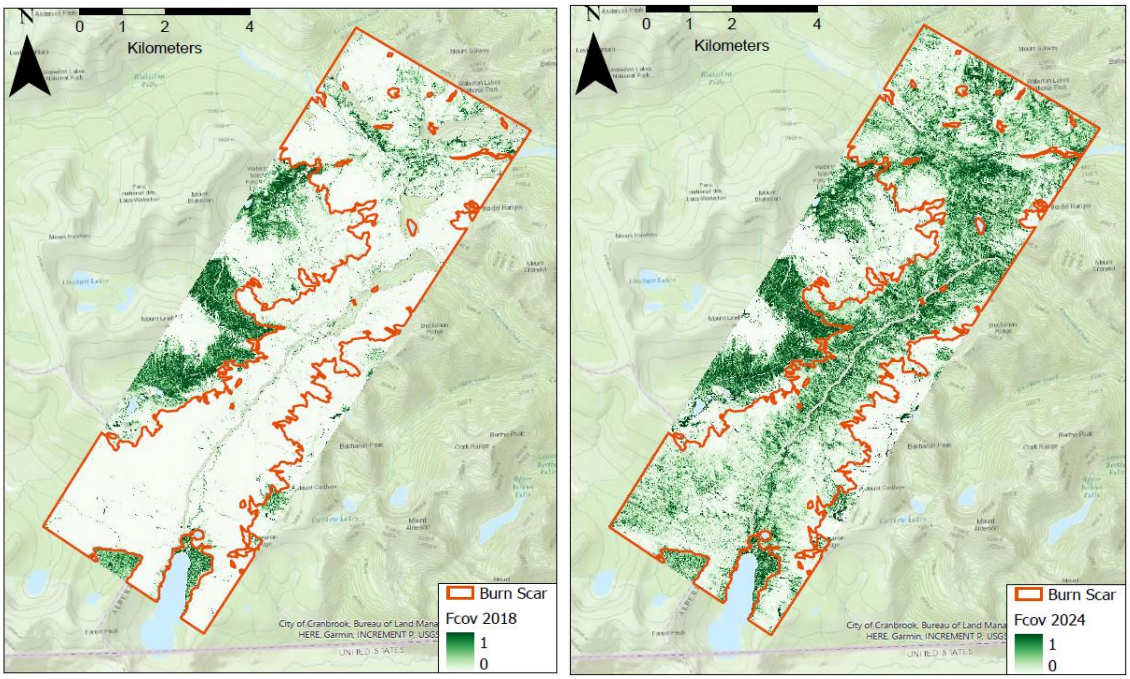

Figure 2.16: Fcov across CV in 2018 and 2024 as predicted from aNBR using the model scale transfer function.

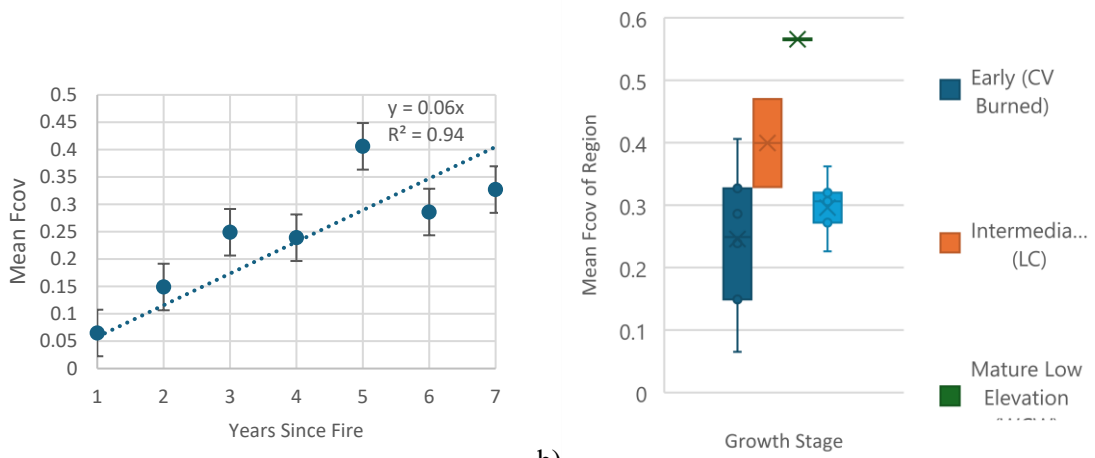

a) b)

Figure 2.17: The trajectory of Fcov change in the early years of post-fire regeneration in the burned area of Cameron Valley showing the mean and standard error (a), and box plots of the mean Fcov in different post-fire conditions, including the early state, approximately 20 years post fire (LC), 90 years post fire in lower elevations (<1800masl) and over 100 years post-fire in higher elevations (>1800masl), with the means represented as an x, whiskers are standard deviation, and circles are data values (b).

The future projections for aNBR shows us that greenness saturates approximately eight years following across the burn scar. Saturation occurs at the point in time where there is no longer a significant increase in mean greenness over the same area from year

to year, based on the two-sample equal variance t-test. The moist site saturated after 5 years, and the dry site reached saturation in 2023 after 6 years (Appendix A). Since only two years of in-situ data have been collected for the NW and SE sites, it is not yet possible to determine whether these sites have saturated in greenness at this scale. Across the entire scale, it is expected that greenness and cover saturate between 5-10 years, depending on the specific region of the valley. Once these reach saturation, it is not as useful of metric to monitor longer time scale vegetation recovery, and it is at this point height measurements should be used instead.

2.5. Discussion

2.5.1. Vegetation Growth Since the Fire

Vegetation is recovering in the severe fire zone across all sites and scales. This is expected as one of the majority species of seedling is lodgepole pine (*Pinus contorta*), which has serotinous cones that release their seeds in extreme heat, such as wildfires (Lotan et al., 1985). Other species that do well shortly following fires include fireweed and other various species of grasses (Aspinall, 2023; Chappell & Agee, 1996). As the herbaceous plants begin to get established, they can quickly expand and cover the area, resulting in the saturation of the indices (Appendix A, Aspinall et al. 2025).

2.5.2. Limitations in Transferability of Height Models in Early-Stage Post-Fire Environments

Height is variable in the first several years of post-fire recovery, as much of the herbaceous vegetation is influenced by annual weather patterns including moisture and temperature inputs, and some species grow tall (>2m) quickly such as grasses and fireweed, while other species reach their maximum height very early on, such as ground cover species like wild strawberry (Kuijt, 1982). The species variance annually can

change significantly depending on the climate conditions and any pre-existing seed bank remaining following the fire (Littlefield, 2019). The species dominance of each year can determine the height, for example, in 2021, the sites contained higher proportion of wheatgrass species, which were consistently growing to approximately 1.5-2 m tall based on field observations. These grasses resulted in the field data height measurements reporting maximum values higher than what the lidar measurements could pick up, due to the small size of the target (a single blade of grass) and relatively larger laser footprint of the Titan (Hopkinson et al., 2016; Hopkinson et al., 2006). Additionally, another limitation of the Titan system, is that it has a minimum target separation of approximately 1m in vertical distance (Teledyne Optech, 2023). This refers to the space in between laser pulses as the laser requires a minute amount of time to recharge and emit the next pulse. The time space between pulses is the 'dead zone' and is a limitation on the accuracy of CHMs for early-post fire vegetation, as the dead zone occurs at approximately the same height above the ground as the live vegetation (Hopkinson et al., 2006). Therefore, when combining the variance in the vegetation height with the lidar resolution limitations, there is significant noise in the datasets which makes them unusable for determining significant differences in vegetation height in the study period. However, as the woody vegetation from shrubs and seedlings continues to increase, it is anticipated that height measurements will become less variable from year to year, and vegetation will be more consistently measured using the CHM than cover in the future, as is the typical practice in managed and older forests (Hopkinson et al., 2016; Hopkinson, Chasmer, et al., 2004; St-Onge & Achaichia, 2001). Therefore, in newly burned areas, it is recommended to measure vegetation cover until it reaches saturation, which is the point at which the site

shows know significant increase in cover between one year and the next (between 5-8 years post-fire), and at that point, start measuring height instead, as it will start to become more consistent.

2.5.3. Influences of Spatial Resolution on Fcov Model Upscaling Accuracy

Both greenness indices (GCC and aNBR) were found to be effective for predicting vegetation cover over small zones, and the GCC was effective for predicting vegetation cover at the 1 m (Figure 2.11) and 5 m (Figure 2.15) grid cell level. This corroborates work done by Liu, et al. (2021) who used cell phone images and GCC to determine fractional cover in grasslands. The GCC is an effective greenness index for determining fractional cover over a specified area. The vegetation fractional cover models also scaled well between the field and RPAS surveys, and then the RPAS and airborne lidar surveys. While the error and mixed pixel effects compounded with each scale transfer, overall, the models determined that there were significant increases in cover in the burn scar in the study period. In WLNP at all measurement scales, vegetation cover was found to saturate within 5- 8 years of the fire. Therefore, vegetation cover is an accurate measure of vegetation growth in the early post-fire regeneration stage in the site, but beyond this period its efficacy for determining vegetation growth decreases and cover saturates.

Another source of error in the scaling is the issue of mixed pixel effects, which is a common source of error in remote sensing processes and land cover change studies regardless of the specific technology or system used in the study (Garrigues et al., 2006; Hopkinson et al., 2024; Peng et al., 2017). The ground sampling distance changes from sub-centimeter at the field plot level GCC, to decimeter at the RPAS level GCC, to 5m

grid cells at the airborne aNBR. While each measure the same area at the same time, the differences in the spatial resolution between each scale results in a different level of detail being resolved, and therefore, the accuracy at the field scale is the highest due to the high spatial resolution, and lowest at the airborne scale due to the lower spatial resolution. Each jump between scales results in some loss of accuracy and an increase in noise, which therefore results in an increase in error, presented with each relevant graph in the results section and Appendix A.

2.5.4. Sources of Error and Limitations

Despite all samples being collected in July of each year to help with normalizing weather conditions on the day of sampling, the interannual meteorological conditions likely influenced the vegetation growth. For example, 2021 showed increased vegetation heights compared to 2022. 2021 was a drier year compared to 2020 and 2022, and allowed for an excess quantity of taller wheatgrass species to grow compared to the years before and after, influencing the mean height measurements in the field plots (Aspinall et al., 2025). Additionally, snowpack maximums and durations change annually (Barnes et al., 2025), also impact seedling growth and retention, especially in lodgepole pine, which is one of the main succession species in the area (Pierce & Taylor, 2011). Therefore, even when sampling timing is precisely controlled, changes in moisture and temperature patterns alter the vegetation growth, increasing the variance in the measurements and models.

One of the difficulties of using lidar for structural post-fire vegetation regeneration detection is the presence of downed woody debris and other non-vegetative features such as cliff faces and boulders that can be mistaken as vegetation in the CHMs. Woody debris

is difficult to discern from live vegetation in CHM when it falls between the 0-2m height range, especially regarding fallen logs and stumps. Where the debris was taller than 3m, the values were set null to attempt to remove the influence of debris on the height measurements, but the logs and snags below this height would remain in the dataset. Cliff faces were not commonly occurring in the valley and in the burned area, but in the control region and in higher elevations they are more common. These were adjusted for by setting CHM values above 50 m null in unburned areas used in the future projections trajectories. Boulders are useful in aligning RPAS SfM and lidar data to the airborne lidar data, however, they have the same issues as the woody debris regarding potential height influences.

2.5.5. Future Work

Since Cameron Valley is still in the early stages of post-fire recovery, further monitoring of the site at all scales of data collection is recommended, especially for validating the future trajectory predictions of changes in vegetation height and cover over time. Since height changes were not significant in the first seven years of post-fire data collection, continued studies to find the year at which they become significant is recommended. Future vegetation monitoring studies should apply a multi-scalar approach to measuring vegetation cover and height, to both cover the detail on the ground for the causes of change over time in the region of interest, to validate the larger scale models, and to determine the rates of change. Additionally, biomass models could be applied using the cover models in the area, as suggested in Aspinall (2025) and Pearse (2024).

Other additional work could include hydrological modelling in the post-fire environment as it recovers, species quantification of trees and herbaceous succession, and

testing other greenness and cover indices could be useful in giving corroborative results. Additionally, applying the framework provided in this paper in Figure 2.5 and Table 2.4to model other post-fire sites would be useful for both validating the processes discussed here, and for increasing both the spatial coverage and resolution of the data collected and information derived in these remote sites.

2.6. Conclusions

Vegetation is significantly regenerating across the Cameron Valley at all scales. Cover is the more reliable and accurate method of measuring vegetation until approximately six years post-fire in riparian and moist areas, and up to eight years in drier upland areas and on slopes. Height is not an accurate measure of vegetation until approximately 10- 15 years following the fire due to the high variability of species and inter-annual meteorological conditions which influence annual herbaceous vegetation growth.

The combination of relationships between greenness indices at each scale, and the fractional cover at the field scale, can be used to effectively transfer fractional cover predictions from the high spatial resolution field scale to the low spatial resolution airborne scale. Multi-scale vegetation height measurements were not yet transferrable but likely will be once the annual variance decreases as the seedlings continue to grow in the next decades, as projected using the other comparison sites and control areas. Using a combination of data sources at different scales and relying on cover measurements in the first decade before switching to relying on height measurements is the vegetation regeneration monitoring framework proposed here. Post-fire regeneration is critical to measure and understand on the highly detailed field scale to the broader airborne scale for

predicting ecosystem recovery and dynamics as the environment continues to change in the future.

3. Chapter 3: Quantifying the Spatial Distribution of Early-Stage Post-Fire Vegetation Regeneration using Lidar in Waterton Lakes National Park, Alberta, Canada

3.1. Abstract

Wildfires in mountainous environments can significantly alter ecological and hydrological systems. Quantifying the spatiotemporal patterns of early post-fire recovery is critical for informing land management decisions and understanding ecosystem recovery in severely burned headwater regions. The Cameron Valley of Waterton Lakes National Park (WLNP) burned to high severity in 2017, so the research objective was to quantify the distribution of vegetation regeneration relative to terrain drivers for each year since the fire using multi-spectral lidar data. Lidar surveys were collected during peak phenology each summer to determine the maximum vegetation cover and height. These vegetation metrics were spatially stratified by five terrain drivers: elevation, slope, aspect, topographic position index (TPI), and terrain curvature (TC). Each terrain driver acts as a proxy for hydro-climatological influences, such as temperature, solar radiation, soil depth, and moisture accessibility, which are critical in supporting vegetation growth. Elevation, slope, TPI, and TC were significantly related to vegetation cover regeneration in the burn scar each year. Maximum cover occurred at 1600 masl on shallow slopes and in local topographic concavities. Mountain forest vegetation is relative to terrain, and therefore mapping the patterns of vegetation regeneration is critical for understanding the dynamics of ecosystem recovery, especially as wildfires continue to occur in the Rocky Mountains.

3.2. Introduction

Wildfire significantly alters forested mountain environments by removing much of the vegetation, changing ecological succession, hydrological pathways, and geomorphological behavior. Post-wildfire recovery can be significantly influenced by the burn severity, seed banks, terrain, and hydrometeorological conditions (Aspinall et al., 2025; Chappell & Agee, 1996; Rother et al., 2022; Turner et al., 1997). Quantifying the vegetation regeneration following an intense fire is critical for understanding succession pathways (Chappell & Agee, 1996; Schoennagel et al., 2003; Turner et al., 1997). Vegetation is also highly influential on local hydrology, affecting the water balance and flow pathways (Bladon et al., 2014; Niemeyer et al., 2019; Robinne et al., 2020). Understanding influences on the watershed is critical for water resource management decisions. Therefore, determining the patterns and rates of vegetation regeneration in burn sites is critical for ecosystem management and planning.

In mountainous environments, vegetation growth is related to a variety of terrain drivers, including elevation, aspect, slope, terrain curvature (TC) and topographic position index (TPI) (Letts et al., 2009; McCaffrey, 2018; Zou et al., 2023). These terrain drivers, which can be mapped using digital elevation models (DEMs) derived from remote sensing technology such as lidar (light detection and ranging) are useful proxies for other environmental conditions (Cobby et al., 2001; McCaffrey, 2018). For example, elevation change, specifically in mountainous regions, is often associated with both decreasing air temperature and increasing precipitation lapse rates (Barnes et al., 2025; López-Moreno, 2005; Zou et al., 2023) due to the reduced atmospheric pressure at higher elevations and therefore reduced vapour pressure deficit. Directional aspect is associated both with air

temperature and solar radiation inputs, as south facing slopes receive more direct solar radiation energy than north facing slopes (Cartwright, 2018; Goulden et al., 2016; Marsh et al., 2012; McCaffrey, 2018). Aspect can also be associated with wind direction, especially in regions with prevailing wind directions, such as the southern Alberta Rocky Mountains, where the prevailing wind direction is southwest to west, creating chinooks on the leeward side of the mountain range (MacDonald et al., 2018; Oard, 1993). Slope, TC, and TPI are proxies for hydrologic connectivity through a region, soil depth and water table levels, as these are associated with gravitational and erosional effects on the landscape (Aspinall et al., 2025; Cartwright, 2018; Gerrand et al., 2021; Thompson & Moore, 1996). Since soil quality and moisture levels are critical to vegetation growth (Aspinall et al., 2025; Day et al., 1989; Gerrand et al., 2021; Thompson & Moore, 1996), these terrain drivers can provide information on regions of the site that may be most productive.

One method of monitoring environmental change is to use remote sensing technology such as airborne lidar. Lidar uses lasers at specific wavelengths to survey the area, measuring the range, or distance between the target and the sensor, and the intensity of the energy which is reflected back to the sensor from each return (Baltsavias, 1999; Hopkinson et al., 2016; Hopkinson, Chasmer, et al., 2004; Hopkinson et al., 2006; Wehr & Lohr, 1999). The multiple return ability of lidar allows for mapping the forest canopy as well as the bare earth terrain, allowing for measurement of changes in forest canopy height over time with repeated surveys (Hopkinson et al., 2016; Lim et al., 2003; St-Onge & Achaichia, 2001). Additionally, the multi-spectral lidar systems such as Teledyne Optech's 'Titan' (2023), uses three laser wavelengths: green at 532 nm, near infrared

(NIR) at 1064 nm, and shortwave infrared at 1550 nm (Aspinall et al., 2025; Barnes & Hopkinson, 2022a; Chasmer et al., 2017; Hopkinson et al., 2016). These wavelengths can be combined to develop vegetation indices to measure vegetation cover over a region (Chapter 2). One index is the active normalized burn ratio (aNBR), which uses the NIR and SWIR wavelengths (Chasmer et al., 2017) , and can be used as a proxy for vegetation cover (Aspinall et al., 2025), especially in regions where fractional cover derived from the lidar point cloud is unreliable, such as in newly burned regions and early-post fire recovery sites (Chapter 2). The bare earth terrain surface derived from lidar provides a digital elevation model (DEM). From the DEM, terrain drivers such as directional aspect and slope, can be derived (Chasmer et al., 2017; Goulden et al., 2016; Hopkinson et al., 2008). The use of lidar over time in repeated annual surveys allows for change detection analysis, such as detection of post-fire vegetation regeneration.

Mountainous post-fire vegetation regeneration is highly heterogeneous in distribution; therefore, the objectives of this research are to quantify the spatial distribution of early-stage post-fire vegetation height and cover for each year in the first seven years in the early post-fire environment of Waterton Lakes National Park, Alberta, Canada, and to find if any specific terrain drivers are significantly related to early vegetation regeneration. The relationship between vegetation regeneration and specific drivers including elevation, aspect, slope, terrain curvature, and topographic position index, will be tested, to determine whether early post-fire vegetation is correlated with any of these drivers. Monitoring the spatial distribution of vegetation in post-fire sites is critical for understanding how mountainous regions will recover from significant forest

disturbances such as wildfire, and for informing model development for ecosystem recovery as the climate continues to shift and as fires continue to occur.

3.3. Methods

3.3.1. Study Area

Waterton Lakes National Park (WLNP) is in the southwestern corner of Alberta, Canada bordering British Columbia (BC) and Montana, USA (113° 54'46" W, 49° 2'55" N, Figure 3.1). This Park supports a wide variety of flora and fauna and supports some species which are endemic to the region. This is due to the wide range of ecozones, extending from prairie grasslands, deciduous forest, to alpine (Government of Alberta, 2005). WLNP tends to experience warm, dry summers, and colder, wet winters (Figure 3.2).

The Kenow Wildland Fire in September 2017 was sparked by a lightning strike on Kenow Mountain in BC, and quickly spread eastward into Akamina and Waterton Parks due to the high speed westerly winds and the persistent hot and dry conditions (Figure 3.2), referred to as 'fire weather' (Jain et al., 2024). Approximately 38% of WLNP was severely burned in the fire (Aspinall et al., 2025; Parks Canada, 2023b). The wildfire burned approximately 35 000 ha total between BC, Waterton, and the surrounding areas. Cameron Valley (CV) is the study area (Figure 3.1), and while most of the area is burned, two valleys, Lineham and Rowe, were both missed by the fire, and therefore are a comparison region demonstrating the old growth forest baseline. Additionally, some area near Cameron Lakes at the southern end of the valley is also unburned due to water bombing efforts to preserve new infrastructure.

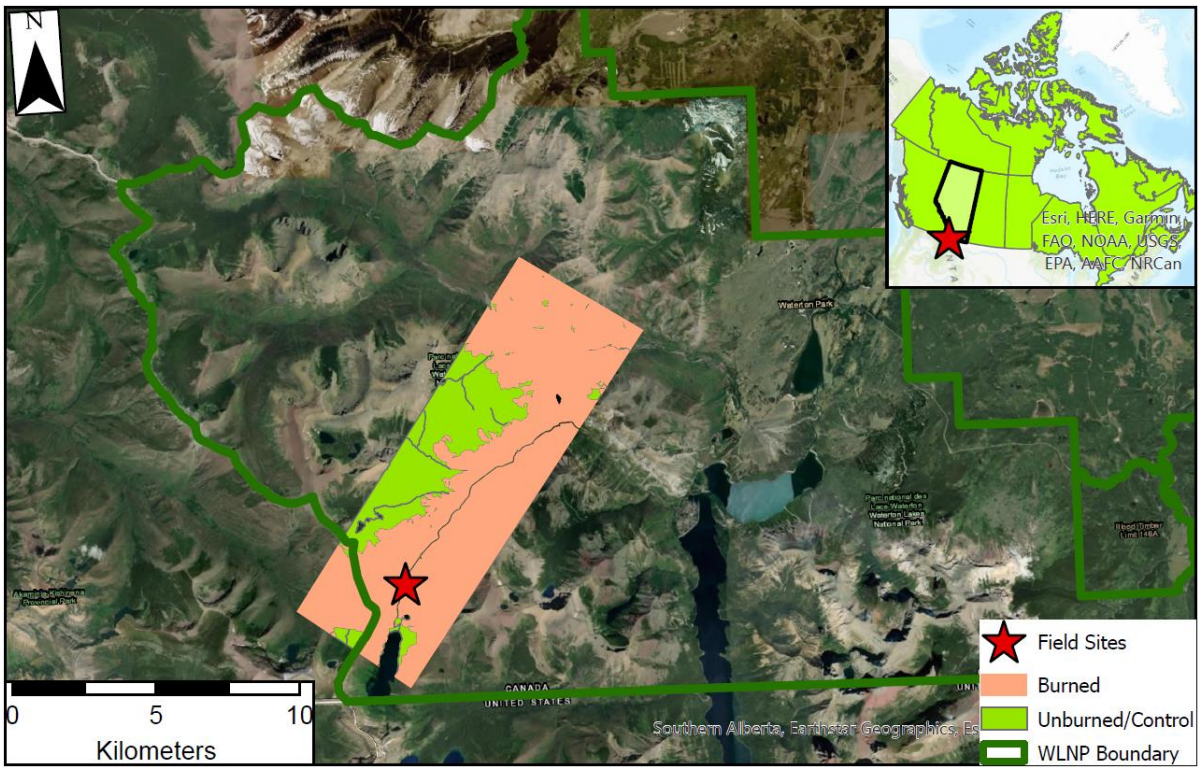

Figure 3.1: The study area of Cameron Valley in Waterton Lakes National Park, Alberta, showing the lidar polygon extent, delineated into burned and unburned regions.

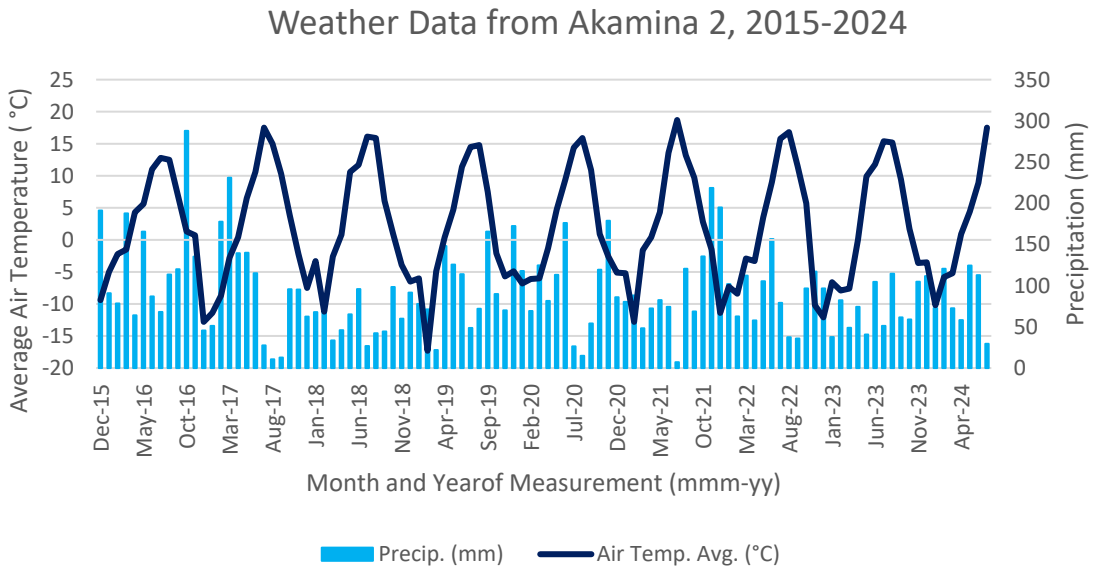

Figure 3.2: The average monthly air temperature and monthly precipitation from the Alberta Climate Information Service for the Akamina 2 station (replaced following the fire), from 2015 to 2024 (Government of Alberta, 2025).

3.3.2. Data Collection

Airborne lidar surveys were flown over Cameron Valley using the 'Titan' multi-spectral lidar system (Teledyne Optech, 2023) once every July from 2018 to 2024, for a total of seven surveys, to capture peak vegetation phenology. This lidar sensor is equipped with three laser wavelengths: 532nm (green), 1064 nm (Near-Infrared (NIR)), and 1550nm (Short-Wave Infrared (SWIR)). The lidar were validated with field height measurements and cover data derived from RGB photography, collected coincidently each year (Chapter 2.3).

3.3.3. Data Analysis

3.3.3.1. Data Pre-processing

The lidar data went through a quality control procedure to align trajectories, remove air points, below ground points, and other issues caused by the multi-pulse in the air (MPIA) effects such as that in the 2018 dataset, the survey closest to the fire. The lidar point clouds for each year were classified into ground and vegetation classes and gridded to develop 1 m and 5 m grid cell digital elevation models (DEMs) and digital surface models (DSMs). The vegetation class was gridded to a 1 m grid cell spatial resolution to determine vegetation height. All points in each channel were gridded by mean intensity to a 5 m grid to develop SWIR and NIR rasters for developing an index of vegetation cover.

3.3.3.2. Vegetation Models.

All vegetation layers and terrain drivers were derived from the lidar data. Vegetation cover data was modelled from the active normalized burn ratio (aNBR), using a ratio of SWIR and NIR, as demonstrated in equation 3.1 (Chasmer et al., 2017). The aNBR can be used for determining the severity of a burn (Chasmer et al., 2017), but it can also be used as an index of early post-fire vegetation recovery (Aspinall et al., 2025). A

correction factor of 0.9 was applied to the 2019 aNBR dataset, as that year experienced a 10% higher humidity level (Appendix B), which was correlated with a higher aNBR value than expected based other years of data and the stage of post-fire regeneration (Government of Alberta, 2025). This is likely due to attenuation in the SWIR channel, which is affected by water vapour content in the atmosphere (Mars & Rowan, 2010). All aNBR datasets were input into the conditional equation set described in equation 3.2 based on locally collected remotely piloted aircraft system imagery and field data (Chapter 2, Appendix A) to calculate the fractional cover (Fcov) datasets used in further analysis.

Equation 3.1. $$aNBR = (NIR - SWIR) / (NIR + SWIR)$$

Equation 3.2. $$\text{Where } aNBR \leq -0.65, Fcov = 0;$$
$$\text{Where } aNBR \geq -0.65, Fcov = 12.37(aNBR + 0.65)^{2.49}$$

Vegetation height was calculated by subtracting the DEM from the DSM at a 1m grid cell (Equation 3.3, Chapter 2.2.3.3 (St-Onge & Achaichia, 2001)). In the burned region, the dead standing stems were removed from the dataset by setting any pixel with a value greater than 3m to null, as these would falsely impact the true vegetation height growth rates in the area. Additionally, 3 m was the maximum height observed in the field for live post-fire vegetation within the study period (chapter 2). CHM values in the unburned area greater than 50 m were also removed from the dataset and set to null, as these are errors in the dataset either due to missed air points in the original classification of the point cloud, or cliff faces that were classified as trees. Additionally, there are very few tree species in WLNP that reach a height beyond 40 m, so this 50 m threshold avoids

the removal of true vegetation in the region. Despite the CHMs showing no significant difference in the time frame when measured across the valley without stratification (Chapter 2), the CHMs were tested for hypsometric change. The other drivers were not tested against vegetation height due to the lack of significant difference in vegetation height over the period of 2018-2024, or the first 7 years post-fire.

Equation 3.3. CHM = DSM-DEM

3.3.3.3. Terrain Drivers.

Elevation was taken directly from a lidar derived DEM with a 5 m grid cell spatial resolution. Directional aspect, slope, TPI, and TC were derived from the 1 m DEM, then aggregated to a 5 m grid cell to reduce the processing power needed and to align with the vegetation data layers and the elevation layer. The 2019 DEM was selected as the basis for the terrain drivers, because it was the earliest fully completed flight with minimal errors to the fire, meaning that this dataset is both complete and has minimal occlusion from vegetation, which may influence the values in later years. While a survey was collected in 2018, multiple-pulse-in-the-air (MPIA) issues occurred in the northern portion of the CV, and therefore the DEM was incomplete, making the 2019 survey the more reliable one. Additionally, due to the MPIA issue in 2018, the lowest elevation band (1300-1400 masl) is missing from this vegetation dataset, but as it was present in all other datasets, the elevation band was still included for analysis. All terrain drivers were aggregated to5m grid cell spatial resolution to preserve detail and to remove local influences including individual boulders and small rills, to increase the accuracy of the more generalized terrain models (Cartwright et al., 2020).

The DEM was stratified into 100 m elevational band classes based on the values and ranges represented in Table 3.1. The hypsometry of the study area is represented in Figure 3.3. Since less than 1% of the total area is accounted for in the top 3 bands (2500-2700 masl), and these areas are well above the 2300masl treeline and therefore support very little vegetation, so these regions were removed from analysis.

Table 3.1. Elevation stratification into 100m bands for terrain analysis, and the amount of area in each band.

Maximum Elevation of Band (masl)	**Area (km^2)**	**%Area**
1400	2.14	3.29
1500	4.02	6.17
1600	6.37	9.80
1700	10.11	15.54
1800	10.14	15.58
1900	8.40	12.90
2000	7.51	11.53
2100	6.01	9.23
2200	4.54	6.98
2300	3.30	5.07
2400	1.83	2.81
2500	0.51	0.78
2600	0.19	0.29
2700	0.04	0.06

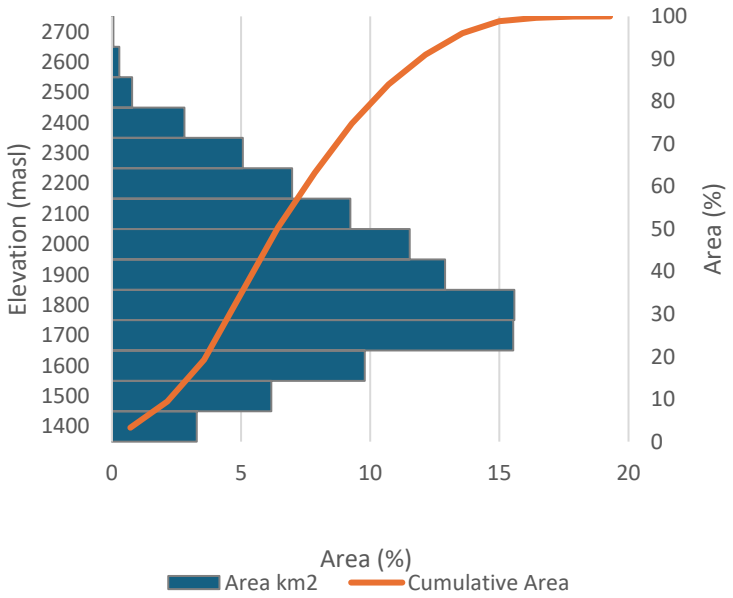

Figure 3.3. The hypsometry of Cameron Valley, by 100m elevational bands (based on the 2019 DEM).

Slope and aspect were developed from the 1m DEM using the respective tools available in ArcGIS Pro (Version 3.3.2). Slope was derived from the lidar DEMs for each year in ArcGIS Pro using the built-in slope function which uses equation 3.3 over a 3 x 3 window. The slope layer was then aggregated to 5m to align with the elevation and fractional cover. This was calculated for each grid cell in degrees (range from 0 to 90°). Slope was then stratified into nine equal interval classes, each covering 10° of slope angles Table 3.2. Since the top three classes (70°-90°) make up less than 1% of the total area, and the 50°-60° class contained just over 2% of the total area, the slopes from 50° to 90° were combined into one class for further analysis.

Equation 3.3: Slope = arctan(rise/run)

Table 3.2: The slope stratifications, based on equal interval, and the percent area in each class.

Class ID	Range (degrees)	% Area
1	0-10	16.11
2	10-20	18.79
3	20-30	26.00
4	30-40	29.67
5	40-50	6.36
6	50-60	2.10
7	60-70	0.78
8	70-80	0.18
9	80-90	0.00

Aspect was developed from the lidar derived DEMs for each year using the Aspect function in ArcGIS which also uses a 3x3 neighbourhood window. Aspect was aggregated to 5m to match the other layers of analysis. This was then reclassified into nine classes as presented in Table 3.3. Very few grid cells resulted in a flat (null) direction (<1%), and therefore these were removed from analysis.

Table 3.3: The aspect stratifications used in the terrain analysis, and the percent area in each class.

Class ID	Direction	Range (degrees)	% Area
1	North	337.5-22.5	13.00
2	Northeast	22.5-67.5	10.59
3	East	67.5-112.5	11.08
4	Southeast	112.5-157.5	15.47
5	South	157.5-202.5	17.30
6	Southwest	202.5-247.5	11.54
7	West	247.5-292.5	11.36
8	Northwest	292.5-337.5	13.66
9	Flat	-1	0.00

Topographic Position Index (TPI) is defined as the difference in elevation between a central pixel and the mean elevation of a window of surrounding pixels (QGIS Project, 2024). TPI was calculated in ArcGIS Pro using the LIDAR 1 m DEMs by calculating the mean of the elevation in a square window of seven grid cells, which was the maximum

available in this software for the terrain curvature calculations, and therefore this was selected for consistency. The mean elevation of the window was subtracted from the 'true' elevation of the grid cell at 1m as is demonstrated in Equation 3.4. Then the TPI was aggregated to match the 5m grid cell, therefore the total area considered in the TPI calculation was a 35 m x 35 m window, or the largest allowable in the software. The TPI was then reclassified into tree stratification classes; depressions, transitional, and uplands; based on a quantile approach Table 3.4.

Equation 3.4: TPI = (Elevation value of grid cell) – (mean elevation of the window)

Table 3.4: The stratifications of TPI and the percent area in each class.

Stratification	% Area
Depressions	19.06
Transitional	51.10
Uplands	29.82

Profile terrain curvature (TC) describes the concavity or convexity of the terrain relative to the surrounding area. This was calculated using the maximum allowable 7x7 grid cell window around the 1 m grid cell of interest to determine whether the cell was concave, convex, or transitional. This layer was then aggregated to 5 m and stratified using a quantile approach into three classes as described in Table 3.5.

Table 3.5: The stratifications of TC and the percent of the area classified in each class.

Stratification	% Area
Concave	38.76
Transitional	34.28
Convex	26.96

3.3.3.4. Statistics and Regression.

The Fcov and CHM were individually tested against terrain driver layers for each year in burned and unburned regions of the Cameron Valley. The Fcov and height

descriptive statistics were extracted over each stratification for elevation. Cover was tested against aspect, slope, TPI, and TC, and box plots, rose diagrams, or scatterplots were developed depending on the data driver to compare vegetation change between years and terrain drivers using the mean Fcov in the strata and the standard error.

Statistically significant differences between driver classes for each year were determined by using a Kruskal-Wallis (KW) test on each dataset to look for consistent patterns in the vegetation cover change as it is impacted by terrain over time. The KW test was used rather than ANOVA due to the non-parametric nature of the datasets. To determine minimum and maximum vegetation cover patterns over time by strata, the sums of ranks calculated for the KW test were compared. The terrain class with the highest rank sum was determined to have the most vegetation, and the class with the lowest rank sum was determined to have the least vegetation. In terrain drivers where there were only three classes, a KW test was run, and if a significant difference was detected with the KW test, the Mann-Whiteny test was run between every combination of classes to determine which classes were different.

To determine which combination of terrain drivers was most influential on a given year of fractional cover data, a generalized linear regression was completed using a sample of the dataset. Approximately 10% of the data in the burned area was extracted using random stratified sampling method by terrain class, with the sampling points distributed based on proportional area covered by each terrain class. Each year of fractional cover data was run through the algorithm in ArcGIS Pro spatial statistics, using the stratified drivers, to determine the correlations between the Fcov and each of the five drivers.

3.4. Results

3.4.1. Overview of Vegetation Growth Each Year

Airborne lidar data showed that vegetation is increasing over time since the fire between 2018 and 2024, based on the mean Fcov of the entire burn scar (Figure 3.4a). The height as represented by the mean CHM of the entire burn scar also increased (Figure 3.4b). The mean height vegetation of the unburned area across all surveys was 3.31m, which includes tall coniferous vegetation, shorter herbaceous vegetation, and non-vegetated areas. The means of the CHMs did not follow a linear growth pattern over the whole burn scar. The reduced heights from 2018 to 2020 are likely due to falling dead stems and branches as time passes since the fire, changing the height measurements detected from the lidar system. However, from 2021 to 2024 the mean CHM increases, suggesting that vegetation height is starting to increase more rapidly than dead vegetation is falling. Figure 3.5 shows the overall change in fractional cover across the whole study area for each year, spatially represented in a series of maps. The greatest vegetation growth appears to occur in regions close to water sources, including Cameron Creek which runs southwest to northeast in the valley, and in gullies and valleys between mountains.

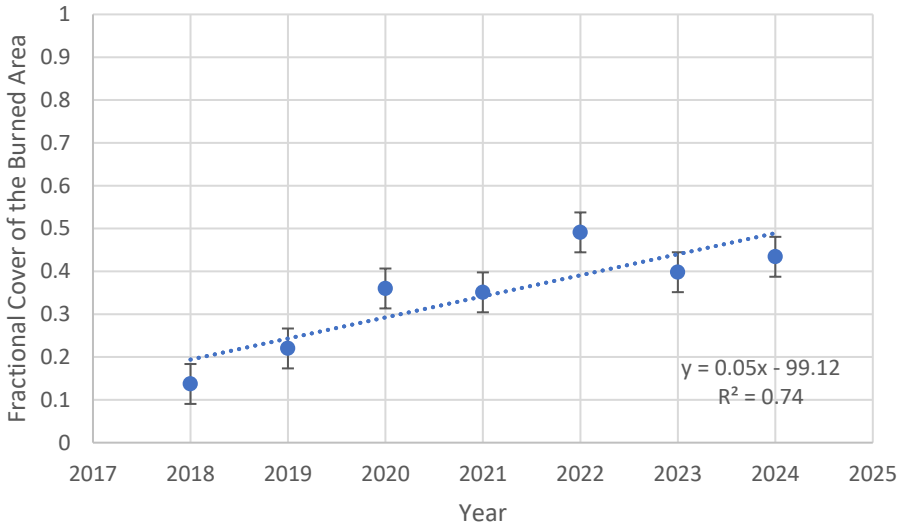

A)

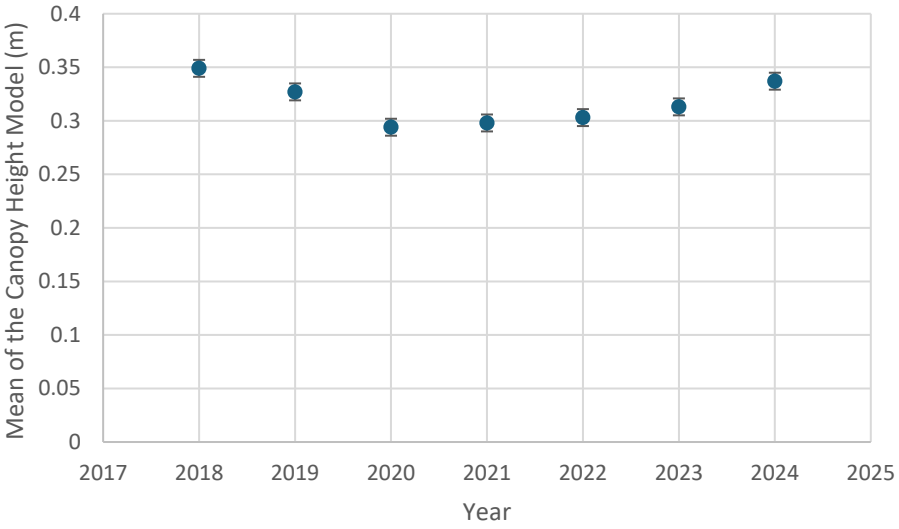

B)

Figure 3.4: The change in vegetation growth of the CV burn scar from 2018 to 2024, using the mean and standard error around the mean as calculated in Excel of the a) Fcov, and b) CHM.

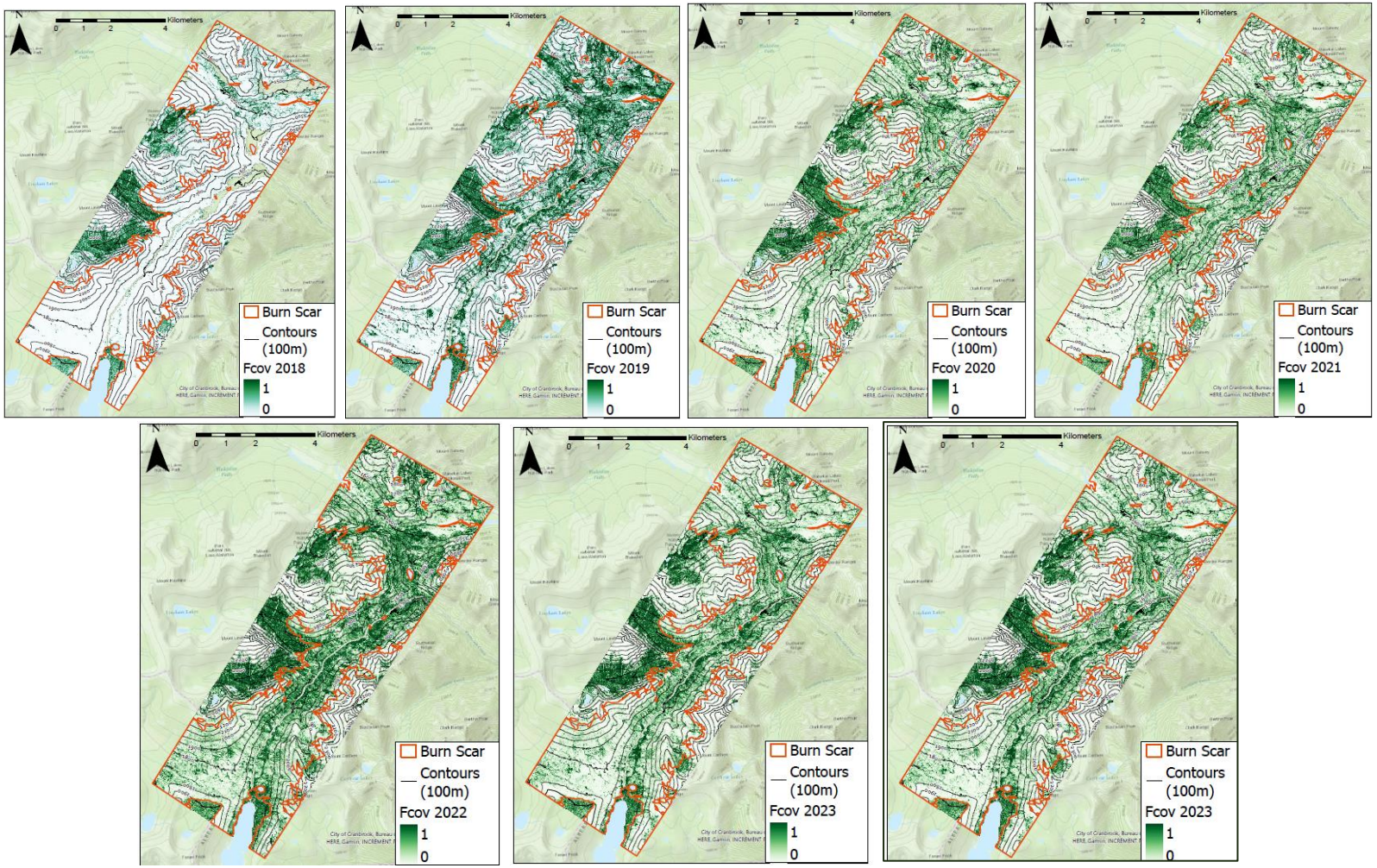

Figure 3.5: The spatial representation of changes in fractional cover for each year from 2018 to 2024, from the top left to the bottom right, across Cameron Valley.

3.4.2. Elevation

The mean and standard deviation of the fractional cover of each year in each elevation class is shown in Figure 3.6. The mean of all unburned years, which show similar results year to year, are also presented in Figure 3.6 as a comparison for the expected future regenerating vegetation behaviour. Vegetation cover varied significantly by elevation band in both the unburned and burned areas (KW <0.01). In the unburned areas, the maximum Fcov occurs between 1800-1900 masl, while in the burned areas the maximum occurs at 1600 masl. Figure 3.7 shows the hypsometric change in vegetation height. Both the burned and unburned areas also demonstrated a significant difference in vegetation height (KW, $p<0.01$). The height in the burned area peaked at 1600 masl, while the unburned area reached a maximum at 1800 masl. The height was variable in the burned area, as the maximum height occurred at 2500 masl, above the 2300 masl treeline. This indicates that the height measurements were also picking up boulders or other objects at higher elevations, or that the signal to noise ratio is too low in the early years of post-fire regeneration to accurately capture vegetation height (Chapter 2). Additionally, height at the higher elevation decreased over time, likely due to falling taller stems that remained initially following the fire but slowly started to fall as the stems started to decompose and lose structural integrity.

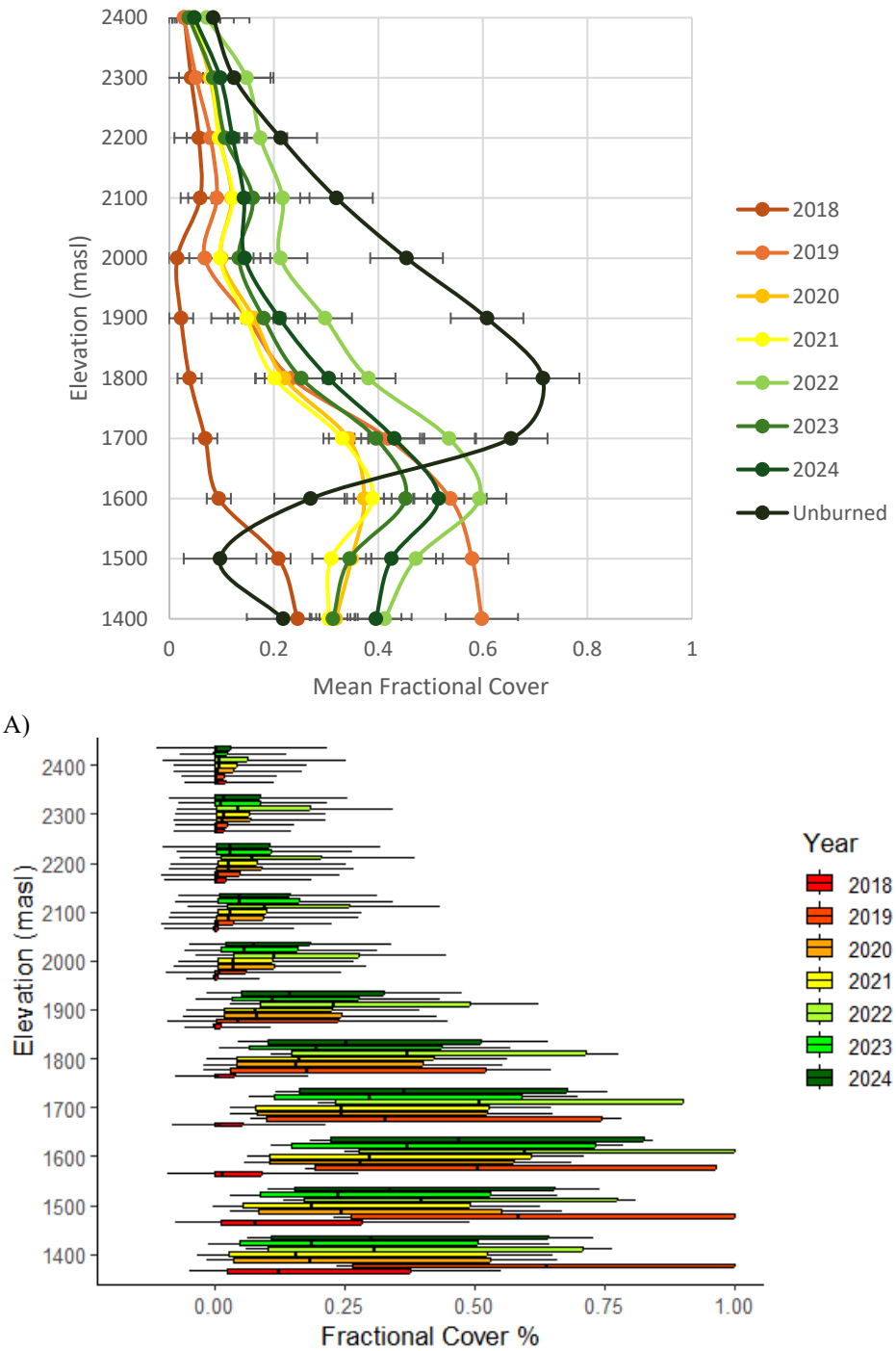

Figure 3.6: The fractional cover stratified by elevation in each year in the burned area represented by a) a scatterplot based on the mean and standard error, and b) a combined box plot based on the mean, interquartile range, and standard deviation (n=200,000).

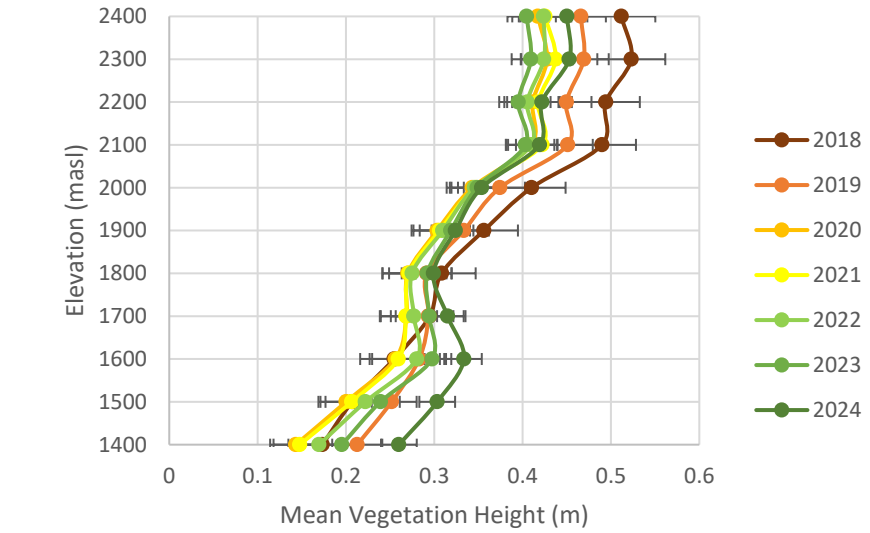

a)

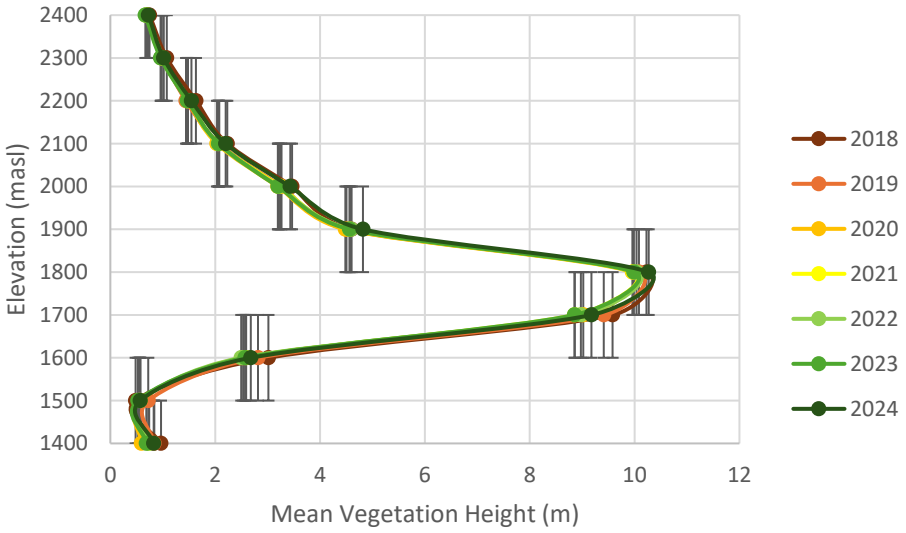

b)

Figure 3.7: The hypsometric distribution of the mean and standard deviation of the canopy height models for each year of a) the burned area and b) the unburned area.

3.4.3. Slope

Vegetation cover was highest in the shallowest slopes (0-10°) and lowest on the steepest slopes (50-90°) in both the burned and unburned regions (Figure 3.8). Both regions follow the same pattern of vegetation growth, with reduced vegetation in steeper slopes, which correspond to areas with little soil substrate and high elevations.

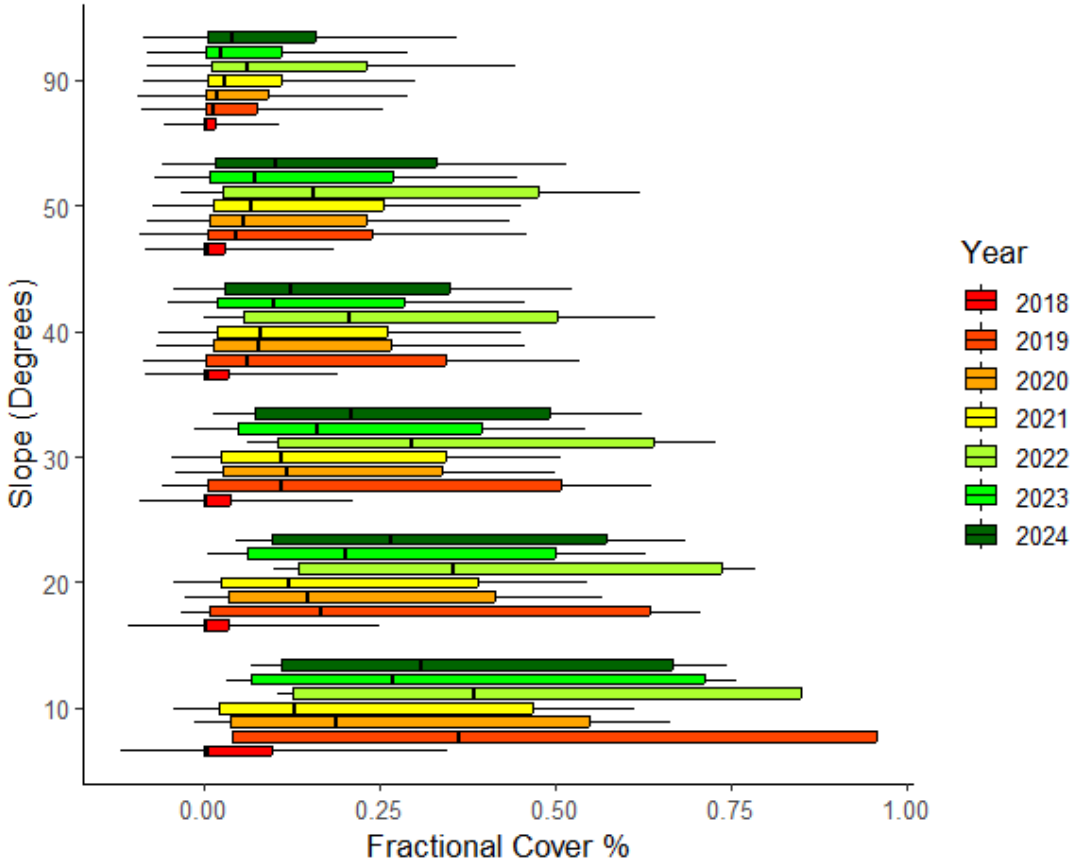

Figure 3.8: A box plot of the mean and standard error of fractional cover stratified by slope for each year in the burned area (n = 200,000)

3.4.4. Aspect

Aspect was influential on post-fire vegetation regeneration, with a general pattern showing increased fractional cover on north and east facing slopes, and lower levels of fractional cover on south and west facing slopes (Figure 3.9). Not all years follow this pattern, as in 2018, the greatest growth occurs in on the south facing slopes. The unburned area also shows a slightly different pattern, with the highest fractional cover on the west and northeast facing slopes. In the unburned area, the southwest facing slopes had significantly less vegetation, and the northeast facing slopes had significantly more vegetation than most other slopes, except for the west facing slope (KW, $p<0.05$).

Fractional Cover by Aspect in the Burned Area 2018

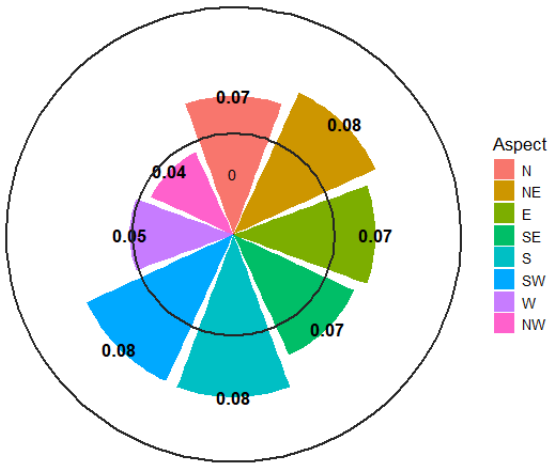

Fractional Cover by Aspect in the Burned Area 2019

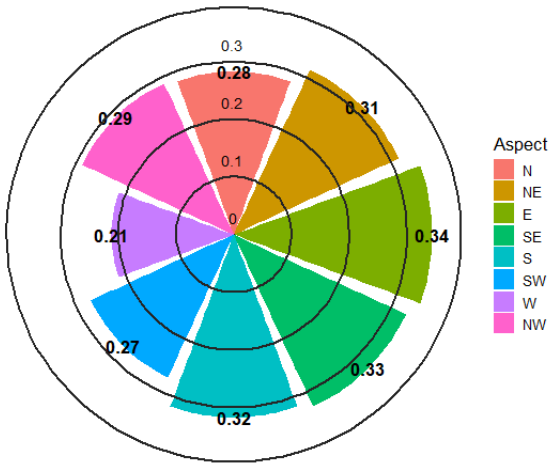

Fractional Cover by Aspect in the Burned Area 2020

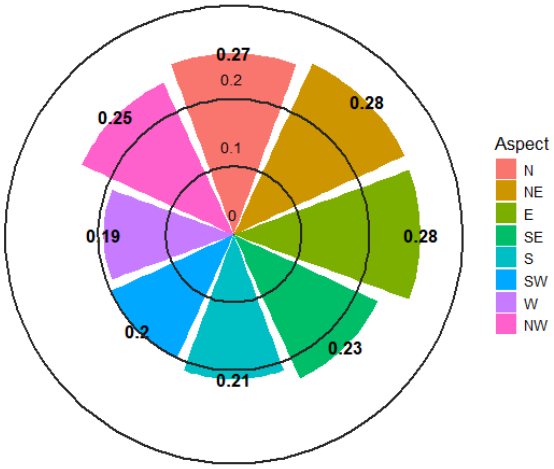

Fractional Cover by Aspect in the Burned Area 2021

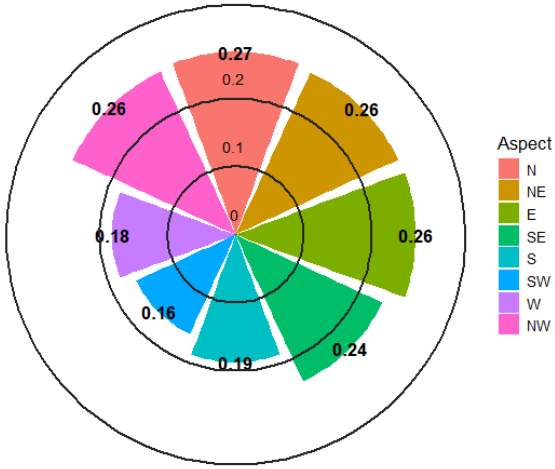

Fractional Cover by Aspect in the Burned Area 2022

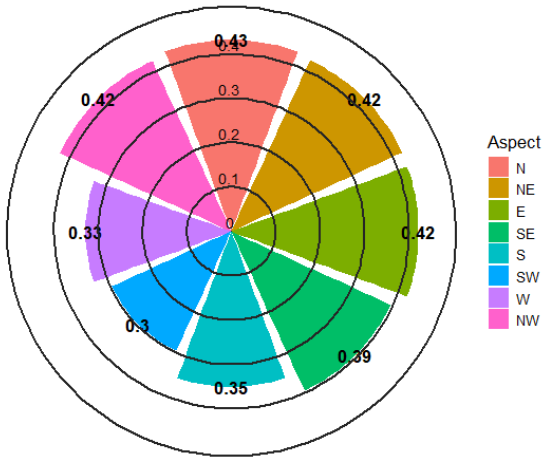

Fractional Cover by Aspect in the Burned Area 2023

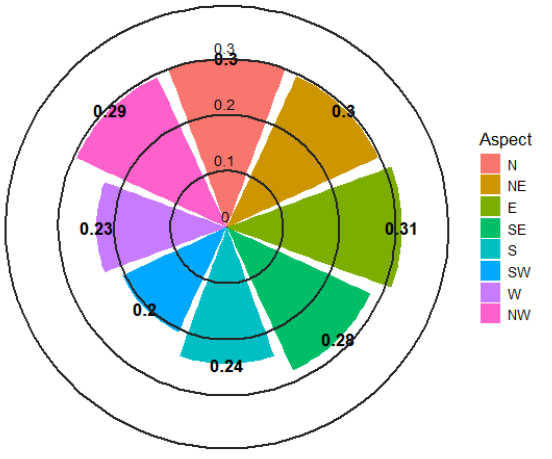

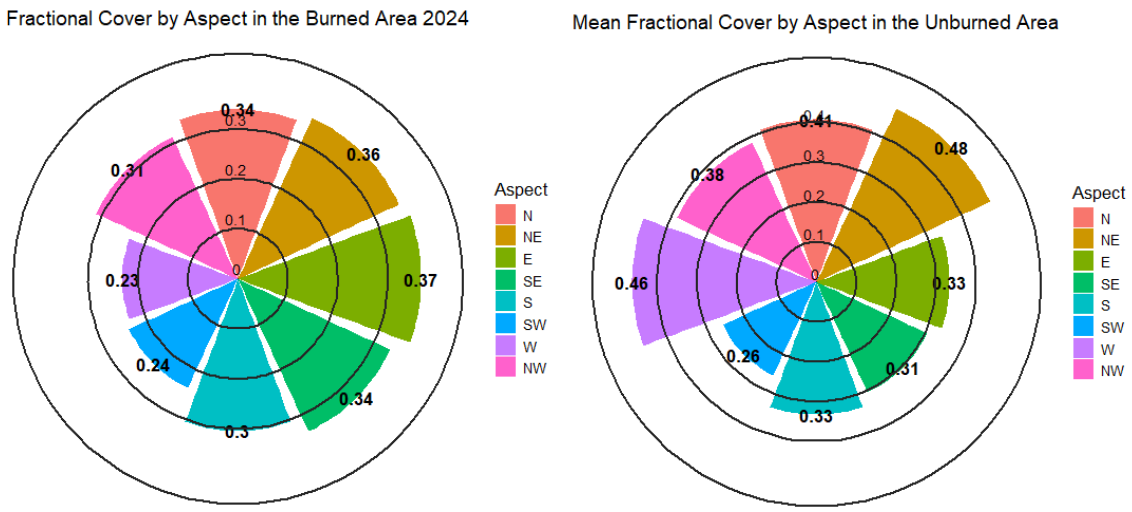

Figure 3.9: Rose diagrams of fractional cover in the burned area for each year, and in the mean unburned area of all years, stratified by aspect. The bolded numbers indicate the mean Fcov value of each aspect (on a scale of 0-1 for each section).

3.4.5. TPI

The vegetation cover in each of the three TPI classes is represented in a box pot in Figure 3.10. TPI was significantly different in both the burned and unburned sites (KW, $p<0.05$). The means and variance of each year in each zone are similar, however, the highest maximum Fcov values occur in upland areas in 2022.

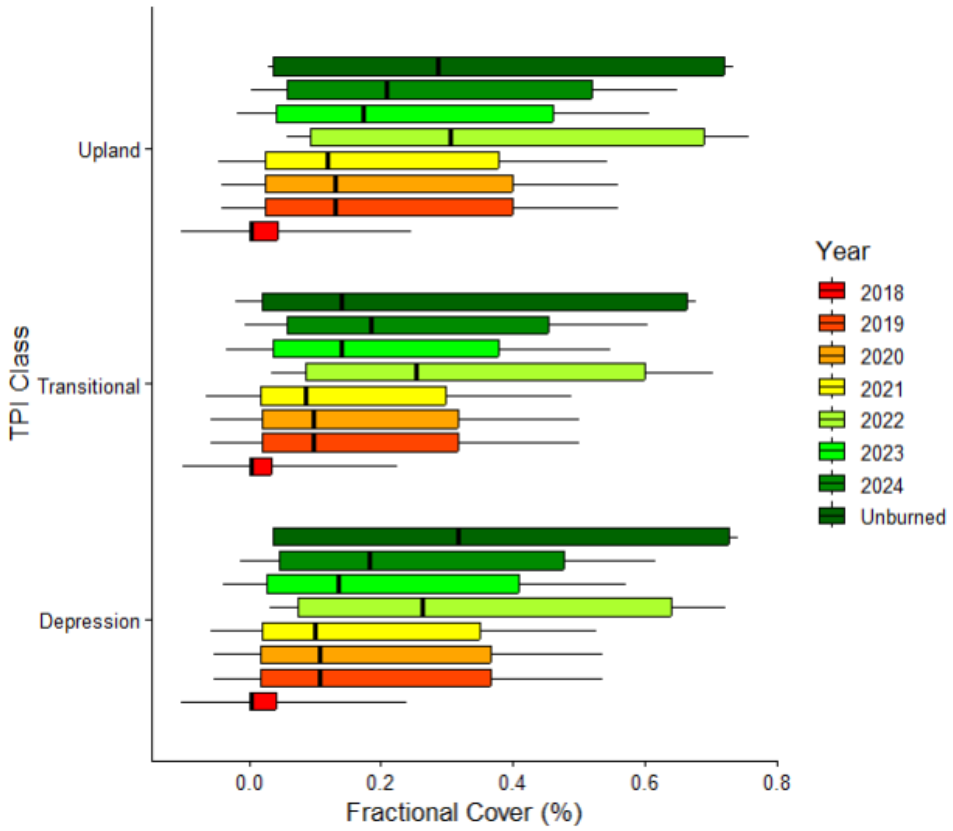

Figure 3.10: A box plot of the mean and standard error of fractional cover stratified by topographic position index, for each year in the burned area.

3.4.6. Terrain Curvature

The vegetation cover in each of the TC classes is represented as a box plot in Figure 3.11. TC was significantly different in both the unburned and burned sites (KW, $p<0.05$). In both the burned and unburned areas, the concave areas had significantly more vegetation cover than the flat and convex areas, and the flat area had significantly more vegetation cover than the convex area (MW tests, <0.05).

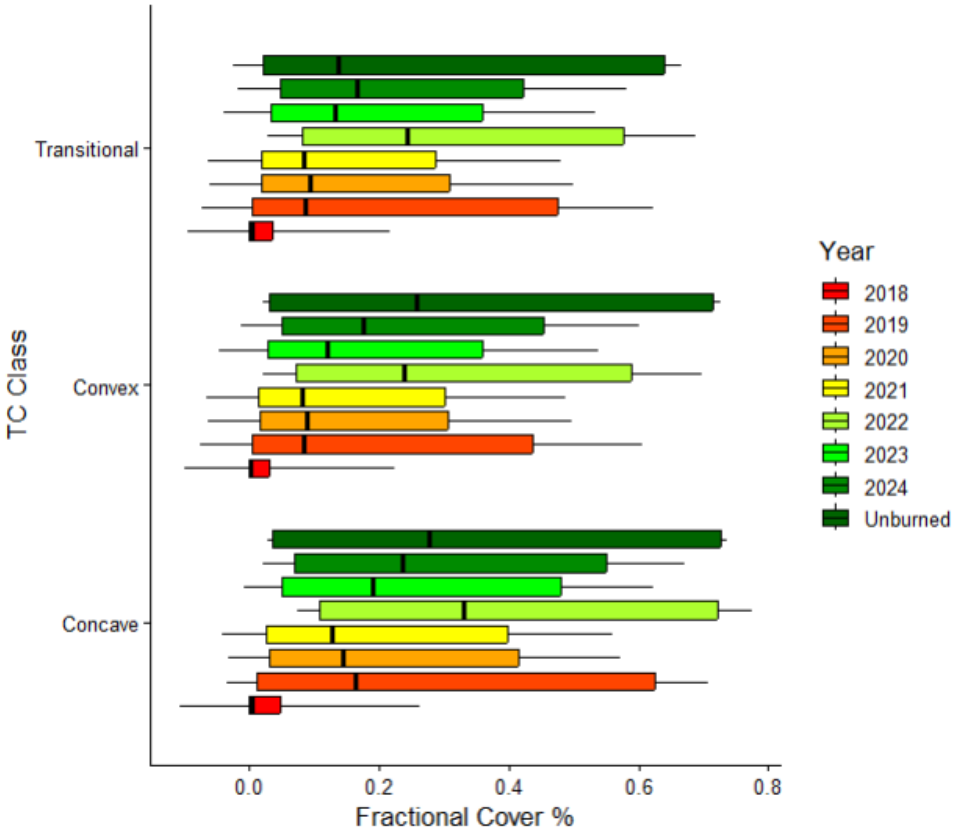

Figure 3.11: A box plot chart of the mean and standard error of fractional cover stratified by profile terrain curvature class, for each year in the burned area.

3.4.7. Regression Analysis Results

The results of generalized linear regression using continuous scales for all variables are presented for each year in Figure 3.12. Fcov is most correlated with elevation in each year, showing a decline in vegetation cover with increasing elevation. The second most correlated variable is slope, also demonstrating a negative correlation with increasing slope. TPI and TC are not significantly correlated with Fcov. Elevation and slope are related to each other, as are elevation and aspect. TPI is the only factor to demonstrate a positive trendline with Fcov, however, at a slope of 0.01, it is not a driving variable in multi-variate analysis.

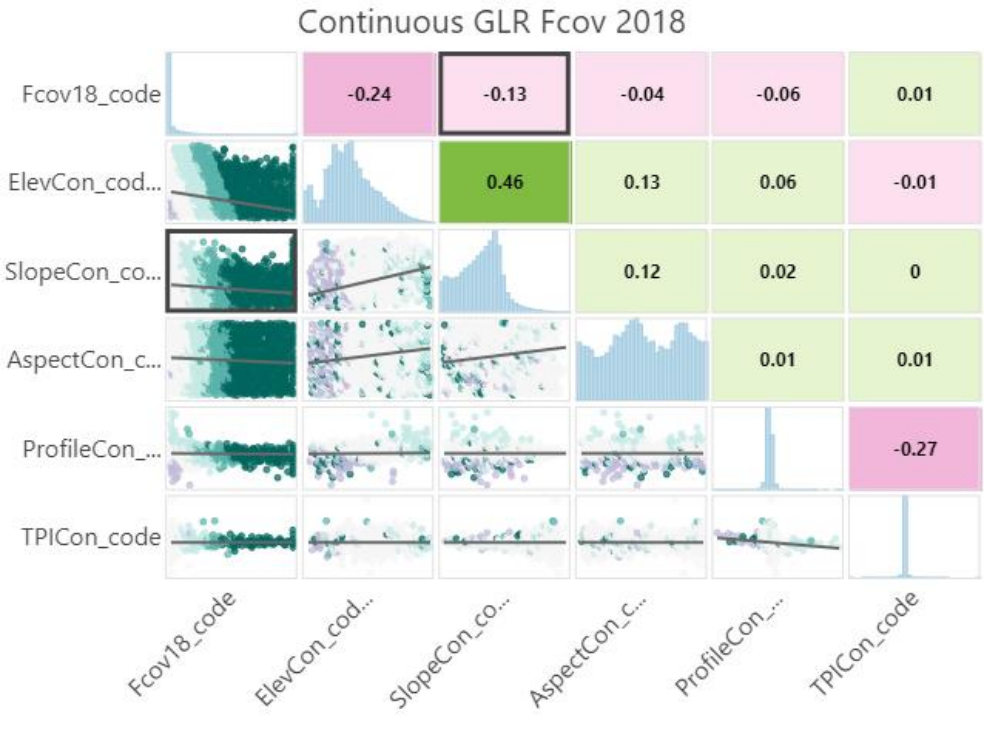
Continuous GLR Fcov 2018
Fcov18_code
ElevCon_cod...
SlopeCon_co...
AspectCon_c...
ProfileCon_...
TPICon_code
-0.24
-0.13
-0.04
-0.06
0.01
0.46
0.13
0.06
-0.01
0.12
0.02
0
0.01
0.01
-0.27

A)

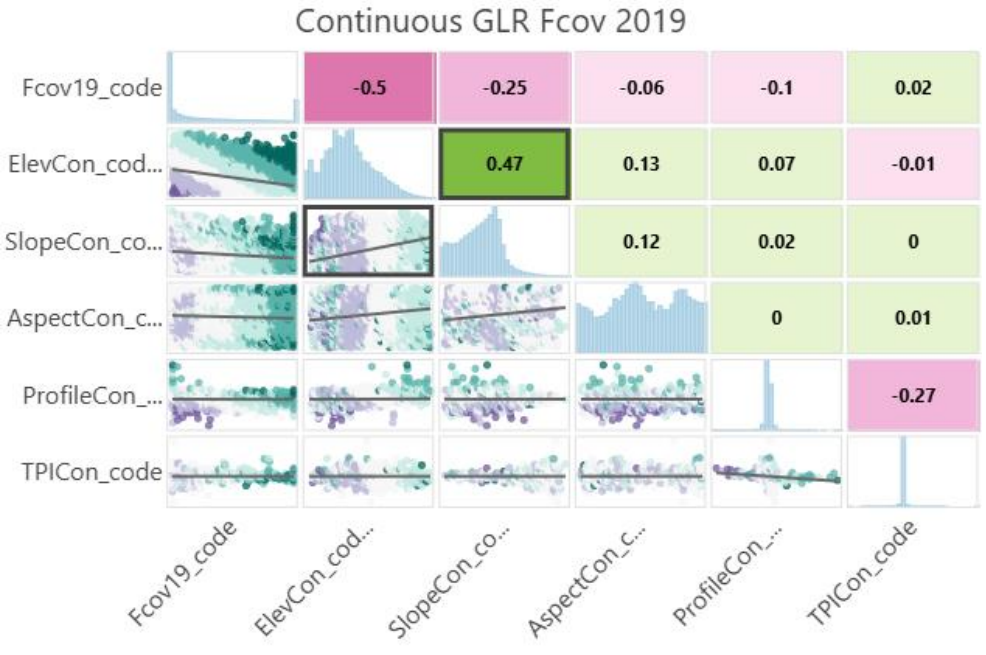
Continuous GLR Fcov 2019
Fcov19_code
ElevCon_cod...
SlopeCon_co...
AspectCon_c...
ProfileCon_...
TPICon_code
-0.5
-0.25
-0.06
-0.1
0.02
0.47
0.13
0.07
-0.01
0.12
0.02
0
0
0.01
-0.27

B)

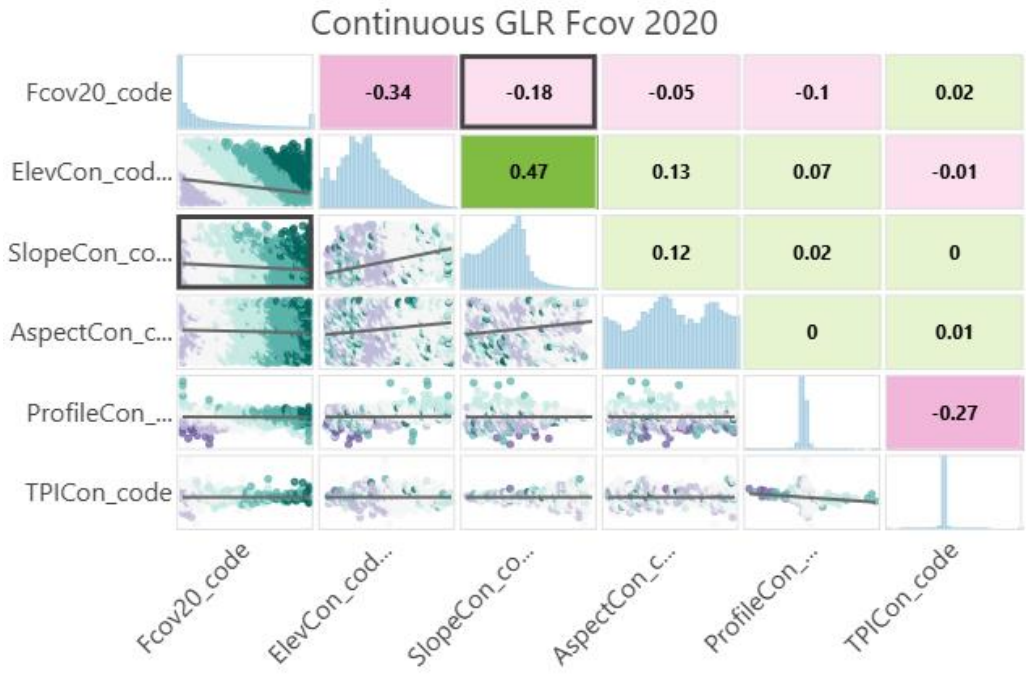
Continuous GLR Fcov 2020
Fcov20_code
ElevCon_cod...
SlopeCon_co...
AspectCon_c...
ProfileCon_...
TPICon_code
-0.34
-0.18
-0.05
-0.1
0.02
0.47
0.13
0.07
-0.01
0.12
0.02
0
0
0.01
-0.27

C)

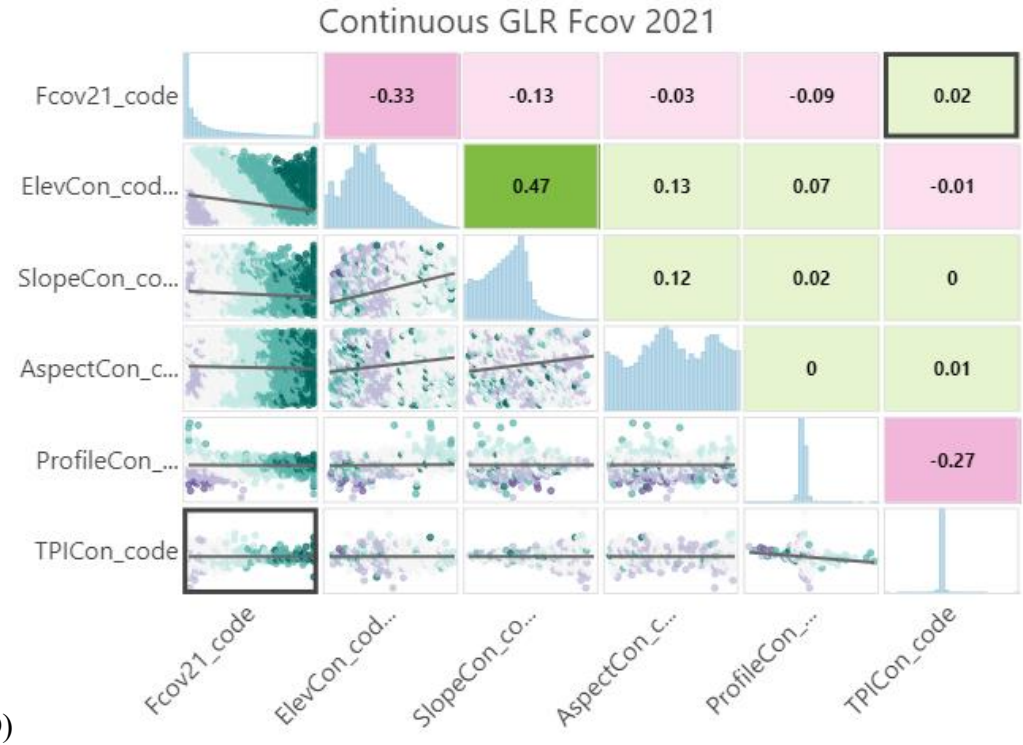
Continuous GLR Fcov 2021
Fcov21_code
ElevCon_cod...
SlopeCon_co...
AspectCon_c...
ProfileCon_...
TPICon_code
-0.33
-0.13
-0.03
-0.09
0.02
0.47
0.13
0.07
-0.01
0.12
0.02
0
0
0.01
-0.27

D)

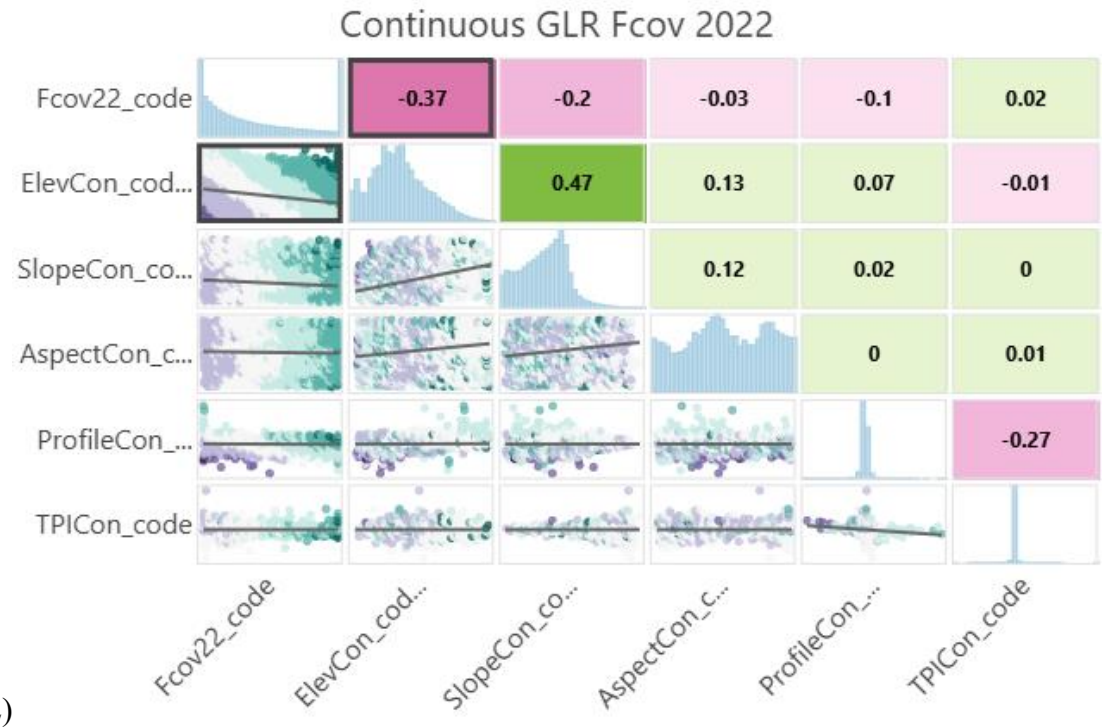
Continuous GLR Fcov 2022
Fcov22_code
ElevCon_cod...
SlopeCon_co...
AspectCon_c...
ProfileCon_...
TPICon_code
-0.37
-0.2
-0.03
-0.1
0.02
0.47
0.13
0.07
-0.01
0.12
0.02
0
0
0.01
-0.27

E)

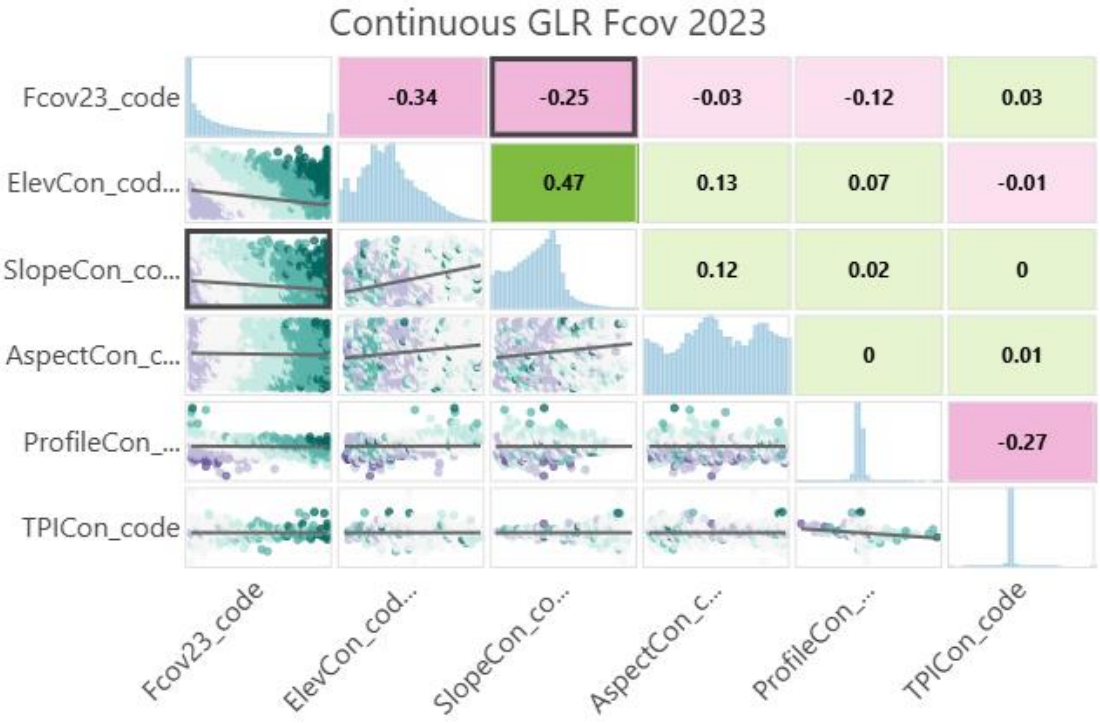
Continuous GLR Fcov 2023
Fcov23_code
ElevCon_cod...
SlopeCon_co...
AspectCon_c...
ProfileCon_...
TPICon_code
-0.34
-0.25
-0.03
-0.12
0.03
0.47
0.13
0.07
-0.01
0.12
0.02
0
0
0.01
-0.27

F)

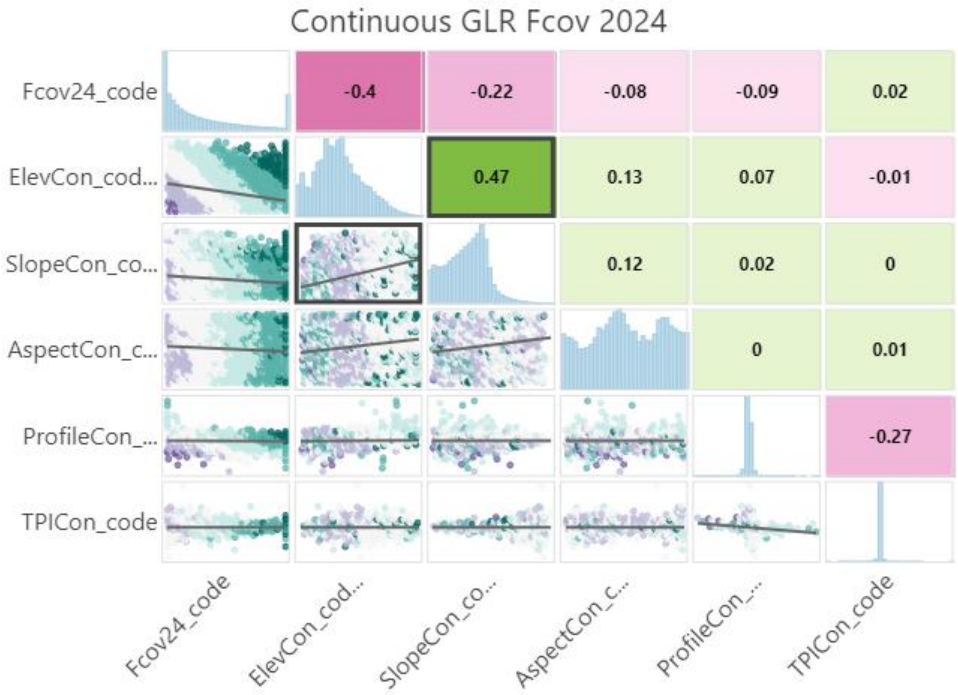

G)

Figure 3.12: The correlation matrices for fractional cover against all five terrain drivers for a) 2018, b) 2019, c) 2020, d) 2021, e) 2022, f) 2023, and g) 2024. Note that the axis names are based on the field names in ArcGIS Pro, and the first portion prefacing the Con_code is the variable of interest. Profile is referring to terrain curvature. Pearson's R is the name represented in either the green or pink squares, demonstrating a positive (green) or negative (pink) relationship between the two variables. In the scatterplots, the lighter colours represent a smaller residual value, and the darker colours represent a larger residual value (where purple is a negative standard deviation and green is a positive standard deviation).

3.5. Discussion

3.5.1. Differences between the Burned and Unburned Areas

The regions designated by the 'burned' and 'unburned' areas differ by vegetation cover, as well as in areas they cover. The burned area is a much larger area than the unburned area, therefore, more observations are obtained and used in the descriptive statistics for determining the relationship between Fcov and each driver. The unburned area is smaller, overall has a higher mean elevation at approximately 2030 masl, while the burned area has a mean elevation at approximately 1825 masl. The differences in mean elevation profiles may have influenced the results of the comparisons between the burned and the unburned sites. Additionally, the river valleys in the unburned area are primarily running west to east, and therefore the dominant slopes are north and south facing.

However, the overall Cameron Valley and Cameron Creek flows southwest to northeast, resulting in more of the slopes facing southeast and northwest, which could influence aspect comparisons between the two regions. While these two areas are sharing a boundary, the differences in local terrain within Cameron Valley in the burned and unburned areas could have influenced the comparisons between the two regions. Therefore, it is critical to understand local differences in a mountainous environment, even if both regions are in the same area.

3.5.2. Vegetation by Elevation

Vegetation as measured by fractional cover is significantly recovering across the entire study area in the study period. General trends in hypsometric vegetation growth demonstrate that the maximum vegetation cover occurs between 1800 and 1900 masl when the forest is undisturbed. In the burned sites, the greatest vegetation cover is occurring at 1600 masl. The uncertainty in the hypsometric vegetation cover tends to increase in the top elevation bands (2500-2700 masl) in both the unburned and burned areas, likely due to the small amount of area of the total hypsometry included in these bands, therefore each value is more influential on the total mean. Additionally, most of this area is barren rock, and therefore the Fcov values would be determined by factors such as dust cover and potential erosion, rather than vegetation (Gerrand et al., 2021). Vegetation height in the unburned area shows three local maximum bands, at 1600, 2100, and 2500 masl, while in the unburned area the vegetation height peaks at 1800 masl, in the same range as the cover. Treeline in CV occurs at approximately 2300 masl (Aspinall et al., 2025), so the height peak observed at 2500 masl is likely erroneous, or due to some other features in the landscape that could not be removed in the quality control analysis,

such as cliffs or large boulders. Mountainous vegetation growth has previously been linked to elevation in several studies, and typically vegetation growth is limited by temperature, as the air temperature decreases with elevation (Macias-Fauria & Johnson, 2013; McCaffrey, 2018; Zou et al., 2023).

3.5.3. Vegetation Cover by Slope and Aspect

Slope was a significant driver of vegetation growth, as most of the vegetation growth occurred in the 0-10° range, and very little vegetation was supported in the 60-90° range. Slope is a driver for soil depth and moisture, and steeper slopes tend to support less soil due to gravitational effects and the principle of the slope of repose (Littlefield, 2019; Thompson & Moore, 1996; Zou et al., 2023). Additionally, much of the area of high slope occurs near the high elevation ridgelines above treeline, so when high slope is combined with high elevation there is reduced vegetation cover. Slope is a driver of vegetation growth as it impacts soil availability and moisture levels, both of which are critical to plant life (Brockway, 1998; Thompson & Moore, 1996).

Aspect was a significant driver in the burn scar and in the old growth forest, as there was generally more vegetation cover on the northeast facing slopes than on the south facing slopes. Directional aspect is a critical driver related to solar energy balance (McCaffrey & Hopkinson, 2020). Since the south and southwest slopes receive more direct solar radiation, the soils tend to be drier due to increased evaporation rates and temperatures compared to shaded areas, like the northeast facing slopes (McCaffrey & Hopkinson, 2020). Therefore, plants that are less drought tolerant may not survive as well on south facing slopes in the long-term, causing the north facing slops to have more vegetation.

3.5.4. Vegetation Cover by Topographic Position and Curvature

TPI and TC are similar drivers, and both are related to microtopography, distance from water table, soil profiles, and they describe the variance in the surface (Aspinall et al., 2025; Cartwright, 2018; McCaffrey & Hopkinson, 2020). Both were significant drivers in both the burned and unburned areas. The unburned areas showed that the TPI transitional and upland areas supported the most vegetation growth, while the burned areas showed that the most vegetation growth occurred in the low-lying depressions. Uplands typically support less vegetation than low lying areas, however, it is possible with some species that prefer drier conditions, that they may grow in areas that are slightly further from the water table. These species could include fireweed and lodgepole pine, as these tend to be early species in post-fire succession regions, and therefore are tolerant of drier conditions (Aspinall et al., 2025; Chappell & Agee, 1996; Robinne et al., 2020). A possible cause for this difference could be species succession, as later succession conifers and perennials are adapted to the drier environments associated with upland areas (Letts et al., 2009).

However, the terrain profile curvature indicates that vegetation cover is higher in concave areas, which typically correspond with depressions in TPI. These areas can support, some early post-fire succession plants, such as grasses and annual flowers, which often do not have the root structure and traits to survive long in dry conditions and require closer access to the water table. Terrain curvature results showed that significantly more vegetation growth occurred in concavities across the entire study area. Concave areas also tend to be closer to the water table in the same way as depressions area in the TPI driver layer (Aspinall et al., 2025; Gerrand et al., 2021). Convexities tend to occur on ridgelines

and hardlines in the topography, and these usually have minimal soil or occur at high elevations, and therefore these compounding factors result in reduced vegetation growth.

3.5.5. Sources of Error and Limitations

The aNBR is a proxy for vegetation cover (chapter 2), however it is limited as cover saturates in the region after approximately 5-8 years of post-fire recovery, and therefore, Fcov as calculated from the aNBR is also limited by this time frame. Additionally, non-covered areas brighten over time as the soot from the fire reduces due to water or wind, so the aNBR is less effective for showing differences between covered and non-covered areas as time passes. The exact timing of saturation of Fcov over the region varies with the local terrain, as riparian areas tend to recover more quickly than upland areas. Therefore, further changes in saturated pixels cannot be detected using this index. Height measurements are recommended for use after Fcov saturates to continue to monitor stratified vegetation growth, once the height measurements are more reliable (Chapter 2). Additionally, since aNBR is originally designed to detect burn severity, or the 'blackness' of a surface immediately following a fire to determine ash levels, overtime the ash and soot of the fire is naturally removed from the environment, also increasing the aNBR (Aspinall et al., 2025; Chasmer et al., 2017; Gerrand et al., 2021). This is why it is possible to see a change in aNBR in otherwise barren rock, like in the high elevations beyond treeline, where the model may falsely predict Fcov. A change due to ash movement in the aNBR could result in overestimations of Fcov.

A limitation of this research is that the descriptive statistics were used to generate a comparison between drivers, and the means of the Fcov per driver layer were tested, rather than testing on the full datasets which were highly data and processing power

intensive. Therefore, as these statistics take the descriptive statistics of each class rather than testing all the points, some of the variance details may be missing from the total analysis. More advanced machine learning algorithms and computer processing hardware may be recommended for use in the future to process the amount of data in environmental monitoring of post-fire environments, as remote sensing data is highly data intensive and more area is catching on fire as the global temperatures rise and fire occurrence increases (Jain et al., 2024; Parks et al., 2025)

3.5.6. Future Research

Continued monitoring of the vegetation recovery by terrain driver is of interest for understanding post-fire succession in the Canadian Rockies under climate change conditions. Applying CHM information in the future is recommended once the height values are less variable and more accurate. The combined effects of multiple terrain drivers could be tested in the future, using some type of machine learning and multi-dimensional raster format. Further stratification or sub-stratification of the tested terrain drivers is recommended to further isolate the influences of individual drivers for improving ecosystem models. Additionally, since wildfire can have profound impacts on the environment, such as hydrological and geomorphological impacts, modeling the impacts of post-fire recovery on annual hydrographs and mapping erosional rates could further understanding of the dynamics of the post-fire ecosystem.

3.6. Conclusions

Vegetation is recovering across the entire region of the Cameron Valley in the observed period. Post-fire vegetation regeneration is related to a combination of elevation, aspect slope, terrain curvature, and topographic position index. Fractional cover is driven mostly by elevation, followed by slope and aspect. Vegetation tends to be

regenerating most quickly in lower elevation ranges, on shallow slopes, and on north and northeast facing aspects. Discrepancies in the microtopography results may indicate that different species or types of vegetation require different conditions, or that these layers require further refinement and analysis to predict fractional cover developed from lidar. The growth patterns are consistent over time, with dominant driver classes consistently supporting the highest Fcov values. Vegetation height is highly variable in the early post-fire recovery years, so it is not effective as a measure of regeneration at this point in the vegetation recovery trajectory. Continued vegetation cover and height monitoring is critical for understanding later developments in post-fire regeneration as the valley continues to recover in the future.

4. Chapter 4: Assessment of Snowpack Distribution and Depth Across a Post-Wildland Fire Mountain Environment Using Lidar: A Case Study in Waterton Lakes National Park, Canada

4.1. Abstract

Snowpack in the mountain headwater region of the Rocky Mountains is a critical water resource for Southern Alberta. Snowpack, vegetation, and local terrain drivers are highly interconnected, therefore stand-replacing fires, such as the 2017 Kenow Wildfire in Waterton Lakes National Park (WLNP), significantly impact snow depth and distribution. The objective of this research was to quantify changes in snowpack distribution in the early stages of post-fire recovery in WLNP relative to local terrain and vegetation drivers. Multi-spectral airborne lidar surveys were collected in the summer and winter to develop high resolution snow depth, terrain, and vegetation recovery models. Snowpack depth was related to five drivers: elevation, aspect, topographic position index (TPI), terrain curvature (TC), and vegetation cover, in the burned and unburned regions of the study area to determine shifts in annual snowpack distributions over time. Snowpack was significantly deeper in the burned areas than the unburned areas. The hypsometric snowpack patterns were significantly different between the burned and unburned areas in the earliest surveys; however, the maximum snow depth shifted from 1900 masl in 2018 to 2300 masl in 2025, demonstrating the recovery of snowpack distributions as the vegetation regenerates. Snowpack in all areas was significantly related to all other drivers, with maximum snowpack depths tending to occur on north-facing slopes in local concavities and minimum snowpacks on steep southwest-facing slopes. Quantifying changes in snowpack distribution with post-fire recovery is critical for predicting water resource estimates to inform water management decisions.

4.2. Introduction

Mountain headwater snowpack is critical for supporting the freshwater resource supply globally, especially in regions which rely on annual snowpack reserves to recharge surface water and groundwater resources. Quantifying snowpack depth and distribution is critical for supporting water resource estimates, which allow for informed water management decisions and policy, regarding water allocations for urban, agricultural, industrial, and recreational usage (Barnes, 2023; Broxton et al., 2019; McGrath et al., 2023; Van Gaalen et al., 2024). Increasing global temperatures and changing precipitation patterns are altering snow accumulation and distribution (Barnes, 2023; Giovando & Niemann, 2022; Lapp, 2002; MacDonald, 2008). Additionally, land disturbances such as wildfire alter snow accumulation and ablation patterns, as the lack of vegetation shading and decreased snow albedo result in early melt timing and in higher peak flows (Giovando & Niemann, 2022; Gleason et al., 2013; Guinn, 2023; Koshkin et al., 2022; Smoot & Gleason, 2021). Therefore, quantifying changes in snowpack accumulation distribution in a recovering post-fire environment is critical for predicting annual water resources for downstream regions supported by mountain snowpack headwaters.

Wildfires are occurring more commonly and more severely in North America in the past few decades due to a combination of fire suppression practices and climate change. In southern Alberta, fire suppression practices have been applied for about a century (Baron et al., 2022; Eisenberg et al., 2019), resulting in excessive fuel loading in some regions. Climate change is increasing the occurrence of “fire weather”, which is a combination of hot and dry weather for an extended period over a region (Jain et al., 2024). When a fire starts under these conditions, it can remove the canopy, understory,

and organic soils (Aspinall et al., 2025; Gerrand et al., 2021). This type of fire disturbance can remove the treeline from the region and therefore the snowpack is impacted. One such fire occurred in 2017 in Waterton Lakes National Park (WLNP), Canada. The fire started in British Columbia on Kenow Mountain from a lightning strike and quickly spread over the continental divide into Alberta, severely burned approximately 38% of the national park (Parks Canada, 2023b). Prior to the 2017 Kenow Wildfire, the last known wildfire in the region was about a century before (Aspinall et al., 2025), therefore an abundance of fire fuels was available, increasing the intensity of the fire. This stand replacing fire has had significant impacts on the vegetation regime in the region, and likely significantly impacted the snow resources, and therefore the water resources, of this critical headwater region for the Oldman River basin of Southern Alberta.

Snowpack is highly interconnected with vegetation cover, as high vegetation cover increases interception which increases sublimation rates, decreasing snowpack depth and density beneath the canopy (Pomeroy, *et al.,* 1998). Snowpack tends to be deeper in open areas, with earlier melt out dates, impacting hydrological systems (Smoot and Gleason, 2021). Old growth forests in the mountains tend to trap snow, preventing significant wind redistribution (Cartwright et al., 2020; Pomeroy & Gray, 1995; Pomeroy, Parviainen, et al., 1998). Typical mountain snowpack hypsometry shows that the maximum snowpack depth occurs in the alpine treeline ecozone, due to a combination of increased orographic precipitation and reduced wind redistribution, which ‘traps’ the snowpack within a few hundred meters of the treeline (Cartwright, 2018). The removal of the canopy significantly alters snowpack accumulation and ablation patterns and rates, and the location of maximum snowpack distribution (Smoot and Gleason, 2021).

Snowpack is influenced by forest fire, as soot and blackened stems decrease the local albedo, increasing melt (Gersh et al., 2022; Rother et al., 2022). Increased open area reduced interception and sublimation, causing deeper snowpacks that are also exposed to more direct solar radiation (Grunewald et al., 2013; Maxwell & Clair, 2019). Reduced vegetation cover allows increased wind redistribution of snowpack (Burles & Boon, 2011; MacDonald et al., 2018). However, the extent to which snowpack depth and distribution are influenced by wildfire, and then by the early post-fire vegetation regeneration has not been quantified.

The location of snowpack relative to the terrain can influence peak ablation rates and maximum hydrological peak flows downstream, therefore understanding how wildfire changes snowpack distribution in mountain headwaters is critical in flood and water resource management decisions (Smoot and Gleason, 2021). Snowpack hypsometry in the southern Canadian Rocky Mountains is impacted by various terrain drivers, including elevation, aspect, topographic position, and canopy cover (Barnes & Hopkinson, 2022a; Burles & Boon, 2011; Cartwright, 2018; Davis, 2012; Grünewald et al., 2010). However, it is not clear how the snowpack distribution changes when the treeline is removed, but it is expected that the maximum snowpack depth shifts downslope and decreases in elevation due to wind redistribution and gravitational effect. Quantifying the changing snow hypsometry is critical for informing hydrological models that rely on snowpack information, including maximum depth values and the location of the snowpack. Work done in nearby West Castle Watershed (Cartwright, 2018, Barnes and Hopkinson, 2022) demonstrated that it is expected that directional aspect and topographic position index will have a significant influence on snowpack distribution in WLNP.

Snow is usually measured in the field using a variety of methods including snow pillows, precipitation gauges, and snow course surveys (Pomeroy & Gray, 1995). These methods provide point information, which while this is informative data, it is not spatially distributed, and interpolating from these points over a large area could give overestimates or underestimates of snowpack resources (Barnes & Hopkinson, 2022a; Hopkinson et al., 2024; Hopkinson, Sitar, et al., 2004; Pomeroy & Gray, 1995; Pomeroy, Gray, et al., 1998). Therefore, to improve the spatial continuity of snowpack measurements, airborne lidar can be utilized. A lidar sensor emits pulses of specific light wavelengths and records the return pulse from the target, including the distance and the intensity of the reflecting pulse (Baltsavias, 1999; Deems et al., 2005; Deems et al., 2013; Hopkinson, Sitar, et al., 2004). This gives a three-dimensional point cloud. When the lidar survey is conducted over the same area, once in the summer (snow-off season) and once in the winter (snow-on season), the snow depth at each point can be determined for the day of the survey (Barnes & Hopkinson, 2022a; Hopkinson, Sitar, et al., 2004). Lidar is known to be an effective method for mapping snowpack depth over mountain watersheds (Hopkinson, et al.*.,* 2004; Deems, et al.*,* 2013).

Having a spatially distributed estimate of snowpack is useful for determining snow melt and water resources in the mountains (Barnes, 2023; Hopkinson et al., 2024). Snowpack hypsometry is critical in runoff timing and ablation, and therefore quantifying the depth and distribution of snowpack in post-fire environments is important, considering the increase in wildfire occurrence. Additionally, determining how snowpack changes over time with regards to vegetation regeneration is important for tracking the

trajectory of hydrological system recovery and ultimately for decision makers regarding water policy.

The goal of this paper was to quantify shifts in post-fire snowpack distribution patterns related to terrain drivers and early post-fire vegetation regeneration in the Cameron Valley (CV) of Waterton Lakes National Park (WLNP) using airborne lidar data. Snowpack depths were compared in the burned and unburned areas. Within each area, the snowpack was compared to the local terrain drivers, including elevation, aspect, topographic position index, and terrain curvature, to determine whether snowpack depth was significantly influenced by any of these drivers. Additionally, the snowpack depth was compared and the annual post-fire vegetation cover to determine if the distribution of snowpack is significantly different in the burned areas from the unburned areas, or if snowpack depth changes as the burned area regenerates. Quantifying snowpack depths and distributions in the post-fire environment is critical in understanding ecosystem dynamics as the systems continue to shift in the future.

4.3. Methods

4.3.1. Study Area

The study area is Cameron Valley in Waterton Lakes National Park (WLNP; 113° 54’ 46’’W, 49° 2’,54’’N), which is in the southwestern Alberta, bordering British Columbia and Montana (Figure 4.1). This is an important region of the WLNP which supports many lakes and streams, vegetation species, and wildlife, from an elevation range of 1346 meters above sea level (masl) to 2657 masl. The Kenow Wildfire burned approximately 38% of WLNP at high severity in September 2017, including much of CV (Parks Canada, 2023b). Cameron Valley was severely burned, except for two valleys,

Lineham and Rowe located on the west side of CV, and some area near the new infrastructure by Cameron Lake due to water bombing efforts. These unburned regions represent the old growth unaltered forest and are used as the ‘unburned’ study site.

A) 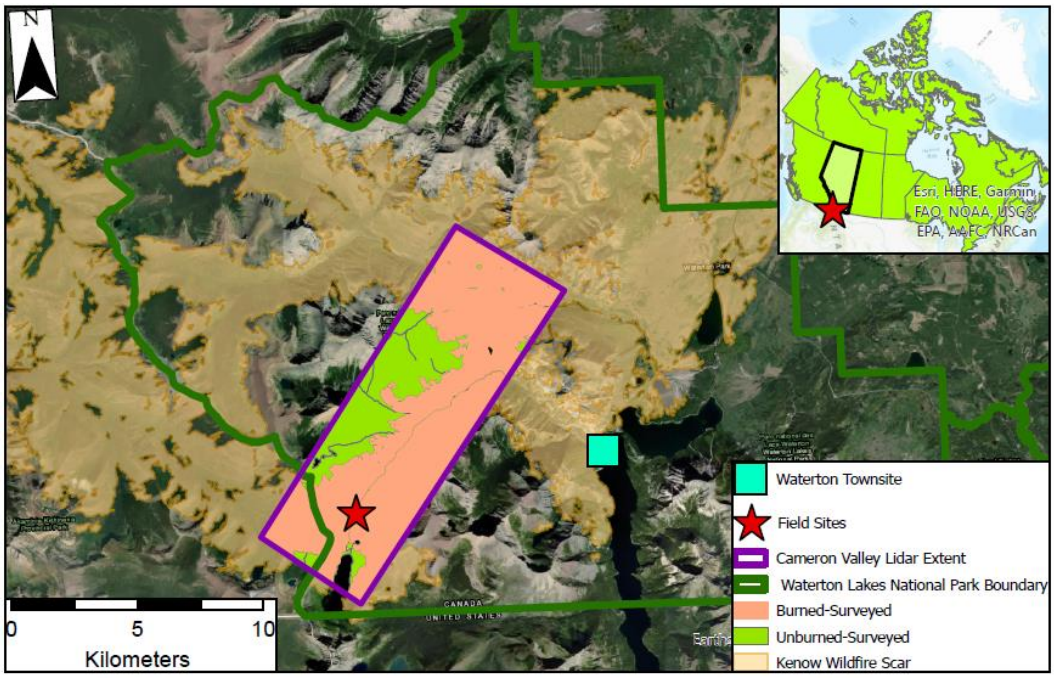

B)

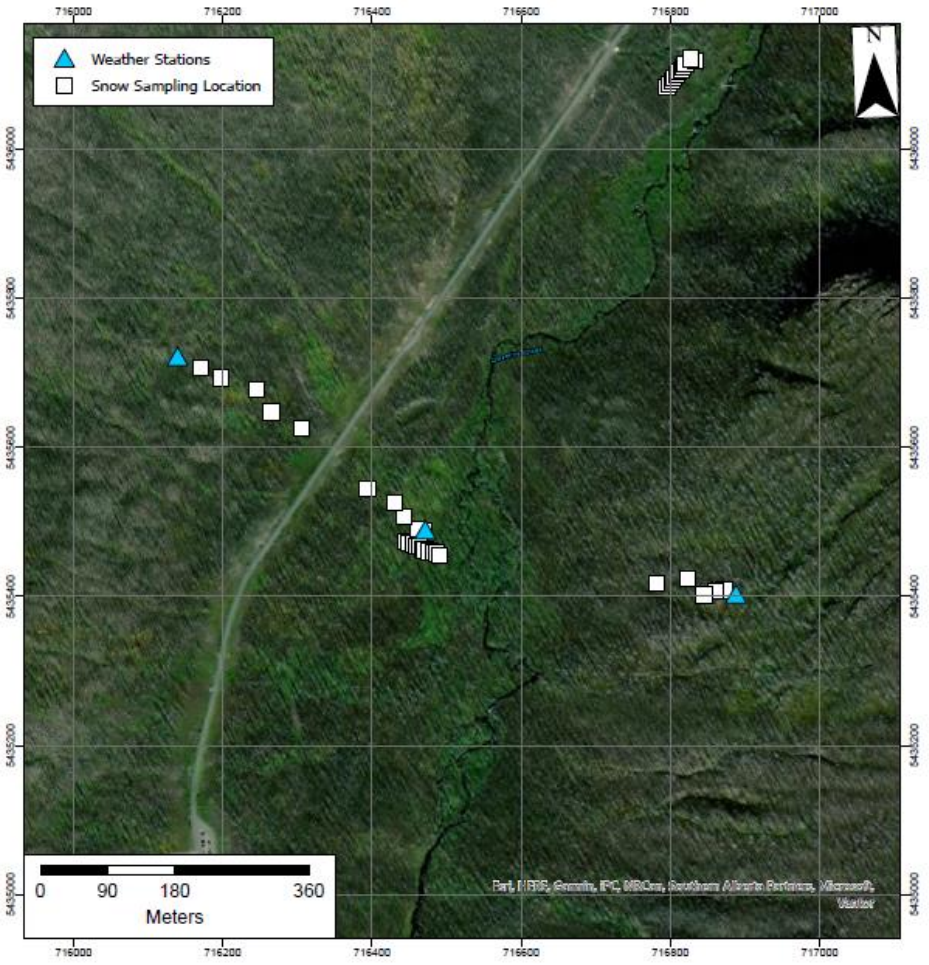

Figure 4.1: The study area, showing the a) airborne lidar extent in Cameron Valley, the general field site location, the burn scar extent, and the unburned area used as the comparison region, and b) the snow sampling locations in the field and the weather station locations.

4.3.2. Field Data Collection

To validate the lidar snow depth models (LSDMs), field measurements of snow depth were collected coincident with the airborne lidar survey (Table 4.1, Figure 4.1). Snow depth was measured following the approach in Hopkinson, et al., (2012), by using an avalanche probe every 5 m along a transect, and a star-shaped systematic sampling approach was taken, with a measurement taken at the point, 1 m to the left and right of the point, and 1 m ahead and behind the point. The mean of each of these samples was calculated and compared to the associated lidar snow depth model grid cell. Field surveys

were located either using transects and precise point positioning with a GNSS receiver system (2024), or using a handheld GPS receiver (2021, 2025).

Table 4.1: A list of the snow course surveys, locations, and dates.

Date	Location	Number of Depth Measurements
21-Feb-21	Cameron	15
21-Apr-21	Cameron	80
01-Apr-24	EC Site and Little Prairie	22
05-Apr-25	EC Site and Slopes	15

4.3.3. Airborne Lidar Data Collection

Airborne lidar data were collected for CV for every summer since the 2017 fire in July, and in seven of nine winters since the fire between January and April (Table 4.2). Five of the flights were collected using the multispectral Teledyne Optech "Titan" system (Teledyne Optech, 2023), which has three laser wavelengths: green at 532 nm, near infrared (NIR) at 1064 nm, and shortwave infrared (SWIR) at 1550 nm. The remaining three flights were collected using a dual channel "Riegl' system (RIEGL, 2021). Flight dates depended on weather conditions, aircraft and personal availability, and other logistical constraints. Flights were separated into two groups, the snow accumulation stage and snow ablation stage for comparison. Flights occurring between January 1 and March 15 were placed into the snow accumulation-dominated stage, and flights March 16 to April 30th were placed into the snow ablation-dominated stage.

Table 4.2: A list of the winter airborne lidar surveys, including collection date and lidar system used.

Year	Date	System
2018	Feb 10	Riegl
2020	Feb 2	Titan
2020	Mar 5	Titan
2021	Jan 22	Riegl
2021	Apr 6	Titan
2023	Mar 16	Riegl
2024	Apr 1	Titan
2025	Apr 5	Titan

4.3.4. Data Analysis

4.3.4.1. Lidar Data Processing and Snow Model Development.

Airborne lidar data was processed to align trajectories, then cleaned for air points, blowing snow, and multipath issues in Terrascan (Terrasolid, 2025). Datums and projections were corrected to ensure that everything was in WGS84 UTM 11 and were checked in Quick Terrain Modeller (Applied Imagery, 2025) to ensure that there were no significant vertical or horizontal offsets with the reference summer lidar point cloud. The data were then tiled and gridded to local max at 1m and 0.5m grid cell rasters in LasTools (rapidLasso, 2024). Similar methods were applied to the summer lidar datasets (Chapter 2.3). To develop the lidar snow depth models (LSDMs), the summer DEM was subtracted from the winter DEM, leaving the snow surface (Equation 4.1 (Hopkinson, Sitar, et al., 2004)).

Equation 4.1: LSDM = SnowDEM -SummerDEM

Once the LSDMs were developed, a quality control procedure was developed and applied to the models. The roads, buildings, lakes, and rivers were masked from analysis. Negative values in the LSDM were set to null if they were less than -0.10m and set to zero if they were greater than or equal to -0.10m. This is because vegetation can cause errors in the snow model, so this attempts to account for snowpack that is influenced by

dead vegetation near the ground, while removing errors caused by multipath or other errors that may have been missed in the cleaning process. Additionally, similarly to the quality control process adopted in Cartwright, et al., (2020), values higher than the 99th percentile were removed from analysis, to address false positive estimates from cornices and overhangs and to remove any missed air points.

The LSDMs for 2024 and 2025 were validated with the snow depth measurements from the snow course surveys, as these surveys had same-day time-coincident field surveys. The 1 m LSDMs were then aggregated to 5m grids for further analysis, both to reduce the data quantity and increase processing speed, and to remove microtopographic effects that may bias results while being significant at the watershed scale. The absolute snow depths were compared for each year, as these values are critical in water resource estimations, and the general patterns of snow distribution are comparable despite annual meteorological conditions changing. The distribution patterns are the result of interest when comparing drivers and shifts in snowpack depths across the valley as the region recovers after the fire. To compare hypsometric shifts in snowpack over time, the volume of snow each year was calculated using the sum of all of the snow depths in the burned area, then the percentage of the total snow volume in each elevation band was determined and spatially represented.

4.3.4.2. Drivers of Snowpack Distribution

Once the LSDMs were checked for quality and normalized, the mean snow depth from each of the burned and unburned areas from each survey was collected to find whether the burned or unburned areas consistently have a significant difference in the

amount of snow distribution. This is critical in determining the influence that wildfires have on general snow distribution and depth patterns and therefore water resources.

Snowpack varies significantly with various terrain drivers, including elevation, aspect, topographic position index (TPI), terrain curvature (TC) and canopy cover (Barnes, 2023; Cartwright, 2018). Therefore, each of these drivers were developed as rasters across the airborne lidar survey region (See chapter 3.3) and tested individually against snowpack year to year. All terrain driver rasters were developed from the snow-off surveys of their corresponding snow-on year and were grided to 5m grid cells, and therefore each pixel covers an area of 25 m^2.

Elevation was stratified in 100 m bands, for a total of 14 classes, and then was split into the burned and unburned areas (Figure 4.2) Once the elevation stratifications were determined, it was found that less than one percent of the area was contained in the top three elevation classes, from 2400 to <2700, and as these regions also had high noise, they were removed from analysis. Aspect was stratified into eight classes: north, northeast, east, southeast, south, southwest, west, northwest. TPI was developed using equation 4.2 using a neighbourhood window of seven grid cells, the maximum allowable in the ArcGIS Pro “Surface Parameters” tool as of version 4.3.3. The window size therefore was 35m x 35m. TPI was stratified into 3 classes (depressions, transitional, and uplands) based on quantiles. Terrain curvature (TC) was developed using the profile curvature option in the Surface Parameters tool using the same neighbourhood window extent for consistency and was stratified into three classes (concave, transitional, and convex) based on quantiles. A larger window size was selected as these appeared to capture overall landscape trends, such as gullies and valleys, effectively without capturing

every slight changes due to rocks or minor depressions, which create more noise than effective measurements (Cartwright et al., 2020).

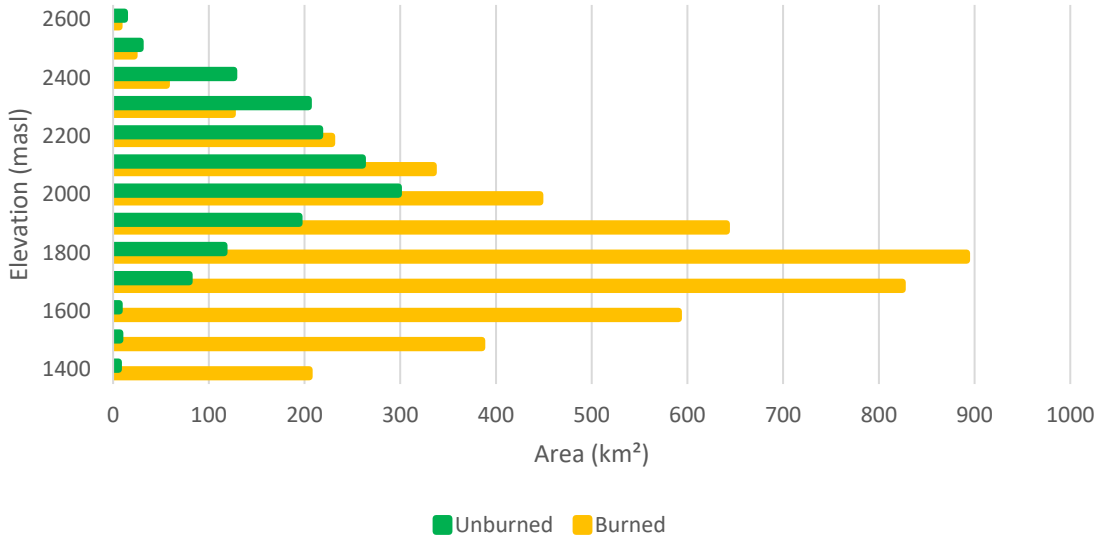

Figure 4.2: The elevational hypsometry distribution of Cameron Valley, divided into the burned and unburned areas.

The canopy cover driver is fractional cover (Fcov) based on the greenness of a summer grid cell as determined by a model which uses the aNBR (active normalized burn ratio) and field and drone ground-truth observations to estimate cover data from a spectral metric (Chapter 2). The aNBR is an index of SWIR and NIR (Equation 4.3), and is typically used in determining burn severity (Aspinall et al., 2025; Chasmer et al., 2017), however, it can also detect increases in vegetation cover over time in early stages of post-fire regeneration. Including field validation data improves the aNBR model to predict fractional cover, rather than only predicting a spectral value, which is not the same as an on-the-ground measured value (Chapter 2; Equation 4.4). The snow depths were compared to the Fcov in the preceding year where data was available, or closest in the case of the winter of 2018 where no preceding lidar survey was available. Fcov was

stratified into five classes based on quantiles, from no vegetation, to little, moderate, high, and most vegetation cover.

Equation 4.3: aNBR = (NIR-SWIR)/(NIR+SWIR)

Equation 4.4: $Fcov = 12.37(aNBR + 0.65)^{2.49}$: where $aNBR \geq -0.65$

4.3.4.3. Statistical Tests

To determine statistical significance between classes over the study period, the snow depth means for each year within each class were run through a Kruskal-Wallis (KW) test. The data do not fit a Gaussian curve and therefore are non-parametric, so the non-parametric version of analysis of variance (ANOVA) was run. To determine which stratum within each driver had the maximum and minimum snow depths overall, and the sums of those ranks used in the KW test were compared. If a stratum had the highest sum of ranks, it was determined to consistently have the most snowpack, and vice versa for the least snowpack. This was validated by comparison with the box plots and rose diagrams.

In terrain drivers with only two or three classes (TPI and TC), the Mann-Whitney (MW) test was applied to determine if there were statistically significant differences in the snow depth between the classes. This was also applied to the means of the burned and unburned areas for non-stratified snow depth across those regions.

Once the relationships between each driver and snow distribution was developed individually, the generalized linear regression (GLR) tool in ArcGIS Pro (version 3.3.2) was used to determine a multivariate relationship between snowpack depth and multiple terrain and vegetation drivers. Additionally, for graphs that present individual snow

surveys (aspect, Fcov, and GLR), these are sorted into accumulation-phase and ablation-phase for easier comparison.

4.4. Results

4.4.1. Lidar Validation and Quality Control

Only the 2024 and 2025 flights had time coincident field data in the study period. At both the 1m and 5m grid cell spatial resolutions, the LSDM tended to underestimate the field measured snow depth by approximately 10% (Figure 4.3). The lidar is sufficiently accurate with the field measurements for determining spatial patterns in snow depth across the valley in the 2018-2025 timeframe.

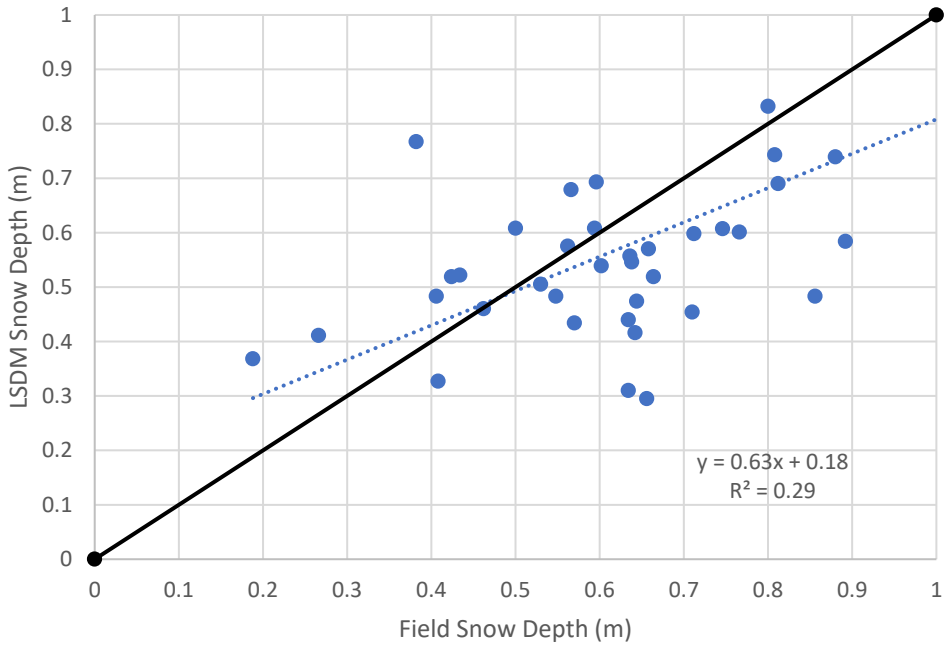

a)

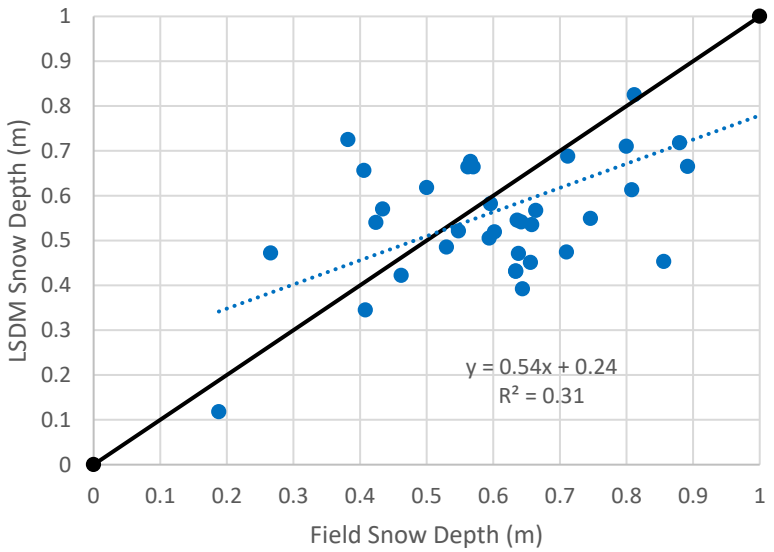

b)

Figure 4.3: The lidar quality control from the field, showing the lidar tends to underestimate the deeper snow depth and overestimate shallower snow depth measured in the field, at the)1m and b)5m grid cell resolutions.

4.4.2. Snow Depth in the Burned and Unburned Areas

The mean absolute and normalized snow depths were compared for each survey in both the burned and unburned areas. This is a singular value collected for the survey polygon as defined in Figure 4.1. The results of the unstratified comparison between the two areas is presented in Figure 4.4. There is a significant difference in both the absolute snow depths between the two regions and in the normalized snow depths (MW, $p<0.01$). Snow depth is lower in the burned area than in the unburned areas of Cameron Valley in most years, except for 2018 which was a higher snowpack year (Figure 4.4).

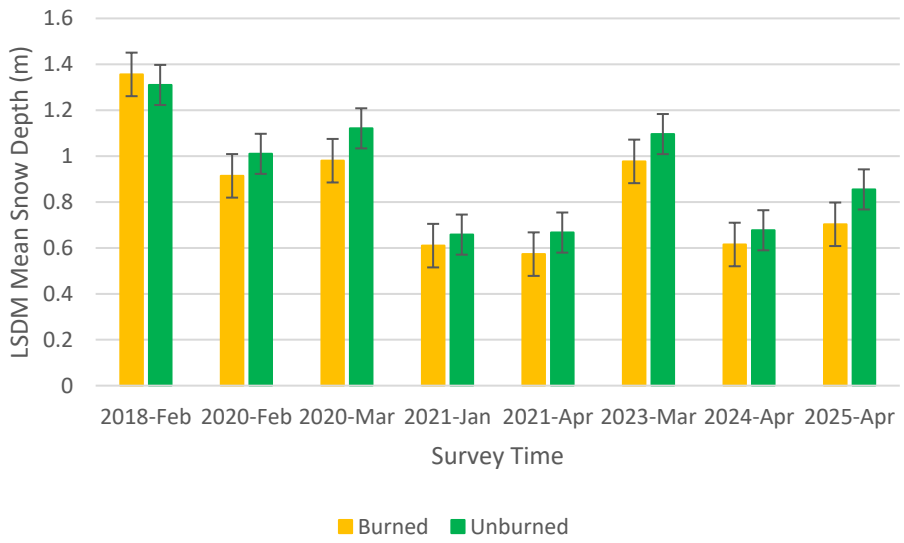

Figure 4.4: A comparison of the mean and standard deviations of the snow depths using absolute snow depth from the LSDM.

4.4.3. Snow Depth by Terrain Driver

The absolute snow depth was tested against the 100m elevation bands in both the burned and unburned areas to determine the general patterns of snow distribution (Figure 4.5). The snowpack hypsometry varies significantly between the burned and burned areas, and snowpack is significantly deeper in the burned areas than in the unburned areas (MW, $p<0.05$).

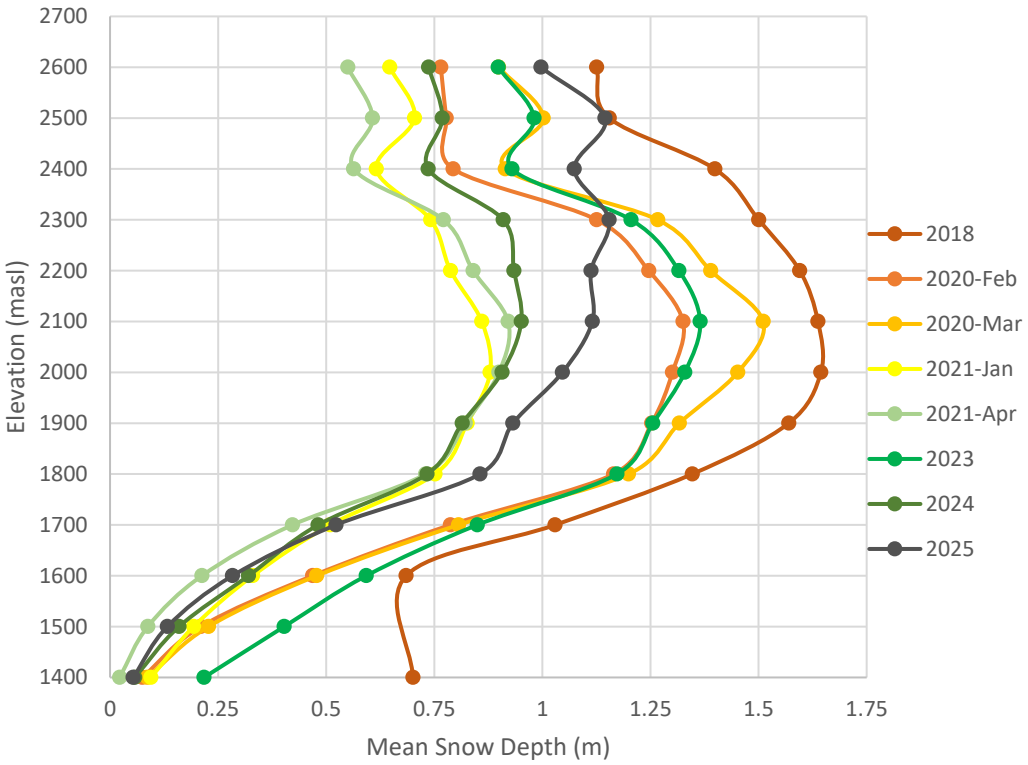

a)

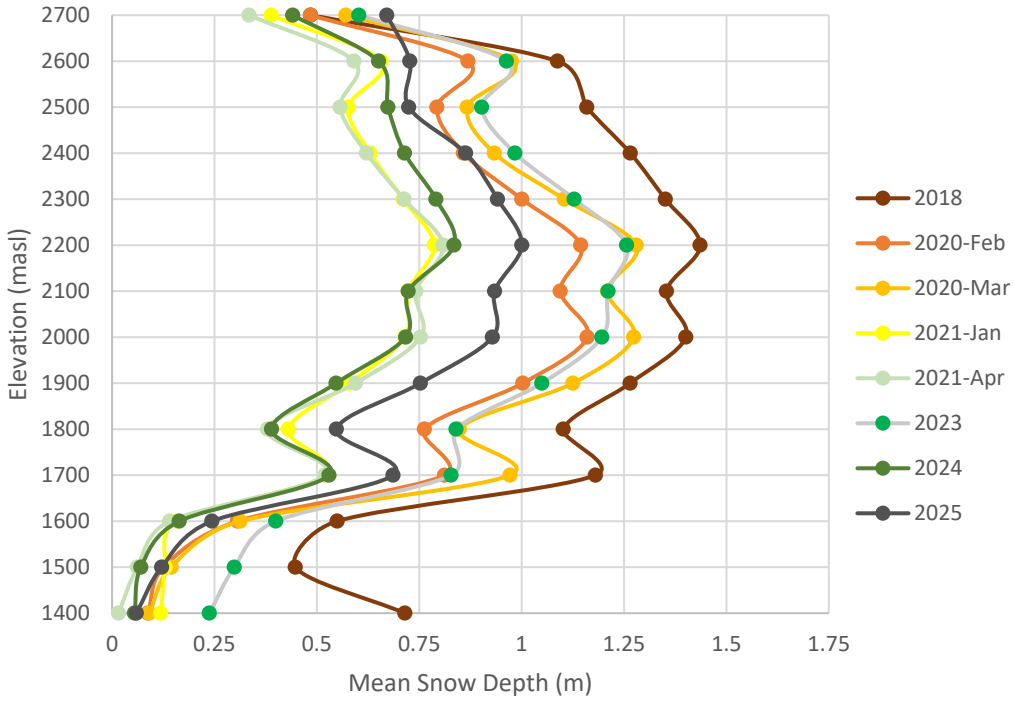

b)

Figure 4.5: Scatter plots of the snow depth by elevation band in Cameron Valley in the a) burned and b) unburned areas for all surveys.

The snow hypsometry presented in Figure 4.5 shows that the maximum snow depth shifts upwards in elevation over time. It is important to note that the surveys from April 2021 to 2025 were conducted during the ablation dominated season, at which point some snow could be melting out from the lower elevations, however, the maximum snow depth shifted up between 2018 and January 2021 as well, during the accumulation season. More of the snow occurs at the 1700 masl to the 2200 masl range in the burned area due to the distribution of the elevation of the terrain in the burned area. However, in the unburned area, most of the snowpack is 2000 masl and 2400 masl as that is the distribution of the terrain in the unburned area. Both regions show that maximum snowpack tends to occur around treeline, or the former treeline area in the case of the burned area.

The relative proportion of snow volume by elevation band in the burned area is presented in Figure 4.6. Generally, the same pattern occurs in each survey, with lower snow volumes occurring in the lowest and highest elevations, and the highest snow volume occurring at approximately 1800-2000 masl. The proportion of the highest snow volume changes in each year, with a higher proportion of the overall snow depth occurring at higher elevations in 2025 than in 2018. This is supported by the mean snow depth changes presented in Figure 4.5 where maximum snowpack depth shifted in the burned area from 1900masl in 2018 to 2300 masl in 2025, with it fluctuating between 2000-2100masl in the surveys between. For contrast, the maximum snowpack depth in the unburned area remained at 2200 masl in all surveys except for the 2020 survey. In both regions, the snow depth was greatest between 2000 and 2200 masl, and lowest between 1400 and 1600 masl.

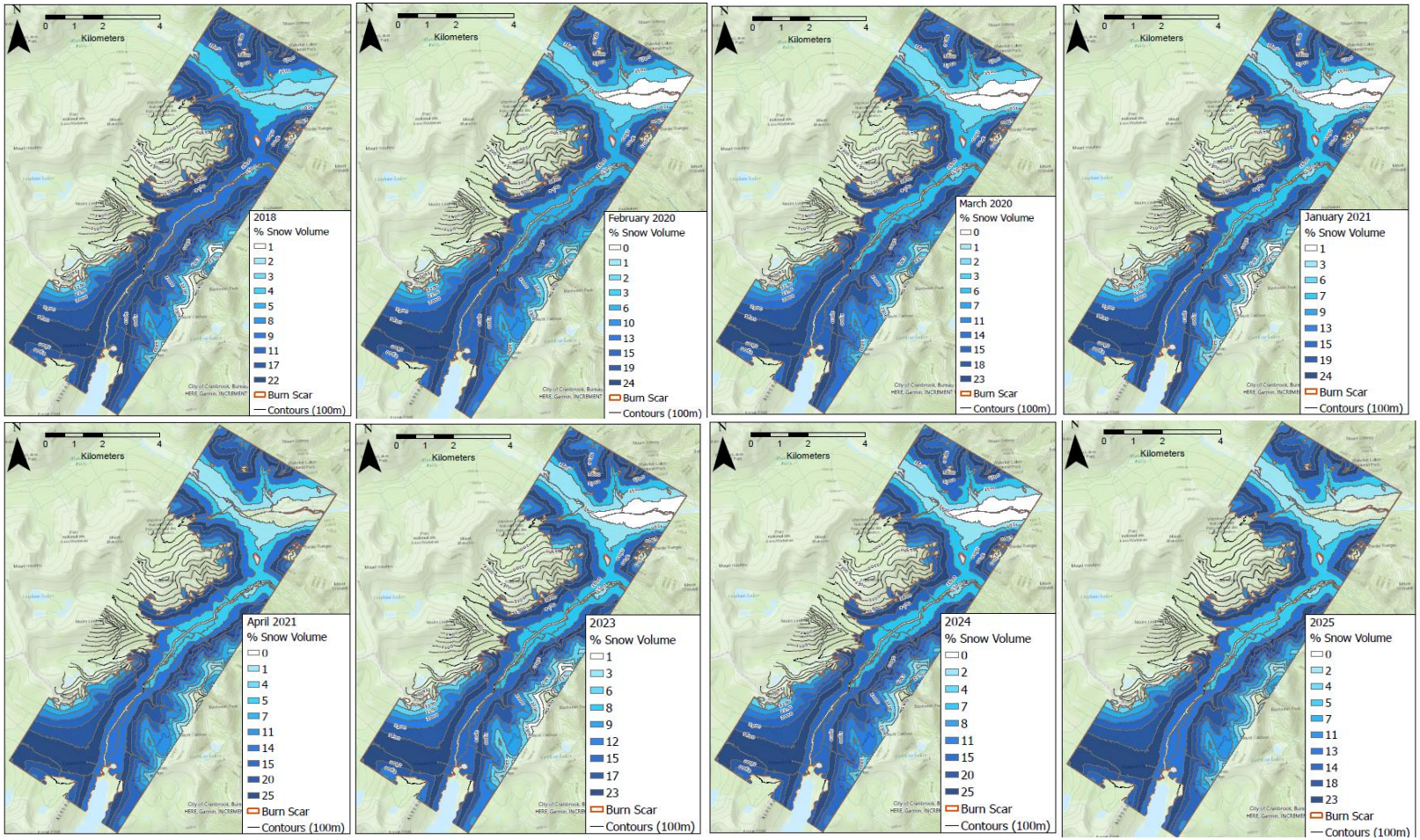

Figure 4.6: Spatialized snow depth volume by percent in Cameron Valley for each survey from 2018 to 2025.

Aspect was stratified into 8 classes based on cardinal directions. The KW test showed that both the unburned and burned areas have significant differences between the classes. Snow depth is consistently significantly greatest in the north and northeast facing slopes in both regions. The shallowest snow depth in both the burned and unburned areas occurred in the south and southwest facing slopes. The stratified snow depth by aspect is presented in Figure 4.7 and Figure 4.8 as rose diagrams for each survey in both regions in the accumulation (Figure 4.7) and the ablation (Figure 4.8) stages of the winter.

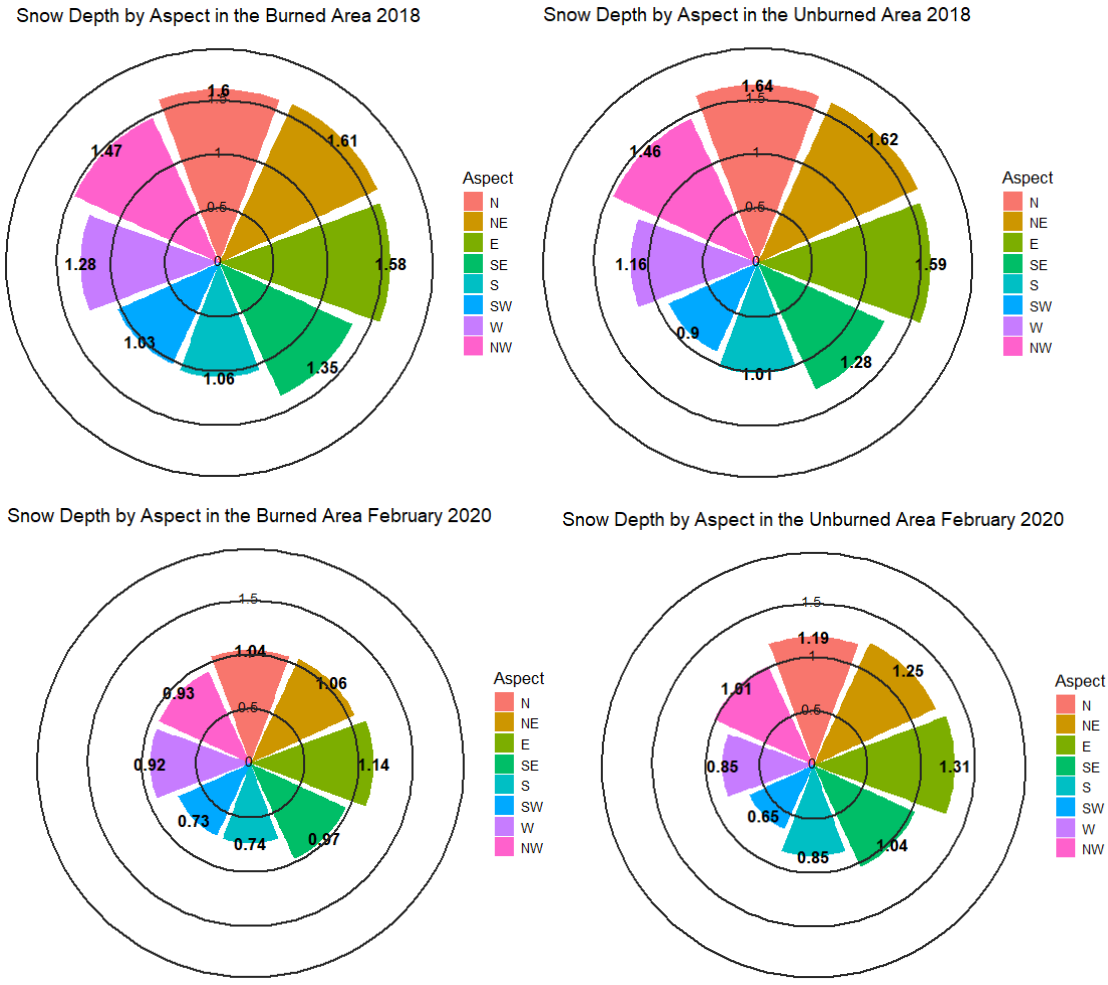

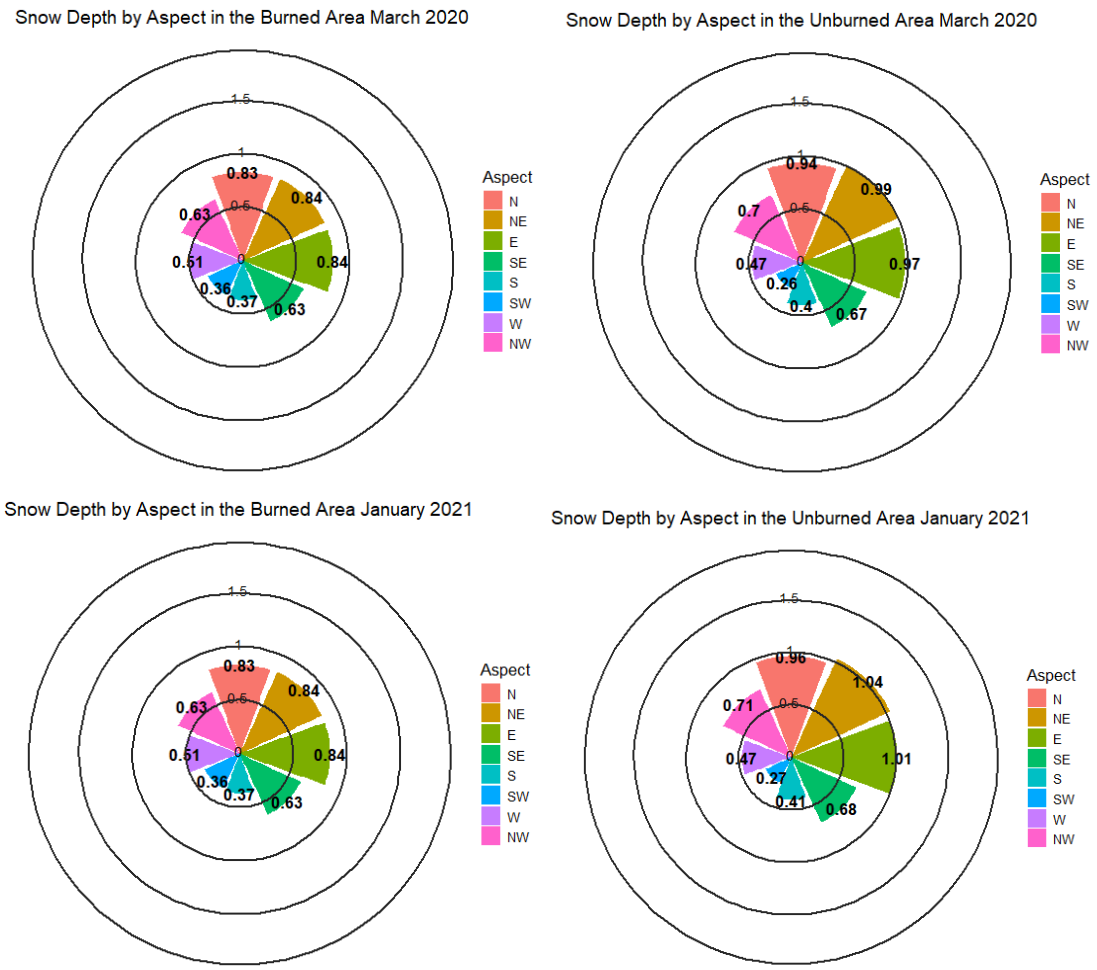

Figure 4.7: Rose diagrams of the snow depth in meters by stratified by aspect for the accumulation phase from 2018 to January 2021, showing the burned and unburned areas.

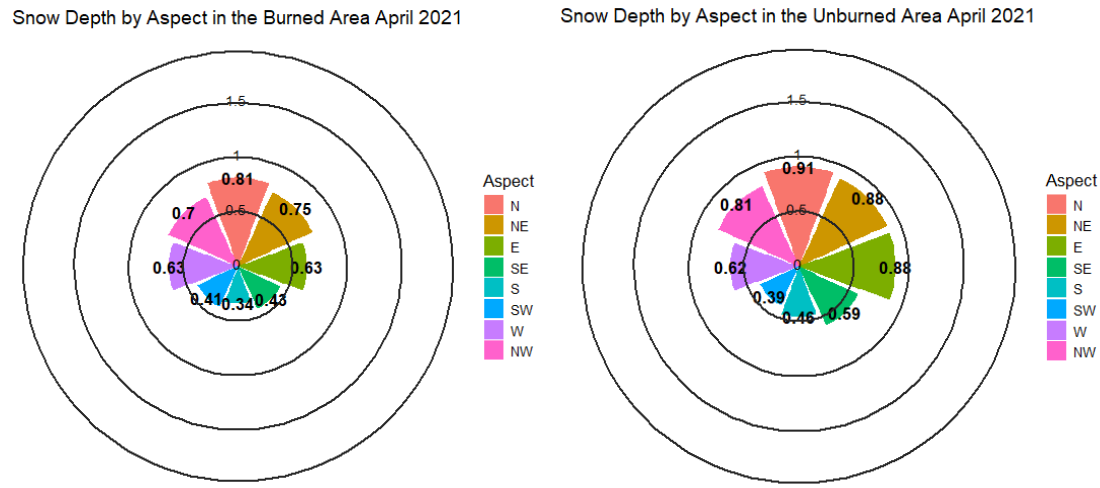

Figure 4.8: The rose diagrams of meters of snow depth stratified by aspect in the ablation phase of the winter, showing the burned and unburned snow depths in each direction.

The normalized snow depth by TPI class is presented in Figure 4.9. The snowpack in the depressions is significantly higher than in both the transitional and upland areas (MW: $p<0.05$).

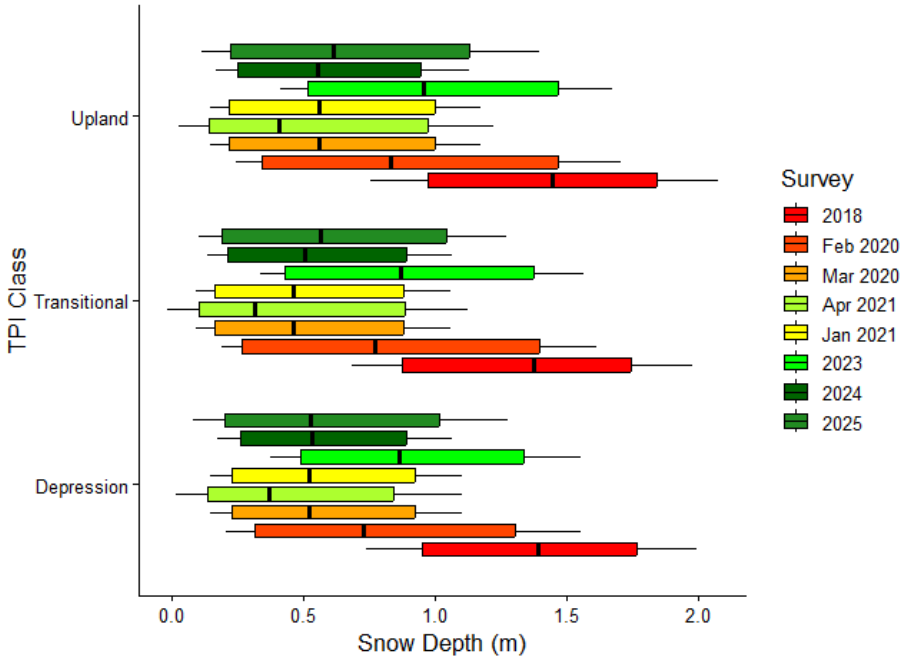

Figure 4.9: Box plots of snow depth by TPI class in the burned area for all surveys, showing the mean and standard deviation of the snow depth in each strata.

The snow depth by TC class is represented in Figure 4.10. In the burned area, there is no significant difference in snow depth with TC class. However, in the unburned area, there was significantly more snow in the concave areas than in either the flat or convex areas (MW, $p<0.05$). Additionally, the concave areas had more snow than the flat areas in the unburned areas (MW, $p<0.05$)

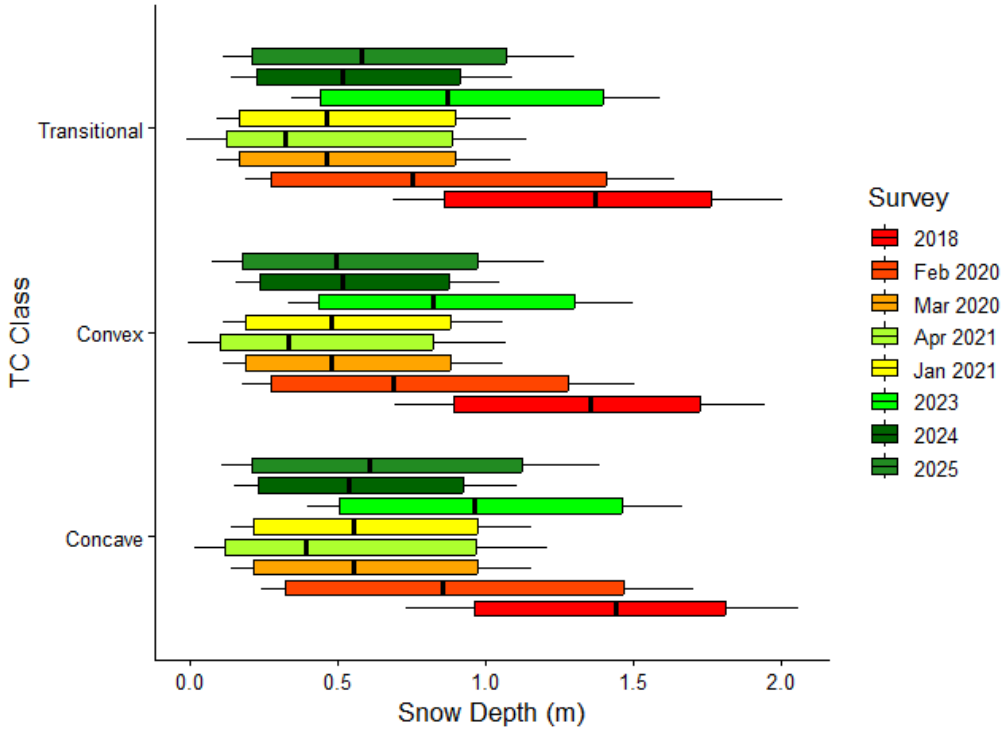

Figure 4.10: Box plots of the mean and standard deviation of the snow depth stratified by terrain curvature in the burned area.

4.4.4. Snowpack Depth by Vegetation Cover

The final driver that was tested was the vegetation cover for each respective year, as determined from the closest summer survey and the stratified Fcov of that survey. Each snow survey is presented with their respective vegetation survey in Figure 4.11. The areas of the burn scar with little to no vegetation had significantly deeper snowpack than the vegetated areas in most years (MW: $p<0.05$). The quantile approach for the vegetation cover split the cover into classes called “none” for 0% cover, “little” cover for 1% to-approximately 10%, “moderate” cover for 11-25%, “high” cover for 25-50%, then “most” cover for over 50%

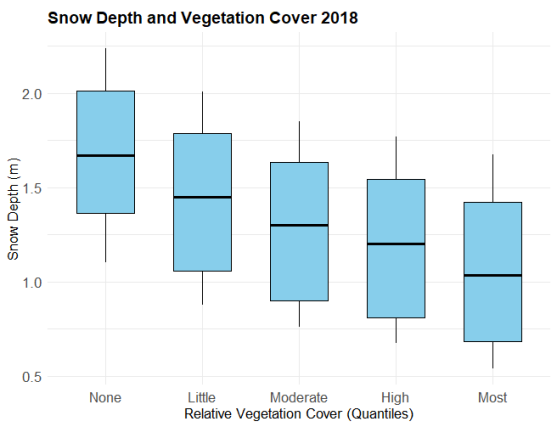
Snow Depth and Vegetation Cover 2018
Snow Depth (m)
2.0
1.5
1.0
0.5
None
Little
Moderate
High
Most
Relative Vegetation Cover (Quantiles)

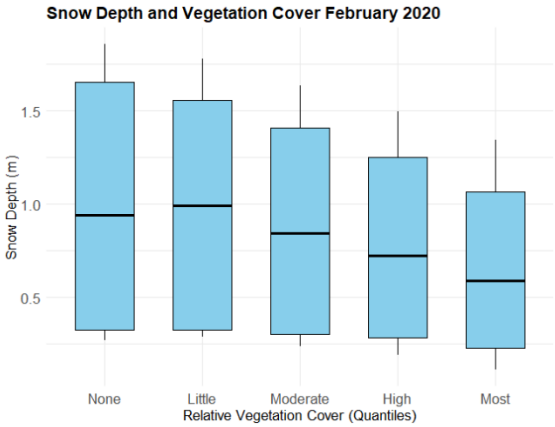
Snow Depth and Vegetation Cover February 2020
Snow Depth (m)
1.5
1.0
0.5
None
Little
Moderate
High
Most
Relative Vegetation Cover (Quantiles)

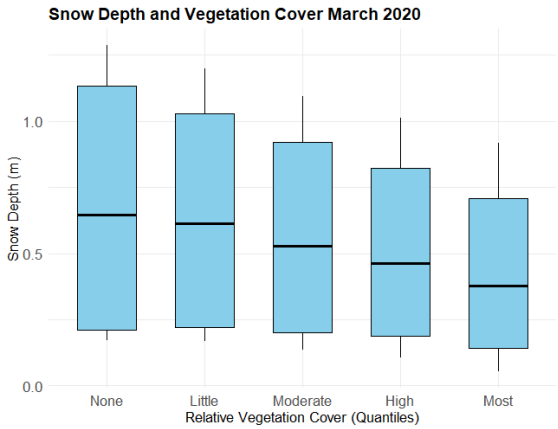
Snow Depth and Vegetation Cover March 2020
Snow Depth (m)
1.0
0.5
0.0
None
Little
Moderate
High
Most
Relative Vegetation Cover (Quantiles)

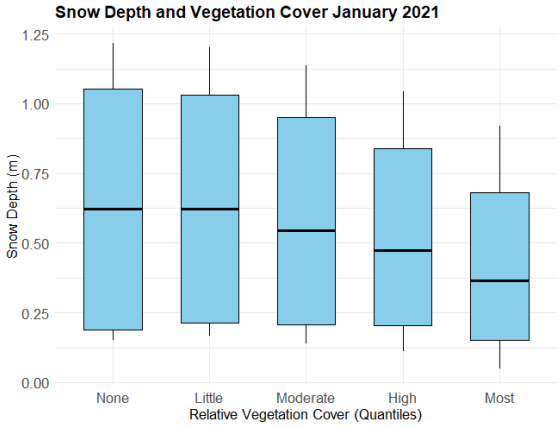
Snow Depth and Vegetation Cover January 2021
Snow Depth (m)
1.25
1.00
0.75
0.50
0.25
0.00
None
Little
Moderate
High
Most
Relative Vegetation Cover (Quantiles)

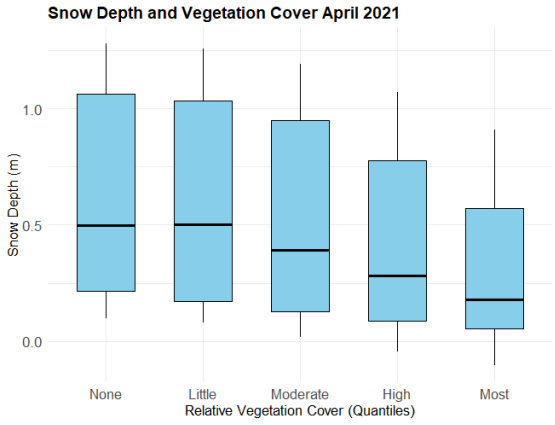
Snow Depth and Vegetation Cover April 2021
Snow Depth (m)
1.0
0.5
0.0
None
Little
Moderate
High
Most
Relative Vegetation Cover (Quantiles)

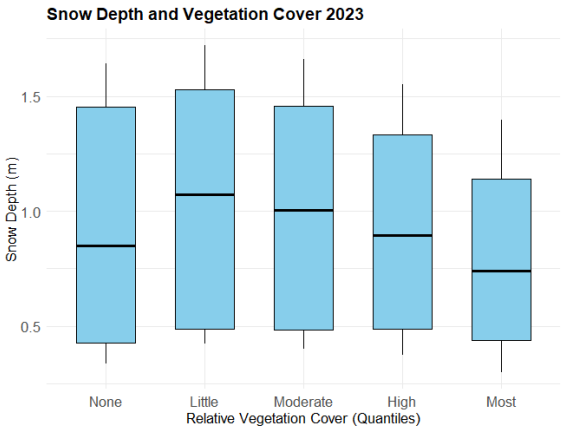
Snow Depth and Vegetation Cover 2023
Snow Depth (m)
1.5
1.0
0.5
None
Little
Moderate
High
Most
Relative Vegetation Cover (Quantiles)

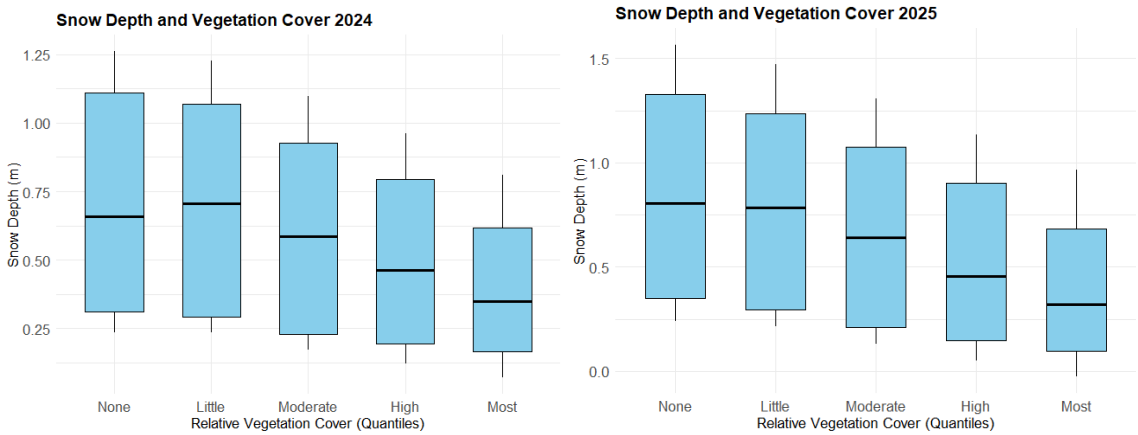

Figure 4.11: Box plots of the mean and standard deviation of snow depth stratified by the corresponding vegetation cover survey in the burned area.

4.4.5. Generalized Linear Regression Results

Each snow survey compared to each driver described above in the generalized linear regression tool. The results are presented in Figure 4.12 below. Similar results and correlations occurred in all years, regardless of the time of winter when the survey was collected. Snow depth was positively correlated with elevation and negatively correlated with vegetation cover. Additionally, elevation and vegetation cover were negatively correlated with each other.

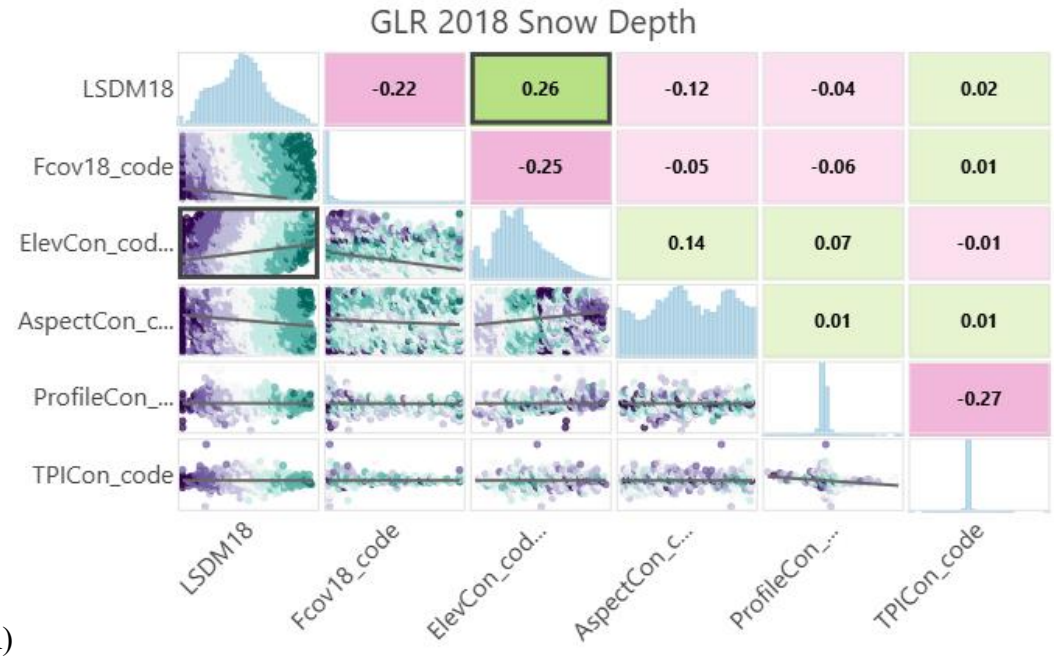
GLR 2018 Snow Depth
LSDM18
Fcov18_code
ElevCon_cod...
AspectCon_c...
ProfileCon_...
TPICon_code
-0.22
0.26
-0.12
-0.04
0.02
-0.25
-0.05
-0.06
0.01
0.14
0.07
-0.01
0.01
0.01
-0.27

A)

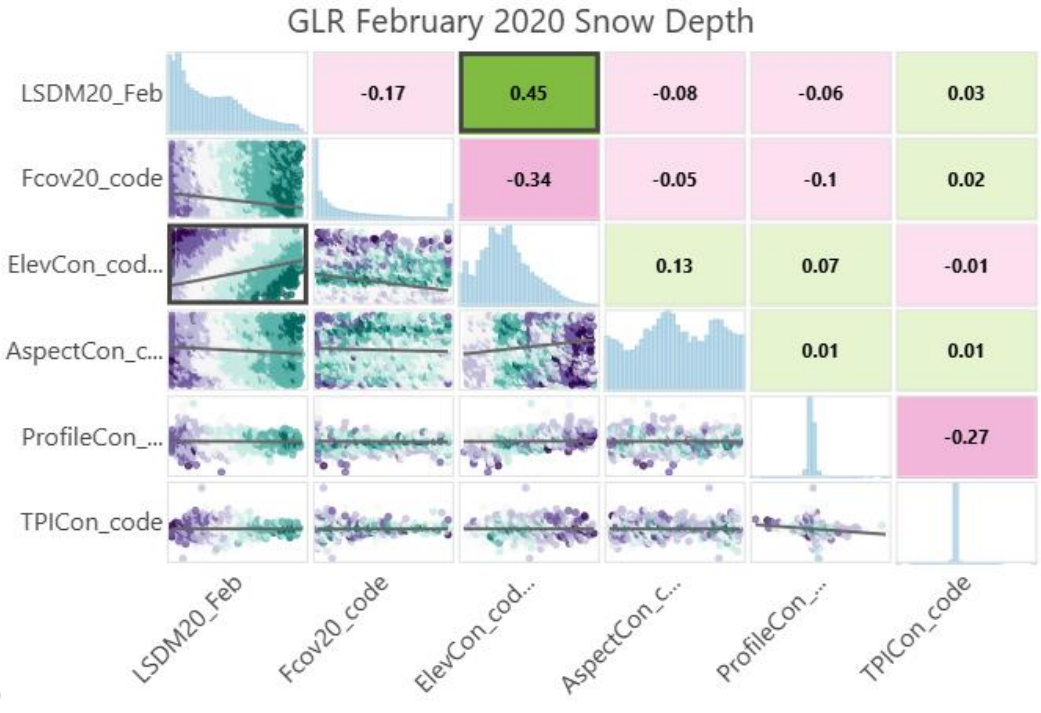
GLR February 2020 Snow Depth
LSDM20_Feb
Fcov20_code
ElevCon_cod...
AspectCon_c...
ProfileCon_...
TPICon_code
-0.17
0.45
-0.08
-0.06
0.03
-0.34
-0.05
-0.1
0.02
0.13
0.07
-0.01
0.01
0.01
-0.27

B)

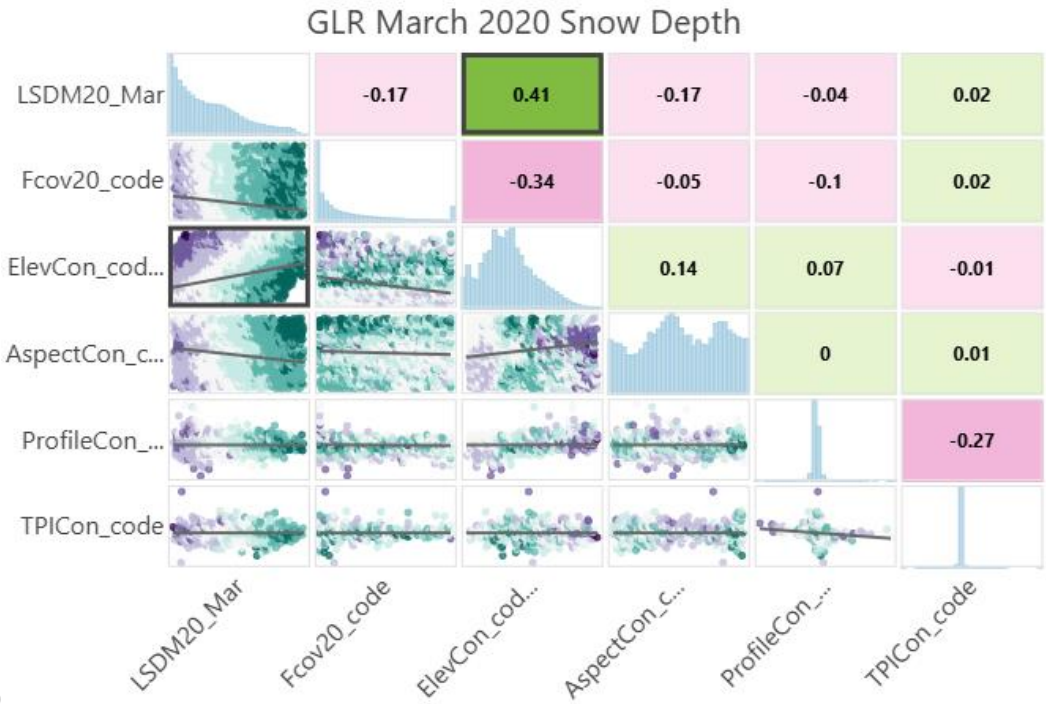
GLR March 2020 Snow Depth
LSDM20_Mar
Fcov20_code
ElevCon_cod...
AspectCon_c...
ProfileCon_...
TPICon_code
-0.17
0.41
-0.17
-0.04
0.02
-0.34
-0.05
-0.1
0.02
0.14
0.07
-0.01
0
0.01
-0.27

C)

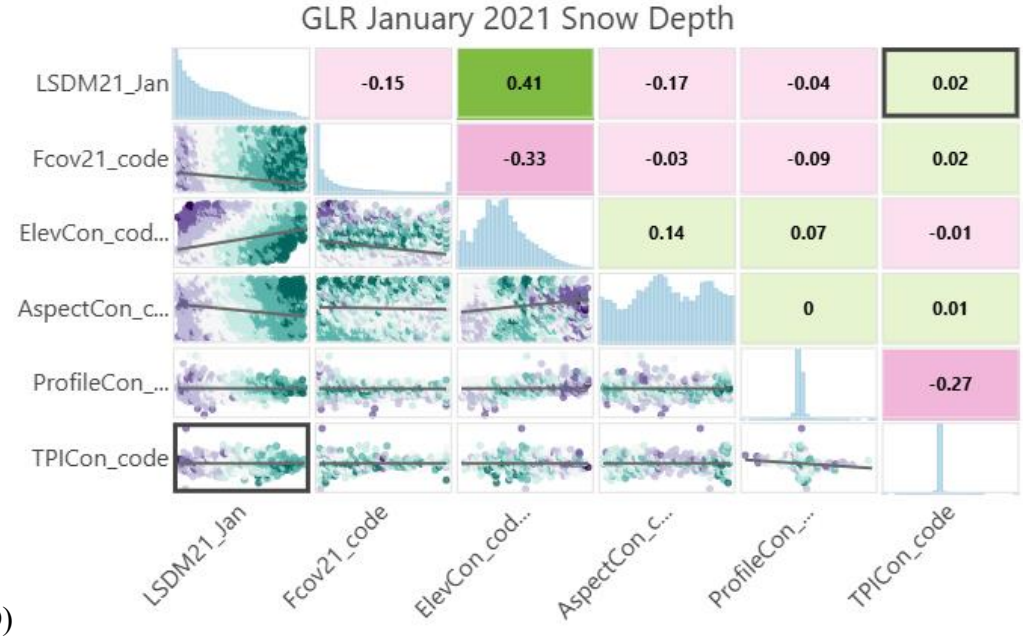
GLR January 2021 Snow Depth
LSDM21_Jan
Fcov21_code
ElevCon_cod...
AspectCon_c...
ProfileCon_...
TPICon_code
-0.15
0.41
-0.17
-0.04
0.02
-0.33
-0.03
-0.09
0.02
0.14
0.07
-0.01
0
0.01
-0.27

D)

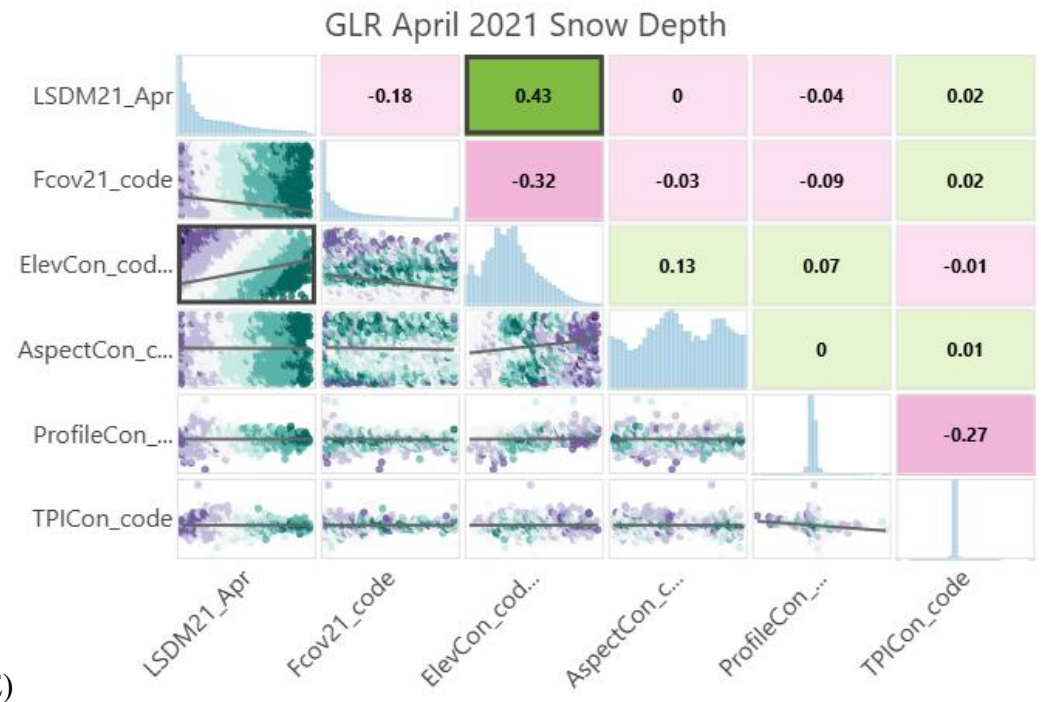
GLR April 2021 Snow Depth
LSDM21_Apr
Fcov21_code
ElevCon_cod...
AspectCon_c...
ProfileCon_...
TPICon_code
-0.18
0.43
0
-0.04
0.02
-0.32
-0.03
-0.09
0.02
0.13
0.07
-0.01
0
0.01
-0.27

E)

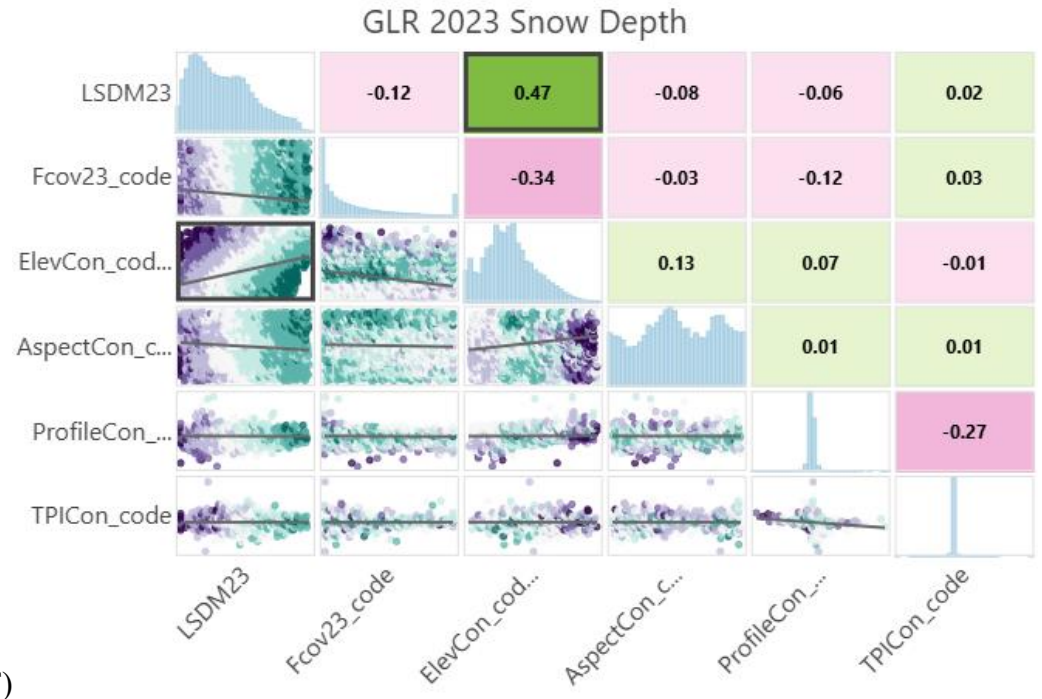
GLR 2023 Snow Depth
LSDM23
Fcov23_code
ElevCon_cod...
AspectCon_c...
ProfileCon_...
TPICon_code
-0.12
0.47
-0.08
-0.06
0.02
-0.34
-0.03
-0.12
0.03
0.13
0.07
-0.01
0.01
0.01
-0.27

F)

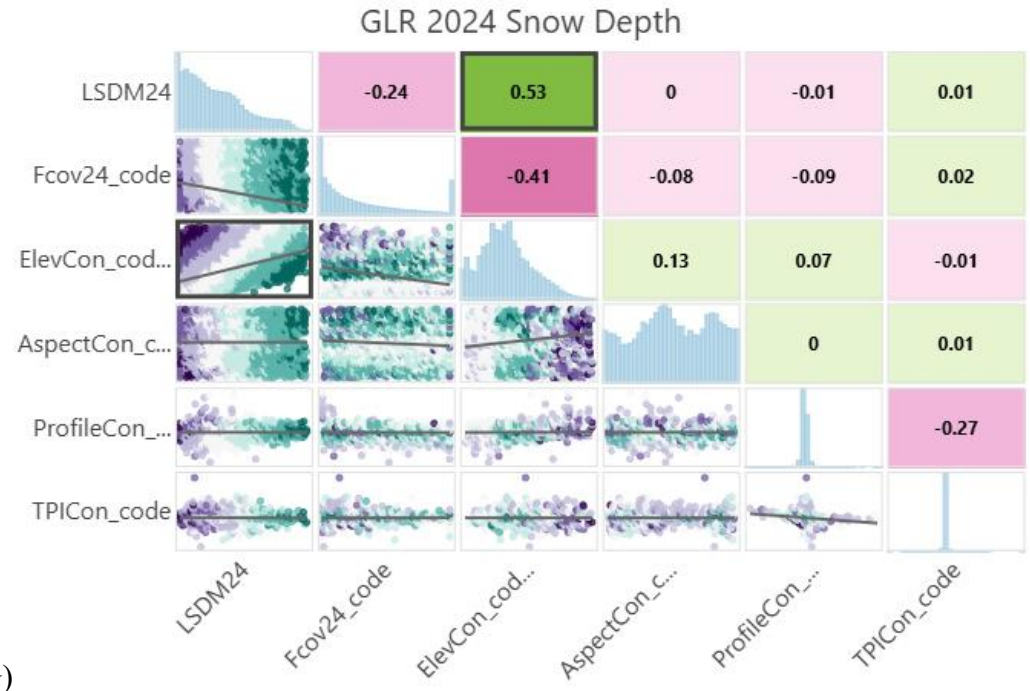

G)

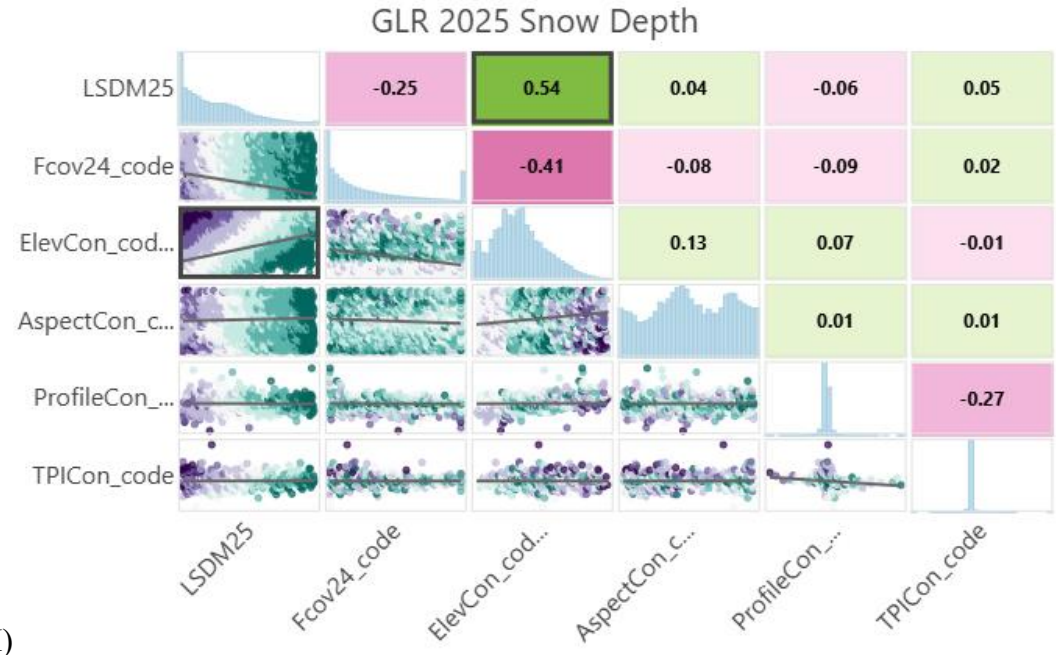

H)

Figure 4.12: The results of the GLR for the accumulation phase surveys for a)2018, b) February 2020, c) March 2020, and d) January 2021, and for the ablation phase sruveys for e) April 2021, f) March 2023, g) April 2024, and h) April 2025. The prefixes refer to the driver type, the code is the value associated with the driver. LSDM = Snow depth (m), Fcov = fractional cover (%), Elev = elevation (masl), Aspect = Directional Aspect (°), Profile = Terrain Curvature, and TPI = topographic position index. The top left boxes are the Pearson's r value of each relationship, where pink boxes indicate a negative correlation and green boxes are positive correlations. The bottom left boxes are the scatterplots of residuals, and purple indicates a negative residual, while teal indicates a positive residual.

4.5. Discussion

4.5.1 Snowpack Distribution Across Cameron Valley

Snow depth is highly heterogenous across CV, and the snowpack volumes shift from year due to the annual meteorological conditions. Field snowpack depth measurements aligned well with the LSDM models for 2024 and 2025, with correlations with an r^2 of 0.9. The lidar tends to overestimate the snow depth by 10%, which is expected from previous studies (Barnes et al., 2025; Broxton et al., 2019; Hopkinson et al., 2024; Smoot & Gleason, 2021; Van Gaalen et al., 2024). Snow depth was significantly different between the burned and unburned areas, even before any terrain stratification beyond fractional cover was applied. The snow tended to be deeper in the burned, open areas, as shown in the figures relating snow depth to terrain stratifications, which is expected based on the reduced canopy interception of snowpack (Broxton et al., 2021; Giovando & Niemann, 2022; Maxwell & Clair, 2019; Pomeroy & Gray, 1995). The unburned area appears to have more snow than the burned area based on Figure 4.4, which is opposite of what is expected, however, this likely can be attributed to the fact that the mean elevation of the unburned area is higher than the mean elevation of the burned area. Since greater precipitation volume occurs at higher elevations typically, and each snow depth value for each survey presented in Figure 4.4 is a singular mean snow depth of the whole region. However, Figure 4.4 does show that there is a difference in snow depth between the two areas prior to stratification. February 2018 had the greatest snow depth of all surveys, and the April 2021 was the lowest snow year. These years provided useful information about what to expect in snow distributions in variable hydro-meteorological conditions.

4.5.2. Elevation and Changing Snowpack Maximum Depths

The location of the maximum snow depth shifted upwards by 400 m over the eight years since the fire, as demonstrated in Figure 4.5. The maximum snow depth elevation occurred at 1900 masl in 2018, and by 2025 that elevation was 2300 masl, which is right around the treeline ecotone in CV (Aspinall et al., 2025; McCaffrey & Hopkinson, 2020). From 2020 to 2024, the maximum snow depth fluctuated between 2000 and 2100 masl, with 2023 and 2024 having their maximum snow depth at the 2100 masl band. This suggests that the snowpack shifts downslope in burn scars and recovers back to the treeline ecotone after approximately 8 years. The maximum snow depth elevation in the unburned area fluctuated between 2000 and 2200 masl, which is relatively close to the treeline ecotone also, regardless of timing of the survey (accumulation or ablation phase), suggesting the vegetation is useful for maintaining snowpack for longer in the season. Therefore, the maximum snow depth is related to the vegetation cover available and recovery over time.

4.5.3. Aspect, TPI, TC, and Snowpack Distribution

Aspect both significantly impacted the snow depth distribution. The snow was also deepest on north and east facing slopes across the entire valley, likely due to the reduced direct solar radiation, and therefore reduced melt energy input into the system, allowing for the snow to accumulate, rather than melt or sublimate (Barnes & Hopkinson, 2022a; Cartwright, 2018; Marsh et al., 2012). Snow was significantly reduced on the south and southwest facing slopes. These are the areas that receive the most sunlight, sensible heat energy, and radiative energy, as well as being the areas that experience the most direct winds most consistently due to the regular Chinook winds in the area (Avalanche Canada, 2024; MacDonald et al., 2018; Oard, 1993).

Snow tends to accumulate to greater depths in local topography depressions and concavities, as is evident by the TC. The TPI results were opposite of what was expected, with greater depths occurring in uplands than in depressions. This could be due to the window size, as it may be picking up more detail than needed, as it is relativity small compared to those used in other studies (Cartwright, 2018). While these drivers have less influence on the snow depth than elevation or aspect, they are still important in determining local snow depth distribution (Avalanche Canada, 2024; Cartwright, 2018; Pomeroy & Gray, 1995).

4.5.4. Vegetation Regeneration and Snowpack Distribution

Vegetation cover was highly influential on snowpack. The burned areas had significantly deeper snow in areas with little to no fractional cover than in regions with greater fractional cover. This is likely due to the longwave radiation that is emitted from the saplings and smaller woody shrubs increasing the energy input into the snowpack (Gersh et al., 2022; Gleason et al., 2013; Smoot & Gleason, 2021). The benefits of vegetation shading the snow from the solar radiation are not yet present due to the young stage of the vegetation, so the vegetation does not yet have sufficient foliage to prevent the direct radiation from reaching the snow surface. As the vegetation recovered over time, greater amounts of snow accumulated in the regions with ‘little’ vegetation than the no cover vegetation class.

4.5.5. Generalized Linear Regression

Snowpack depth is correlated with elevation and vegetation cover most strongly, but in opposite directions. Increasing vegetation cover tends to decrease snowpack, and increasing elevation tends to increase snowpack (Barnes & Hopkinson, 2022b), both of which are expected results, as snowpack tends to increase with elevation, but interception

of snow by vegetation decreases the snow on the ground (Pomeroy, Parviainen, et al., 1998). Elevation and vegetation cover are negatively correlated to each other, which is supported by the results presented in Chapter 3. Aspect becomes a less correlated driver with snowpack in the later years as vegetation cover increases. While TPI and TC do not show a significant correlation in the GLR, they are important in the system, and the GLR may not be capturing that importance. Additionally, GLR can inflate the effects of more correlated drivers, such as elevation, causing other less correlated but still important drivers to appear as though there are insignificant, due to a statistical problem of mixed effects. Future research should further separate out the drivers to removed mixed effects from the model, likely by using another type of machine learning that better supports non-parametric data.

4.5.6. Sources of Error and Limitations

Potential sources of error in the LSDMs include the lidar technology itself. On steeper slopes, the footprint of the laser 'shrinks' to a smaller area than it typically would on a flat surface scanned at nadir, and therefore terrain-induced errors can occur regarding positional alignment (Baltsavias, 1999; Deems et al., 2013). Other potential sources of error include the potential for horizontal or vertical misalignments between the snow-on and snow-off lidar surveys which may have been missed in the post-processing quality control and assurance steps. Additionally, field measurements used for aligning and quality control of the lidar could be a source of error, with avalanche probes being only accurate to the nearest centimeter, and to allow for error with the ground surface below the snow.

A potential source of error is the presence of senesced vegetation and downed woody debris in the region. This vegetation debris can result in snow depth values appearing as though they are greater than they truly are, due to the interference of this debris between the snow and the ground (Hopkinson, Sitar, et al., 2004). There is also the potential that the snow surface appears shallower than it is if the vegetation is occluding the true ground surface, especially if using a DEM from a later post-fire recovery year. These sources were attempted to be corrected for in the initial quality control process by setting LSDM values below -0.1m to 0m, to account for the shallower snow depth issue (Hopkinson et al., 2024; Van Gaalen et al., 2024). Additionally, using the earliest completed DEM available helps to reduce the occlusion of the ground surface in the snow-off lidar point cloud, with the goal of increasing the accuracy of the terrain driver surface.

4.5.7. Future Research

This work discusses changes in snow depth distribution across a burned mountain valley, which is a critical headwater source for many communities downstream. Future work could look at the snow water equivalence of these absolute snow depths to determine the amount of water available for that point in time each year. Field samples of density are required and were taken at the same time as the field depth measurements used for validation. Additionally, there is the possibility that some multi-spectral index could be generated from lidar or other remote sensing which may be useful for density (Hopkinson et al., 2024). Collecting more surveys during winter could also help to further understand the dynamics of snowpack within a winter, and between years, which would further information hydrological models for water resource calculations for flood

modeling and water use allocations on a larger scale than the current point meteorological stations can support (Hopkinson et al., 2024). As the region recovers, it would also be recommended to study the hydrographs of the region to see how long it will take for the hydrographs to match the patterns of the region before the fire, to quantify hydrological recovery. Continued snowpack lidar surveying is recommended as the ecosystem continues to recover from the fire to increase our understanding of ecosystem dynamics in post-fire sits as fires become more common and more severe (Parks et al., 2025).

4.6. Conclusions

Snowpack is a critical source of water for southern Alberta. Wildfires can alter the distribution of snowpack by changing the vegetation cover and distribution. Snowpack depth varies significantly between burned and unburned areas of the Cameron Valley. The maximum snow depth shifts downslope immediately following the fire and in earlier post-fire years but recovers to the same elevation as the unburned area within eight years of the fire as the vegetation regenerates over the area. Continued monitoring of the snowpack resources using lidar is recommended to determine further changes in snowpack distribution as the region regenerates following the fire, to find if snowpack distributions stabilize with changing vegetation. Snowpack distributions changes are critical for water resource considerations, therefore, understanding that the snowpack distribution is impacted significantly by post-fire vegetation regeneration can inform future research into modelling for water management decisions.

5. Chapter 5: Conclusions

5.1 Discussion of Major Results

Vegetation is consistently recovering in the Cameron Valley in the Kenow Wildfire burn scar in the seven-year time frame studied. Vegetation cover and height are both known to be effective measures for determining vegetation growth over time, however, in this early-stage vegetation regeneration case, cover is the more effective measure. This is because the spectral differences and changes are more accurate observations at this point in the regeneration trajectory than height. Height measures are highly variable with inter-annual hydro-climatological influences and with annual species. Therefore, height is expected to become a more useful measure of vegetation cover approximately 10-15 years post-fire, as the woody vegetation, including coniferous species, increase in height consistently beyond the height of the annual vegetation (approximately 3m). Vegetation cover measures saturate after 5 years in riparian areas and 7 years upland areas and therefore are not useful for detecting further vegetation growth after this point.

Using a combination of field, RPAS, and airborne lidar data was useful for detecting changes in vegetation. Field vegetation cover measured at the ground surface using a binary threshold of greenness successful informed a similar RPAS model, which was applied spatially to convert aNBR to a vegetation cover metric, fractional cover. The final transfer equation provides an idea of the fractional cover at a larger scale, using only multi-spectral lidar data.

Using the vegetation cover and the DEM derived from the lidar point cloud, the post-fire vegetation regeneration distribution could effectively be determined across

Cameron Valley. There were significant differences vegetation cover distribution between burned and unburned regions of the study area. Recovering vegetation reached a maximum cover proportion at 1600masl, and the maximum occurred at 1800-1900masl in the unburned area. Vegetation was also significantly associated with aspect slope, TPI, and TC. This indicates that aspect and solar radiation input is critical in early post-fire recovery, as is distance to the water table. Vegetation cover has significantly increased in all classes of each driver and continued monitoring of post-fire regeneration is critical to understand post-fire climate change environments to accurately inform future land management decisions.

Snowpack depth and distribution are highly variable between the burned and unburned areas and are influenced by a variety of terrain and vegetation drivers. Maximum snow depth in the burned area shifted downslope in the first few years of post-fire recovery due to the removal of the treeline, and it shifted back up to the original treeline ecotone elevation within eight years of post-fire recovery. All the tested drivers are significantly influential on snow depth. Mid-slopes, north-facing, concavities, and non-vegetated areas between 2000-2300masl had the greatest snow depth in the burned areas. Snow depth and distribution are highly connected to post-fire vegetation recovery and the local terrain, and continued surveying of the snowpack resources is critical in understanding continuing changes in water resources.

5.2. Future Work

Continued monitoring of vegetation cover and height and of snow depth and distribution is recommended, both to validate the future trajectory models and to increase understanding of later post-fire recovery beyond 7-8 years of available survey data.

Continued data collection in the RPAS sites, using standardized field techniques, sampling timing, and the L1 lidar sensor on the RPAS unit, is recommended. Future work can build on this work to find the exact timing when vegetation height becomes a more reliable variable to measure vegetation recovery, or the point at which the variance in the height does not massively exceed the mean and therefore gives a more valuable measurement.

Developing a more complex machine learning model that incorporates the multiple terrain and vegetation drivers is a potential opportunity for taking the single-variable comparisons further, to understand the interactions between the drivers, and then how they impact the vegetation or snowpack. Additionally, the absolute values of snow depth and the terrain and vegetation informing could be used in hydrological modeling to determine post-fire hydrological recovery over time in the region.

A final suggestion for future research is to take the vegetation monitoring framework and snowpack monitoring frameworks presented here for Waterton Lakes National Park, and apply them in another study area, such as Jasper National Park which experienced fires in 2022 and in 2024, to test the spatial transferability of the models between locations.

5.3. Summary of Research Significance

The overall objective of this thesis was to determine the influences of terrain drivers on post-fire ecosystem dynamics in the Cameron Valley of Waterton Lakes National Park, to further the understanding of post-fire vegetation regeneration patterns and snowpack water resource availability in heavily disturbed sites, especially in the context of increasing wildfire occurrence in climate change. This thesis first developed a

post-fire vegetation regeneration monitoring framework that is recommended for future use, which captures both the field level detail and the spatial extent of the entire region. New equations were developed for creating fractional cover models from multi-spectral lidar based on field measured fractional cover. This was applied to understanding how vegetation regeneration patterns are influenced by terrain drivers over time, and finally to understanding snowpack dynamics as the valley recovered over time. Vegetation is returning in this severely burned region. In the burned region, snowpack hypsometry was shown to change over time, because in the winter immediately following the fire, the maximum snowpack depth had shifted downslope by approximately 200 m compared to the unburned area, and by 2025, it had shifted up by approximately 400, indicating that snowpack is related to regenerating vegetation. This is critical for water resources planning and land management decisions, because as the snowpack shifts back to the pre-fire locations, adjustments must be made to downstream water management to adapt to changing peak flow timing and rates in the spring freshet. This research also shows that the ecosystems are resilient to significant change and can rebound from disturbance such as wildfire, and that the terrain drivers and their representation of hydro-climatological variables support the ecosystem resilience of vegetation and snowpack. Terrain drivers are influential on ecosystem dynamics and post-fire recovery in Waterton Lakes National Park, and they support the critical hydro-climatological variables that allow for ecological and hydrological functions.

6. References

Andrus, R. A., Harvey, B. J., Rodman, K. C., Hart, S. J., & Veblen, T. T. (2018). Moisture Available limits subalpine tree establishment. *Ecology*, *99*(3), 567-575. https://esajournals.onlinelibrary.wiley.com/doi/10.1002/ecy.2134

Applied Imagery. (2024). *Quick Terrain Modeler*. Applied Imagery. https://appliedimagery.com/

Aspinall, J. (2023). *Assessing the State of Initial Post-Fire Vegetation Regeneration Following a Severe Montane Wildland Fire* University of Lethbridge]. Lethbridge, Alberta, Canada.

Aspinall, J., Chasmer, L., Coburn, C. A., & Hopkinson, C. (2025). Post-fire vegetation regeneration during abnormally dry years following severe montane fire: Southern Alberta, Canada. *Forest Ecology and Management*, *587*, 122750. https://doi.org/https://doi.org/10.1016/j.foreco.2025.122750

Avalanche Canada. (2024). *Avalanche Canada: Glossary*. Retrieved May 16, 2024 from https://avalanche.ca/map

Baltsavias, E. P. (1999). Airborne laser scanning: basic relations and formulas. *ISPRS Journal of Photogrammetry and Remote Sensing*, *54*(2), 199-214. https://doi.org/https://doi.org/10.1016/S0924-2716(99)00015-5

Barnes, C. (2023). *Innovations in Headwater Snow Monitoring in the Southern Canadian Rockies* University of Lethbridge]. Lethbridge, Alberta, Canada.

Barnes, C., & Hopkinson, C. (2022a). Comparing Mountain Snowpack Depth Model Results from Different Airborne Laser Scanning Flight Path Samples. *Canadian Journal of Remote Sensing*, *48*(1), 81-92. https://doi.org/10.1080/07038992.2021.1999797

Barnes, C., & Hopkinson, C. (2022b). Quality Control Impacts on Total Precipitation Gauge Records for Montane Valley and Ridge Sites in SW Alberta, Canada. *Data (Basel)*, *7*(6), 73. https://doi.org/10.3390/data7060073

Barnes, C., MacDonald, R. J., & Hopkinson, C. (2025). Montane Seasonal and Elevational Precipitation Gradients in the Southern Rockies of Alberta, Canada. *Hydrological Processes*, *39*(1), e70061. https://doi.org/https://doi.org/10.1002/hyp.70061

Baron, J. N., Gergel, S. E., Hessburg, P. F., & Daniels, L. D. (2022). A century of transformation: fire regime transitions from 1919 to 2019 in southeastern British Columbia, Canada. *Landscape Ecology*, *37*(10), 2707-2727. https://doi.org/10.1007/s10980-022-01506-9

Bhardwaj, A., Sam, L., Bhardwaj, A., & Martin-Torres, F. J. (2016). LiDAR remote sensing of the cryosphere: Present applications and future prospects [Review]. *Remote Sensing of Environment*, *177*, 125-143. https://doi.org/https://doi.org/10.1016/j.rse.2016.02.031

Bi, G., Si, G., Zhao, Y., Qi, B., & Lv, H. (2022). Haze Removal for a Single Remote Sensing Image Using Low-Rank and Sparse Prior. *IEEE Transactions on Geoscience and Remote Sensing*, *60*, 1-13. https://doi.org/10.1109/TGRS.2021.3135975

Black, P. (1991). *Watershed Hydrology*. Prentice Hall Inc.

Bladon, K. D., Emelko, M. B., Silins, U., & Stone, M. (2014). Wildfire and the Future of Water Supply. *Environmental science & technology*, *48*(16), 8936-8943. https://doi.org/10.1021/es500130g

Bright, B. C., Hudak, A. T., McCarley, T. R., Spannuth, A., Sánchez-López, N., Ottmar, R. D., & Soja, A. J. (2022). Multitemporal lidar captures heterogeneity in fuel loads and consumption on the Kaibab Plateau. *Fire Ecology*, *18*(1), 18. https://doi.org/10.1186/s42408-022-00142-7

Brockway, D. G. (1998). Forest plant diversity at local and landscape scales in the Cascade Mountains of southwestern Washington. *Forest Ecology and Management*, *109*(1), 323-341. https://doi.org/https://doi.org/10.1016/S0378-1127(98)00266-7

Broxton, P. D., Leeuwen, W. J. D. v., & Biederman, J. A. (2019). Improving Snow Water Equivalent Maps with Machine Learning of Snow Survey and Lidar Measurements. *Water Resources Research*, *55*, 3739-3757. https://doi.org/10.1029/2018WR024146

Broxton, P. D., Moeser, C. D., & Harpold, A. (2021). Accounting for Fine-scale Forest Structure is Necessary to Model Snowpack Mass and Energy Budgets in Montane Forests. *Water Resources Research*, *57*. https://doi.org/10.1029/2021WR029716

Burles, K., & Boon, S. (2011). Snowmelt energy balance in aburned forest plot, Crowsnest Pass, Alberta, Canada. *Hydrological Processes*, *25*, 3012-3029. https://doi.org/DOI: 10.1002/hyp.8067

Cameron, H. A., Schroeder, D., & Beverly, J. L. (2021). Predicting black spruce fuel characteristics with Airborne Laser Scanning (ALS). *International Journal of Wildland Fire*, *31*(2), 124-135. https://doi.org/10.1071/wf21004

Cartwright, K. A. (2018). *Spatio-Temporal Variations in Snow Depth and Associated Driving Mechanisms in a Temperate Mesoscale Mountainous Watershed* University of Lethbridge]. University of Lethbridge Library. Lethbridge, Alberta, Canada. https://opus.uleth.ca/items/305e807f-8e65-46ca-8b92-e7022ef6a7e4

Cartwright, K. A., Hopkinson, C., Kienzle, S., & Rood, S. B. (2020). Evaluation of temporal consistency of snow depth drivers of a Rocky Mountain watershed in southern Alberta. *Hydrological Processes*, *34*, 4996-5012. https://doi.org/DOI: 10.1002/hyp.13920

Chappell, C. B., & Agee, J. K. (1996). Fire Severity and Tree Seedling Establishment in Abies Magnifica Forests, Southern Cascades, Oregon. *Ecological Applications*, *6*(2), 628-640. https://doi.org/10.2307/2269397

Chasmer, L., Hopkinson, C., Petrone, R. M., & Sitar, M. (2017). Using Multitemporal and Multispectral Airborne Lidar to Assess Depth of Peat Loss and Correspondence With a New Active Normalized Burn Ratio for Wildfires: Depth of burn of peat soils using lidar. *Geophysical research letters*, *44*, 11,851-811,859. https://doi.org/10.1002/2017gl075488

Cobby, D. M., Mason, D. C., & Davenport, I. J. (2001). Image processing of airborne scanning laser altimetry data for improved river flood modelling. *ISPRS Journal of Photogrammetry and Remote Sensing*, *56*(2), 121-138. https://doi.org/https://doi.org/10.1016/S0924-2716(01)00039-9

Cunningham, C. X., Williamson, G. J., & Bowman, D. M. J. S. (2024). Increasing frequency and intensity of the most extreme wildfires on Earth. *Nature Ecology & Evolution*, *8*(8), 1420-1425. https://doi.org/10.1038/s41559-024-02452-2

Davis, R. (2012). *Modelling the Effects of Forest Disturbances on Snow Accumulation and Ablation in the Okanagan* University of Lethbridge]. Lethbridge, Alberta, Canada.

Day, T. A., DeLucia, E. H., & Smith, W. K. (1989). Influence of Cold Soil and Snowcover on Photosynthesis and Leaf Conductance in Two Rocky Mountain Conifers. *Oecologia*, *80*(4), 546-552. http://www.jstor.org.uleth.idm.oclc.org/stable/4219086

Deems, J. S., Fassnacht, S. R., & Elder, K. J. (2005). Fractal Distirbution of Snow Depth from Lidar Data. *Journal of Hydrometeorology*, *7*, 285-297.

Deems, J. S., Painter, T. H., & Finnegan, D. C. (2013). Lidar measurement of snow depth: a review. *Journal of Glaciology*, *59*(215), 467- 479. https://doi.org/doi:10.3189/2013JoG12J154

Eisenberg, C., Anderson, C. L., Collingwood, A., Sissons, R., Dunn, C. J., Meigs, G. W., Hibbs, D. E., Murphy, S., Kuiper, S. D., SpearChief-Morris, J., Little Bear, L., Johnston, B., & Edson, C. B. (2019). Out of the Ashes: Ecological Resilience to Extreme Wildfire, Prescribed Burns, and Indigenous Burning in Ecosystems [Original Research]. *Frontiers in Ecology and Evolution*, *7*. https://doi.org/10.3389/fevo.2019.00436

Ellis, T. M., Bowman, D. M. J. S., Jain, P., Flannigan, M. D., & Williamson, G. J. (2022). Global increase in wildfire risk due to climate-driven declines in fuel moisture. *Global change biology*, *28*(4), 1544-1559. https://doi.org/10.1111/gcb.16006

Fiera Biological Consulting Ltd. (2014). *Oldman Watershed Headwaters Indicator Project-Final Report*.

Flannigan, M. D., Logan, K. A., Amiro, B. D., Skinner, W. R., & Stocks, B. J. (2005). Future Area Burned in Canada. *Climatic Change*, *72*(1), 1-16. https://doi.org/10.1007/s10584-005-5935-y

Garrigues, S., Allard, D., Baret, F., & Weiss, M. (2006). Influence of landscape spatial heterogeneity on the non-linear estimation of leaf area index from moderate spatial resolution remote sensing data. *Remote Sensing of Environment*, *105*(4), 286-298. https://doi.org/https://doi.org/10.1016/j.rse.2006.07.013

Gerrand, S., Aspinall, J., Jensen, T., Hopkinson, C., Collingwood, A., & Chasmer, L. (2021). Partioning carbon losses from fire combustion in a montane Valley, Alberta, Canada. *Forest Ecology and Management*, *496*. https://doi.org/https://doi.org/10.1016/j.foreco.2021.119435

Gersh, M., Gleason, K. E., & Surunis, A. (2022). Forest Fire Effects on Landscape Snow Albedo Recovery and Decay. *Remote sensing (Basel, Switzerland)*, *14*(16), 4079. https://doi.org/10.3390/rs14164079

Giovando, J., & Niemann, J. D. (2022). Wildfire Impacts on Snowpack Phenology in a Changing Climate Within the Western U.S. *Water Resources Research*, *58*. https://doi.org/10.1029/2021WR031569

Gleason, K. E., Nolin, A. W., & Roth, T. R. (2013). Charred forests increase snowmelt: Effects of burned woody debris and incoming solar radiation on snow ablation. *Geophysical Research Letters*, *40*. https://doi.org/doi:10.1002/grl.50896,

Glenn, E. P., Huete, A. R., Nagler, P. L., & Nelson, S. G. (2008). Relationship Between Remotely-sensed Vegetation Indices, Canopy Attributes and Plant Physiological Processes: What Vegetation Indices Can and Cannot Tell Us About the Landscape. *Sensors*, *28*(8), 2136-2160. https://doi.org/ 10.3390/s8042136

Goulden, T., Hopkinson, C., Jamieson, R., & Sterling, S. (2016). Sensitivity of DEM, slope, apsect and watershed attributes to LiDAR measurement uncertainty. *Remote Sensing of Environment*, *179*, 23-35. https://doi.org/http://dx.doi.org/10.1016/j.rse.2016.03.005

Government of Alberta. (2005). *Natural Regions & Subregions of Alberta*.

Government of Alberta. (2023). *Fire Perimeter Data Standard*. Alberta Retrieved from https://open.alberta.ca/opendata/wildfire-data

Government of Alberta. (2025). *Current and Historical Alberta Weather Station Data Viewer*. https://acis.alberta.ca/weather-data-viewer.jsp

Grandpre, L. D., Gagnon, D., & Bergeron, Y. (1993). Changes in the understory of Canadian southern boreal forest after fire. *Journal of Vegetation Science*, *4*, 803-810. https://doi.org/10.2307/3235618

Grünewald, T., Schirmer, M., Mott, R., & Lehning, M. (2010). Spatial and temporal variability of snow depth and ablation rates in a small mountain catchment. *The Cryosphere*, *4*.

Grunewald, T., Stotter, J., Pomeroy, J. W., R.Dadie, Banos, I. M., Marturia, J., Spross, M., Hopkinson, C., Burlando, P., & Lehning, M. (2013). Statistical modelling of the snow depth distribution in open alpine terrain. *Hydrology and Earth System Sciences*, *17*, 3005-2021. https://doi.org/doi:10.5194/hess-17-3005-2013

Guinn, M. N. (2023). *Forest Fire Effects on Snow Storage and Melt Across Scales of Forest Recovery in the Western Oregon Cascades* (Publication Number Paper 6539) Portland State University]. Portland, Oregon, USA. https://pdxscholar.library.pdx.edu/cgi/viewcontent.cgi?article=7613&context=open_access_etds

Hopkinson, C., Barnes, C. C., Burdett, H., Craig, J. R., Rodrigues, I., MacDonald, R. J., Singer, M., Newton, B., & Van Gaalen, J. (2024, December 01, 2024). *A remote sensing-based sampling and imputation framework to model regional-scale mountain Snow Water*

Equivalent for drought mitigation AGU Fall Meeting Abstracts, Washington, D.C. https://ui.adsabs.harvard.edu/abs/2024AGUFMC21D.0375H

Hopkinson, C., Chasmer, L., Gynan, C., Mahoney, C., & Sitar, M. (2016). Multisensor and Multispectral LiDAR Characterization and Classification of a Forest Environment. *Canadian journal of remote sensing*, *42*(5), 501-520. https://doi.org/10.1080/07038992.2016.1196584

Hopkinson, C., Chasmer, L., Young-Pow, C., & Treitz, P. (2004). Assessing forest metrics with a ground-based scanning lidar [Research]. *Canadian Journal of Forest Research*, *34*(3), 573-583. https://doi.org/doi: 10.1139/X03-225

Hopkinson, C., Collins, T., Anderson, A., Pomeroy, J., & Spooner, I. (2012). Spatial Snow Depth Assessment Using LiDAR Transect Samples and Public GIS Data Layers in the Elbow River Watershed, Alberta. *Canadian Water Resources Journal / Revue canadienne des ressources hydriques*, *37*(2), 69-87. https://doi.org/10.4296/cwrj3702893

Hopkinson, C., Hayashi, M., & Peddle, D. (2008). Comparing alpine watershed attributes from LiDAR, Photogrammetric, and Contour-based Digital Elevation Models. *Hydrological Processes*, *23*, 451-463. https://doi.org/10.1002/hyp.7155

Hopkinson, C., Pietroniro, A., & Pomeroy, J. W. (2006). *Hydroscan: Airborne laser mapping of hydrological features and resources*. Environment Canada.

Hopkinson, C., Sitar, M., Chasmer, L., & Treitz, P. (2004). Mapping Snowpack Depth beneath Forest Canopies using airborne lidar. *Photogrammetric Engineering and Remote Sensing*, *70*(3), 323-330, Article 0099-1112/04/7003–0323/$3.00/0. https://doi.org/http://dx.doi.org/10.14358/PERS.70.3.323

Jain, P., Barber, Q. E., Taylor, S. W., Whitman, E., Acuna, D. C., Boulanger, Y., Chavardes, R. D., Chen, J., Englefield, P., Flannigan, M., Girardin, M. P., Thompson, D. k., Wang, X., & Parisien, M.-A. (2024). Drivers and Impacts of the Record-Breaking 2023 Wildfire Season in Canada. *Nature Communications*, *15*(6764). https://doi.org/https://doi.org/10.1038/s41467-024-51154-7

Jain, P., Castellanos-Acuna, D., Coogan, S. C., Abatzoglou, J. T., & Flannigan, M. D. (2022). Observed increases in extreme fire weather driven by atmospheric humidity and temperature. *Nature Climate Change*, *12*(1), 63-70.

Jean Louis, M., & Hiatt, M. (2025). Modelling the Effects of Vegetation Distribution and Density on Hydrological Connectivity and Water Age in a River Delta. *Ecohydrology*, *18*(2), e2741. https://doi.org/https://doi.org/10.1002/eco.2741

Keeling, C. D. (1970). Is Carbon Dioxide from Fossil Fuel Changing Man's Environment? *Proceedings of the American Philosophical Society*, *114*(1), 10-17. http://www.jstor.org/stable/985720.

Kirchner, P. B., Bales, R. C., Molotch, N. P., Flanagan, J., & Guo, Q. (2014). LiDAR measurement of seasonal snow accumulation along an elevation gradient in the southern Sierra Nevada, California. *Hydrological Earth System Science*, *18*, 4261-4275. https://doi.org/10.5194/hess-18-4261-2014

Koshkin, A. L., Hatchett, B. J., & Nolin, A. W. (2022). Wildfire impacts on western United States snowpacks. *Frontiers in water*, *4*. https://doi.org/10.3389/frwa.2022.971271

Krzic, M., Walley, F. L., Diochon, A., Pare, M. C., & Farell, R. E. (2021). *Digging into Canadian Soils: An Introduction to Soil Science*. Canadian Society of Soil Science.

Kuijt, J. (1982). *A Flora of Waterton Lakes National Park*. University of Alberta Press.

Lapp, S. L. (2002). *Climate Warming Impacts on Alpine Snowpacks in Western North America* University of Lethbridge]. Lethbridge, Alberta, Canada.

Lentile, L. B., Holden, Z. A., Smith, A. M. S., Falkowski, M. J., Hudak, A. T., Morgan, P., Lewis, S. A., Gessler, P. E., & Benson, N. C. (2006). Remote sensing techniques to assess active

fire characteristics and post-fire effects. *International Journal of Wildland Fire*, *15*, 319-345. https://doi.org/10.1071/WF05097

Letts, M. G., Nakonechny, K. N., Van Gaalen, K. E., & Smith, C. M. (2009). Physiological acclimation of Pinus flexilis to drought stress on contrasting slope aspects in Waterton Lakes National Park, Alberta, Canada [Report]. *Canadian Journal of Forest Research*, *39*, 629+. https://link-gale-com.uleth.idm.oclc.org/apps/doc/A198810314/CPI?u=leth89164&sid=summon&xid=6d1d1ca7

Lim, K., Treitz, P., Wulder, M., St-Onge, B., & Flood, M. (2003). LiDAR remote sensing of forest structure. *Progress in Physical Geography: Earth and Environment*, *27*(1), 88-106. https://doi.org/10.1191/0309133303pp360ra

Littlefield, C. E. (2019). Topography and post-fire climatic conditions shape spatio-temporal patterns of conifer establishment and growth. *Fire Ecology*, *15*(1), 34. https://doi.org/10.1186/s42408-019-0047-7

Liu, Z., Liu, K., Zhang, J., Yan, C., Lock, T. R., Kallenbach, R. L., & Yuan, Z. (2022). Fractional coverage rather than green chromatic coordinate is a robust indicator to track grassland phenology using smartphone photography. *Ecological Informatics*, *68*, 101544. https://doi.org/https://doi.org/10.1016/j.ecoinf.2021.101544

López-Moreno, J. I. (2005). Recent Variations of Snowpack Depth in the Central Spanish Pyrenees. *Arctic, Antarctic, and Alpine Research*, *37*(2), 253-260. https://doi.org/10.1657/1523-0430(2005)037[0253:RVOSDI]2.0.CO;2

Lotan, J. E., Brown, J. K., & Neuenschwander, L. F. (1985). Role of Fire in Lodgepole Pine Forest. Lodgepole pine the species and its management Symposium Procedings, Washington State University.

Lüdeke, M. K. B., Ramage, P. H., & Kohlmaier, G. H. (1996). The use of satellite NDVI data for the validation of global vegetation phenology models: application to the Frankfurt Biosphere Model. *Ecological Modelling*, *91*(1), 255-270. https://doi.org/https://doi.org/10.1016/0304-3800(95)00192-1

MacDonald, G. A. (2000). *Where the Mountains Meet the Prairies: A History of Waterton County*. University of Calgary Press.

MacDonald, M. K., Pomeroy, J. W., & Essery, R. L. H. (2018). Water and energy fluxes over northern prairies as affected by chinook winds and winter precipitation. *Agricultural and Forest Meteorology*, *248*, 372-385. https://doi.org/https://doi.org/10.1016/j.agrformet.2017.10.025

MacDonald, R. J. (2008). *Modelling the Potential Impacts of Climate Change on Snowpack in the St. Mary River Watershed, Montana* University of Lethbridge]. Lethbridge, Alberta, Canada.

Macias-Fauria, M., & Johnson, E. A. (2013). Warming-induced upslope advance of subalpine forest is severly limited by geomorphic processes. *Proceedigs of the National Academy of Sciences of the United States of America*, *110*(20), 8117-8122. https://doi.org/https://doi.org/10.1073%2Fpnas.1221278110

Mars, J. C., & Rowan, L. C. (2010). Spectral assessment of new ASTER SWIR surface reflectance data products for spectroscopic mapping of rocks and minerals. *Remote Sensing of Environment*, *114*(9), 2011-2025. https://doi.org/https://doi.org/10.1016/j.rse.2010.04.008

Marsh, C. B., Pomeroy, J. W., & Spiteri, R. J. (2012). Implications of mountain shading on calculating energy for snowmelt using unstructured triangular meshes. *Hydrological Processes*, *26*(12), 1767-1778. https://doi.org/https://doi.org/10.1002/hyp.9329

Maxwell, J., & Clair, S. B. S. (2019). Snowpack properties vary in repsonse to burn severity gradients in montane forests. *Environmental Research Letters*, *14*. https://doi.org/https://doi.org/10.1088/1748-9326/ab5de8

McCaffrey, D., & Hopkinson, C. (2020). Repeat Oblique Photography Shows Terrain and Fire-Exposure Controls on Century-Scale Canopy Cover Change in the Alpine Treeline Ecotone. *Remote Sensing*, *12*(10), 1569. https://www.mdpi.com/2072-4292/12/10/1569

McCaffrey, D. R. (2018). *Assessing Historic Change in Subalpine Forest: A case study in the west castle watershed* University of Lethbridge]. University of Lethbridge Library. Lethbridge, Alberta, Canada. https://opus.uleth.ca/items/d82a7322-dfda-4d0d-beb5-7d00d38e10ed

McGrath, D., Zeller, L., Bonnell, R., Reis, W., Kampt, S., Williams, K., Okal, M., Olsen-Mikitowicz, A., Bump, E., Sears, M., & Rittger, K. (2023). Declines in Peak Snow Water Equivalent and Elevated Snowmelt Rates Following the 2020 Cameron Peak Wildfire in Northern Colorado. *Geophysical Research Letters*, *50*. https://doi.org/10.1029/2022GL101294

Niemeyer, R. J., Bladon, K. D., & Woodsmith, r. D. (2019). Long-term hydrologic recovery after wildfire and post-fire forest management in the interior Pacific Northwest. *Hydrological Processes*, *34*, 1182-1197. https://doi.org/DOI: 10.1002/hyp.13665

Nijland, W., Jong, R. d., Jong, S. M. d., Wulder, M. A., Bater, C. W., & Coops, N. C. (2014). Monitoring plant condition and phenology using infrared sensitive consumer grade digital cameras. *Agricultural and Forest Meteorology*, *184*, 98=106. http://dx.doi.org/10.1016/j.agrformet.2013.09.007

Oard, M. J. (1993). A Method for Predicting Chinook Winds East of the Montana Rockies. *Weather and Forecasting*, *8*(2), 166-180. https://doi.org/https://doi.org/10.1175/1520-0434(1993)008<0166:AMFPCW>2.0.CO;2

Odum, E. P. (1969). The Strategy of Ecosystem Development. *Science*, *164*(3877), 262-270. http://www.jstor.org.uleth.idm.oclc.org/stable/1726720

Okhrimenko, M., & Hopkinson, C. (2019). Investigating the Consistency of Uncalibrated Multispectral Lidar Vegetation Indices at Different Altitudes. *Remote Sensing*, *11*. https://doi.org/doi:10.3390/rs11131531

Oldman Watershed Council. (2023). *Oldman Watershed Council: Explore your Watershed*. Retrieved December from https://oldmanwatershed.ca/about-the-watershed/

Parks Canada. (2023a). *Kenow Wildfire*. https://parks.canada.ca/pn-np/ab/waterton/nature/environment/feu-fire/feu-fire-kenow

Parks Canada. (2023b). *Kenow Wildfire: Waterton Lakes National Park*. Government of Canada. Retrieved March 15, 2024 from https://parks.canada.ca/pn-np/ab/waterton/nature/environment/feu-fire/feu-fire-kenow

Parks, S. A., Guiterman, C. H., Margolis, E. Q., Lonergan, M., Whitman, E., Abatzoglou, J. T., Falk, D. A., Johnston, J. D., Daniels, L. D., Lafon, C. W., Loehman, R. A., Kipfmueller, K. F., Naficy, C. E., Parisien, M.-A., Portier, J., Stambaugh, M. C., Williams, A. P., Wion, A. P., & Yocom, L. L. (2025). A fire deficit persists across diverse North American forests despite recent increases in area burned. *Nature Communications*, *16*(1), 1493. https://doi.org/10.1038/s41467-025-56333-8

Peng, D., Zhang, X., Zhang, B., Liu, L., Liu, X., Huete, A. R., Huang, W., Wang, S., Luo, S., Zhang, X., & Zhang, H. (2017). Scaling effects on spring phenology detections from MODIS data at multiple spatial resolutions over the contiguous United States. *ISPRS Journal of Photogrammetry and Remote Sensing*, *132*, 185-198. https://doi.org/https://doi.org/10.1016/j.isprsjprs.2017.09.002

Pierce, A. D., & Taylor, A. H. (2011). Fire severity and seed source influence lodgepole pine (*Pinus contorta* var. *murrayana*) regeneration in the southern Cascades, Lassen volcanic

National Park, California. *Landscape Ecology*, *26*, 225-227. https://doi.org/DOI 10.1007/s10980-010-9556-0
Pomeroy, J., & Gray, D. (1995). *Snowcover: Accumulation, Relocation, and Management* (Vol. 7). National Hydrology Research Institute. https://research-groups.usask.ca/hydrology/documents/reports/pomeroy-j.w.-and-gray-d.m._snowcover-accumulation,-relocation-and-management_book_1995.pdf
Pomeroy, J., Gray, D., Hedstrom, N., & Janowicz, J. (2002a). Physically Based Estimation of Seasonal Snow Accumulation in the Boreal Forest.
Pomeroy, J., Gray, D. M., Hedstrom, N. R., & Janowicz, J. R. (2002b). Prediction of Seasonal Snow Accumulation in Cold Climate Forests. *Hydrological Processes*, *16*(18), 3543-3558. https://doi.org/http://dx.doi.org/10.1002/hyp.1228
Pomeroy, J. W., Gray, D. M., Shook, K. R., B.Toth, Essery, R. L. H., Pietroniro, A., & Hedstrom, N. (1998). An evaluation of snow accumulation and ablation processes for land surface modelling. *Hydrological Processes*, *12*, 2339-2367. https://doi.org/https://doi.org/10.1002/(SICI)1099-1085(199812)12:15%3C2339::AID-HYP800%3E3.0.CO;2-L
Pomeroy, J. W., Parviainen, J., Hedstrom, N., & Gray, D. M. (1998). Coupled modelling of forest snow interception and sublimation. *Hydrological Processes*, *12*, 2317-2337. https://doi.org/10.1002/(SICI)1099-1085(199812)12:15%3C2317::AID-HYP799%3E3.0.CO;2-X
QGIS Project. (2024). *QGIS Documentation*. Retrieved May 16, 2024 from https://docs.qgis.org/3.34/en/docs/index.html
rapidLasso. (2024). *LAStools LiDAR processing*. https://lastools.github.io/
Reid, A. M., William K., C., Prescott, C. E., & Nijland, W. (2016). Using excess greenness and green chromatic coordinate colour indices from aerial images to assess lodgepole pine vigour, mortality and disease occurence. *Forest Ecology and Management*, *374*, 146-153. https://doi.org/http://dx.doi.org/10.1016/j.foreco.2016.05.006
RIEGL. (2021). *The Recognized Performance Leader in LIDAR*. Retrieved June 15, 2025 from https://www.rieglcanada.com/
Robinne, F.-N., Hallema, D. W., Bladon, K. D., & Buttle, J. M. (2020). Wildfire impacts on hydrologic ecosystem services in North American high-latitude forests: A scoping review. *Journal of Hydrology*, *581*, 124360. https://doi.org/https://doi.org/10.1016/j.jhydrol.2019.124360
Rother, D. E., De Sales, F., Stow, D., & McFadden, J. (2022). Impacts of burn severity on short-term postfire vegetation recovery, surface albedo, and land surface temperature in California ecoregions. *PLoS One*, *17*(11), e0274428. https://doi.org/10.1371/journal.pone.0274428
Schoennagel, T., Turner, M. G., & Romme, W. H. (2003). THE INFLUENCE OF FIRE INTERVAL AND SEROTINY ON POSTFIRE LODGEPOLE PINE DENSITY IN YELLOWSTONE NATIONAL PARK. *Ecology*, *84*(11), 2967-2978. https://doi.org/https://doi.org/10.1890/02-0277
Silins, U., Stone, M., Emelko, M. B., & Bladon, K. D. (2009). Sediment production following severe wildfire and post-fire salvage logging in the Rocky Mountain headwaters of the Oldman River Basin, Alberta. *CATENA*, *79*(3), 189-197. https://doi.org/https://doi.org/10.1016/j.catena.2009.04.001
Smoot, E. E., & Gleason, K. E. (2021). Forest Fires Reduce Snow-Water Storage and Advance the Timing of Snowmelt across the Western U.S. *Water*, *13*(24), 3533. https://www.mdpi.com/2073-4441/13/24/3533
Soininen, A. (2023). *TerraScan User Guide*. Terrssolid ltd. https://www.terrasolid.com/guides/tscan/index.html

Springer, J., Ludwig, R., & Kienzle, S. W. (2015). Impacts of Forest Fires and Climate Variability on the Hydrology of an Alpine Medium Sized Catchment in the Canadian Rocky Mountains. *Hydrology*, *2*, 23-47. https://doi.org/doi:10.3390/hydrology2010023

St-Onge, B. A., & Achaichia, N. (2001). Measuring Forest Canopy Height using a Combination of Lidar and Aerial Photogrpahy Data. *International Archieves of Photogrammetry and Remote Sensing*, *34*(3). https://www.isprs.org/proceedings/xxxiv/3-w4/pdf/stonge.pdf

Teledyne Optech. (2023). *Optech Titan Multispectral Lidar System*. www.teledyneoptech.com

Terrasolid Inc. (2024). *TerraScan*. In https://terrasolid.com/

Thomas, M. E. (1987). INFRARED AND MILLIMETER-WAVELENGTH ABSORPTION BY ATMOSPHERIC WATER-VAPOR. *Johns Hopkins APL technical digest*, *8*(4), 363-369. https://go.exlibris.link/ChGPY1PT

Thompson, J. C., & Moore, R. D. (1996). RELATIONS BETWEEN TOPOGRAPHY AND WATER TABLE DEPTH IN A SHALLOW FOREST SOIL. *Hydrological Processes*, *10*(11), 1513-1525. https://doi.org/https://doi.org/10.1002/(SICI)1099-1085(199611)10:11<1513::AID-HYP398>3.0.CO;2-V

Tinkham, W. T., Smith, A. M. S., Hans-Peter Marshall, Link, T. E., Falkowski, M. J., & Winstral, A. H. (2014). Quantifying spatial distribution of snow depth errors from LiDAR using Random Forest. *Remote Sensing of the Environment*, *141*, 105-115. https://doi.org/http://dx.doi.org/10.1016/j.rse.2013.10.021

Turner, M. G., Romme, W. H., Gardner, R. H., & Hargrove, W. W. (1997). Effects of Fire Size and Pattern on Early Succession in Yellowstone National Park. *Ecological Monographs*, *67*(4), 411-433. https://doi.org/10.2307/2963464

Van Gaalen, J., Barnes, C., Aslami, F., Ohkrimenko, M., Rodrigues, I., & Hopkinson, C. (2024). *How Much Water is in the Snow?* University of Lethbridge. https://storymaps.arcgis.com/stories/9a25f62241d745468d6b4e9e67d6395d

Vionnet, V., Marsh, C. B., Menounos, B., Gascoin, S., Wayand, N. E., Shea, J., Mukherjee, K., & Pomeroy, J. W. (2021). Multi-scale snowdrift-permitting modelling of mountain snowpack [Article]. *Cryosphere*, *15*(2), 743-769. https://doi.org/10.5194/tc-15-743-2021

Wehr, A., & Lohr, U. (1999). Airborne laser scanning—an introduction and overview. *ISPRS Journal of Photogrammetry and Remote Sensing*, *54*(2), 68-82. https://doi.org/https://doi.org/10.1016/S0924-2716(99)00011-8

Williams, C. H. S., Silins, U., Spencer, S. A., Wagner, M. J., Stone, M., & Emelko, M. B. (2019). Net precipitation in burned and unburned subalpine forest stands after wildfire in the northern Rocky Mountains. *International Journal of Wildland Fire*, *28*, 750-760. https://doi.org/10.1071/WF18181

Woebbecke, D. M., Meyer, G. E., Vonbargen, K., & Mortensen, D. A. (1995). Color Indexes for Weed Identification Under Various Soil, Residue, and Lighting Conditions. *American Society of Agricultural Engineers*, *38*(1), 259-269.

Wyszecki, G., & Stiles, W. S. (1967). Colorimetry. In *Color Science: Concepts and Methods, Quantative Data and Formulas* (1 ed., Vol. 1, pp. 228-370). John Wiley and Sons, Inc.

Yousefi, S., Pourghasemi, H. R., Emami, S. N., Pouyan, S., Eskandari, S., & Tiefenbacher, J. P. (2020). A machine learning framework for multi-hazards modeling and mapping in a mountainous area. *Scientific Reports*, *10*(1), 12144. https://doi.org/10.1038/s41598-020-69233-2

Zou, L., Tian, F., Liang, T., Eklundh, L., Tong, X., Tagesson, T., Dou, Y., He, T., Liang, S., & Fensholt, R. (2023). Assessing the upper elevational limits of vegetation growth in global high-mountains. *Remote Sensing of Environment*, *286*, 113423. https://doi.org/https://doi.org/10.1016/j.rse.2022.113423

Appendix A: Additional Field Data

The results of chapter 2 show that the field data is critical for providing the base information for the fractional cover prediction. The field plots were collected each summer from 2019 to 2024, in 4 different sites, and included field photos and height measurements. Figures A and B show the field plot data collected for each site in each year. These data are interesting for comparing differences between sites and for further understanding at the local scale of post-fire vegetation regeneration. These results also continue on some of the work presented in Aspinall, et al., (2025), where the moist and dry site were compared, and biomass models were generated in the first 4 years post fire.

Between 2018 and 2024, in-situ vegetation showed significant increases in greenness at all sites (Figure A, K-W test $p<0.05$). The most growth was observed in the moist site, and the least growth was observed in the slope sites. Greenness in the GCC tests reaches a saturation point after 5 years in the moist site, at which point GCC is not significantly different from the year prior. In the dry site, GCC saturates after seven years. The slope sites showed an increasing trend in growth over time but did not show a significant difference in the means and variance between 2023 and 2024. Since there is only two years of data within these sites, it is not yet possible to draw a conclusive result on vegetation growth rates in these sites based solely on the field vegetation data.

Height measurements demonstrated a significant increase in vegetation between 2018 and 2024 at the moist and dry sites (KW test $p<0.05$; Figure B). All sites had increasing variance over time, as some seedlings increased in height to a maximum of 2.1m tall, while most herbaceous and small seedlings were below 0.5m tall. While the height was observed to have a significant difference between 2018 and 2024 for the moist and dry sites, individual MW tests between specific years did not give a conclusive measure of vegetation recovery rates within the early post-fire timeframe observed ($p>0.05$), due to the high variance in the vegetation species, meteorological conditions from year-to-year, and the high variance in the herbaceous growth which changes year-to-year.

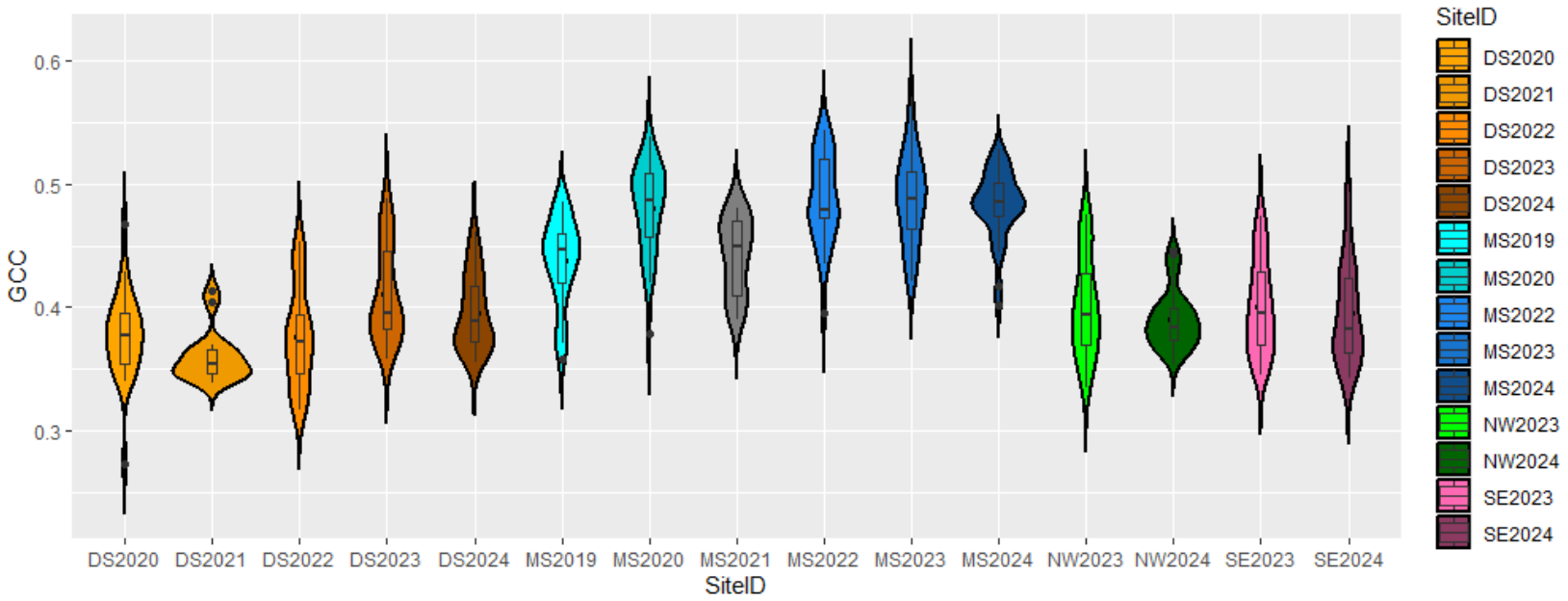

Figure A: The GCC of the field plots represented as violin plots for each year and site measured. The first two letters of the Site ID refer to the site location, and the four numbers refer to the survey year.

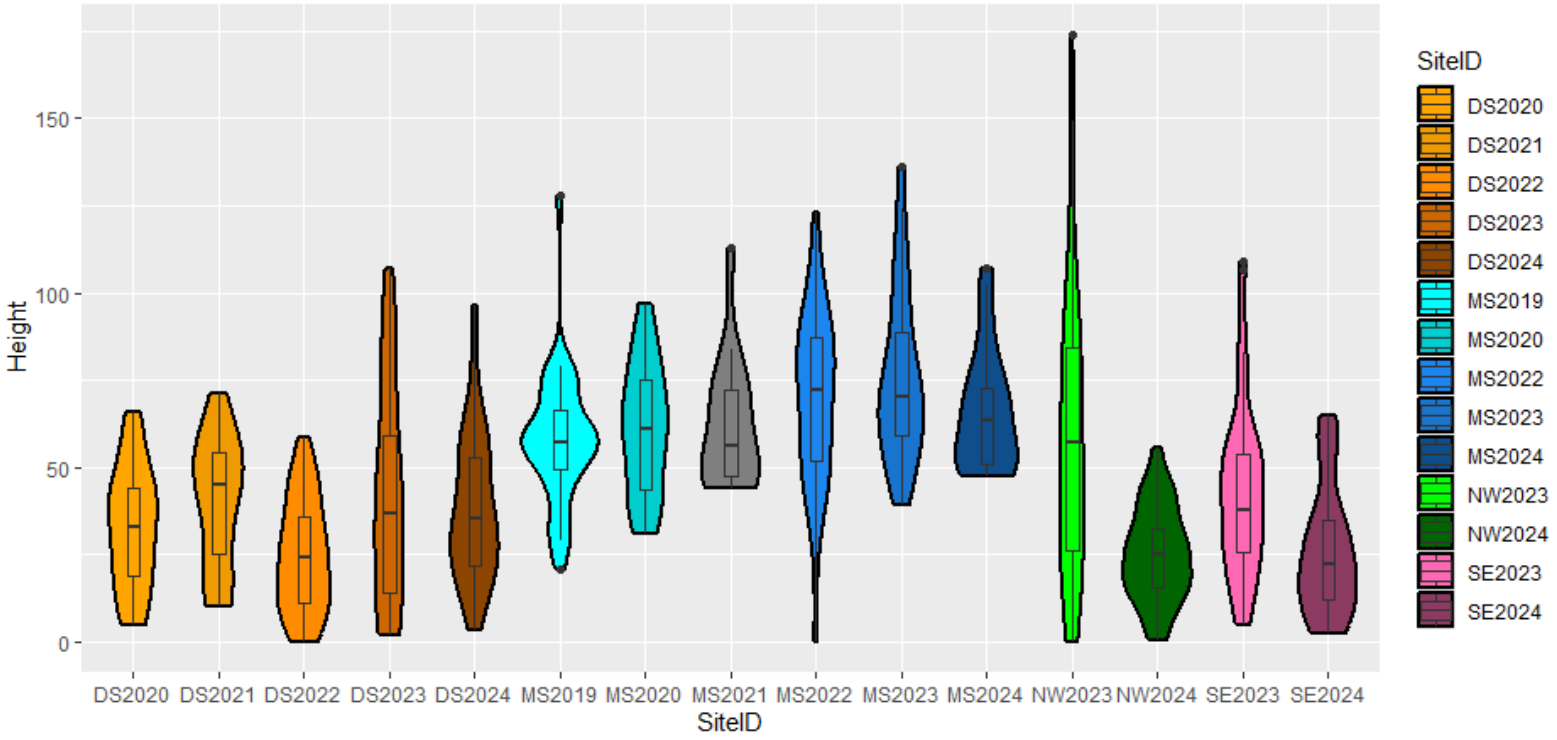

Figure B: The mean vegetation height of the field plots represented as violin plots for each year and site measured. The first two letters of the Site ID refer to the site location, and the four numbers refer to the survey year.

Similarly to the field data presented, the RPAS data showing the change over time in greenness and height for each of the surveyed RPAS polygons showed the same trends as the in-situ data, with the moist site increasing in vegetation cover faster than any other site, but with all sites demonstrating a growth trend, all with Pearson's Coefficients of over 0.80 (Figure C). The mean of the CHMs for each RPAS survey polygon over time show some increase in height over time between 2018 and 2024, but overall, there is no statistically significant increase from year to year across the sites (Figure D). Three of the four sites show a positive trendline indicating a general increase in vegetation height, however, the SES shows a negative trendline, indicating a loss in vegetation height. The MS again shows the most growth and most reliable model, with an r^2 of 0.38.

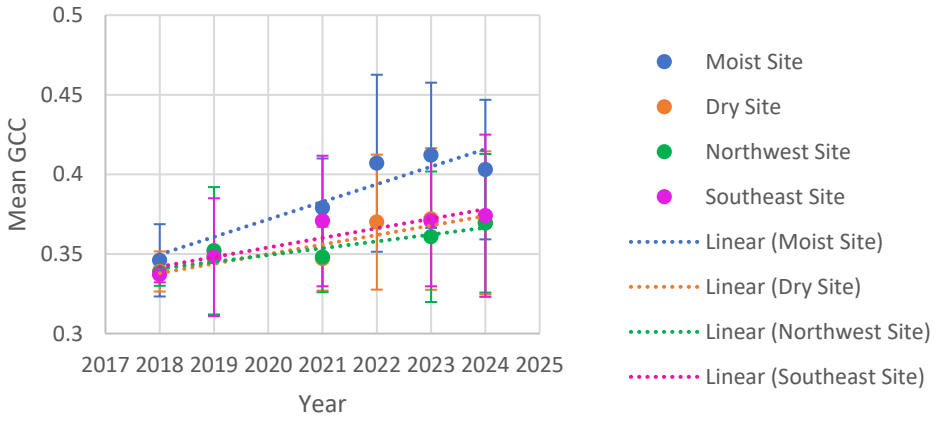

Figure C: RPAS plot regressions showing mean GCC over time for each of the survey polygons, error bars are standard deviation. The coefficients of determination for each site were: MS: r^2=0.86, DS: r^2=0.81, NWS: r^2=0.83. and SES: r^2=0.86.

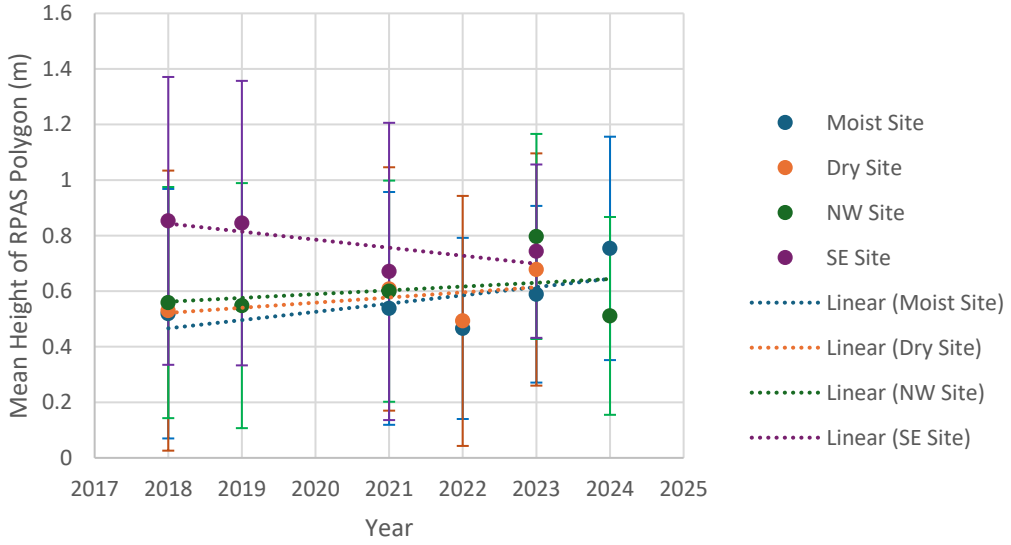

Figure D: RPAS plot regressions showing the mean vegetation height over time for each of the survey polygons, error bars are standard deviation. The coefficients of determination for each site were: MS: r^2=0.38, DS: r^2=0.23, NWS: r^2=0.09. and SES: r^2=0.54.

Appendix B: Humidity Impacts on the Active Normalized Burn Ratio derived from Multispectral Lidar

Multispectral lidar is a very useful tool for understanding changes on the Earth's surface, because it can capture both structural and spectral aspects of the environment. The combination of laser wavelengths can be used to develop spectral indices, as is discussed in chapters 2 and 3. However, like any other optical spectral index, the lasers light is affected by atmospheric components from the day, time, and location when the data is collected (Bi et al., 2022). Atmospherics, such as water vapour, smoke particulates, and pollution, can significantly attenuate certain wavelengths of the electromagnetic spectrum. For example, ozone tends to block ultraviolet wavelengths, and water vapour attenuates short wave infrared (SWIR) wavelengths (Thomas, 1987).

In the case of the active normalized burn ratio (aNBR), derived from ratioing the near infrared (NIR) laser intensity response at 1064nm and the SWIR laser intensity response at 1550nm, if either of those bands are impacted by the atmospheric conditions, predictions of vegetation cover could be inflated or repressed. This is observed in the 2019 flights over Cameron Valley and Lynx Creek. In these locations, the aNBR mean was observed to be approximately 10-15% higher than expected based on the years prior and following (Chapter 2). While Lynx Creek alone the abnormality could possible be attributed to the vegetation and hydro climatological conditions of the year, the response in Cameron Valley suggested that in 2019, the valley was fully covered in vegetation as though it had not burned. Field experience and RPAS imagery demonstrated that this was not the case, and the valley was expected to take several years to recover following the 2017 fire. Therefore, this 10% offset in the lidar data had to be caused by something in the system itself, or with the atmospheric conditions. The lidar system (Teledyne Optech's "Titan") was functioning properly, as the other datasets collected before and after 2019 in the summer, as well as the snow data, seemed to be responding as expected. Therefore, the problem was attributed to atmospheric conditions.

The two most likely atmospheric conditions that could cause problems in the summer in this region were wildfire smoke and humidity. Wildfire smokes is a combination of many types of atmospheric compounds, including particulate matter of different sizes, nitrous oxides, carbon dioxide, sulfur oxides, and other various chemicals. However, limited information was available regarding historical air quality conditions related to smoke for rural areas in Alberta. There was information available from Alberta Environment and Parks (Government of Alberta, 2025) regarding current and historical weather conditions as measured by their network of meteorological stations across the province. Three stations are within a 100km radius of Cameron Valley, each of which reports the air temperature and relative humidity, which are two conditions that we are interested in which can affect the laser pathways. The weather data for the days of the flights for each year and the days before and after were extracted and graphed, as shown in Figure B1 below.

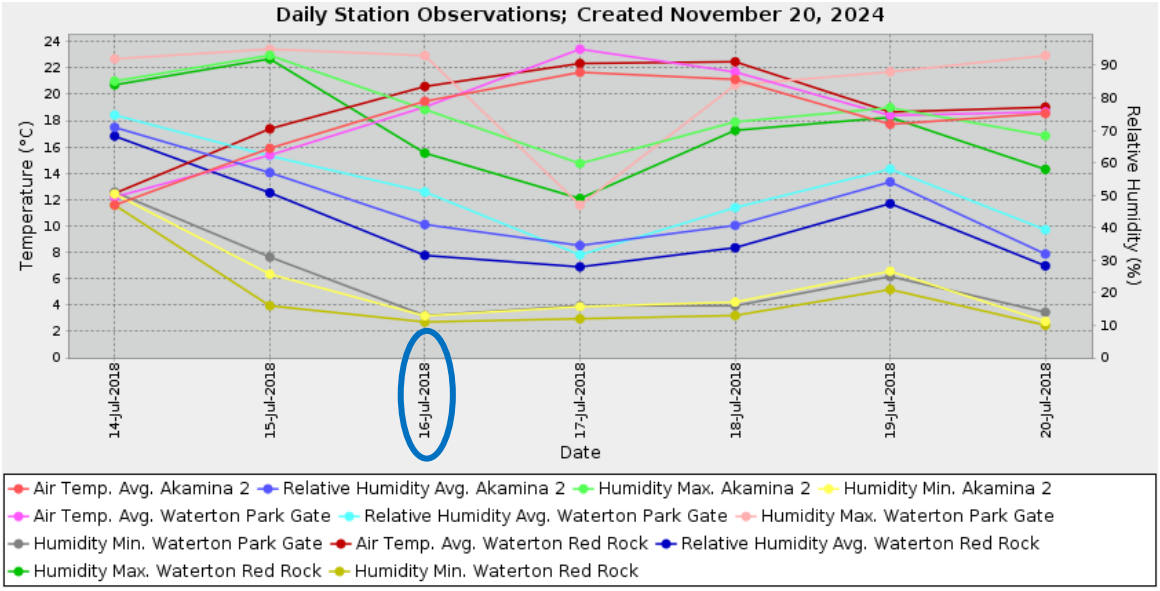
Daily Station Observations; Created November 20, 2024
Temperature (°C)
Relative Humidity (%)
14-Jul-2018
15-Jul-2018
16-Jul-2018
17-Jul-2018
18-Jul-2018
19-Jul-2018
20-Jul-2018
Date
Air Temp. Avg. Akamina 2
Relative Humidity Avg. Akamina 2
Humidity Max. Akamina 2
Humidity Min. Akamina 2
Air Temp. Avg. Waterton Park Gate
Relative Humidity Avg. Waterton Park Gate
Humidity Max. Waterton Park Gate
Humidity Min. Waterton Park Gate
Air Temp. Avg. Waterton Red Rock
Relative Humidity Avg. Waterton Red Rock
Humidity Max. Waterton Red Rock
Humidity Min. Waterton Red Rock

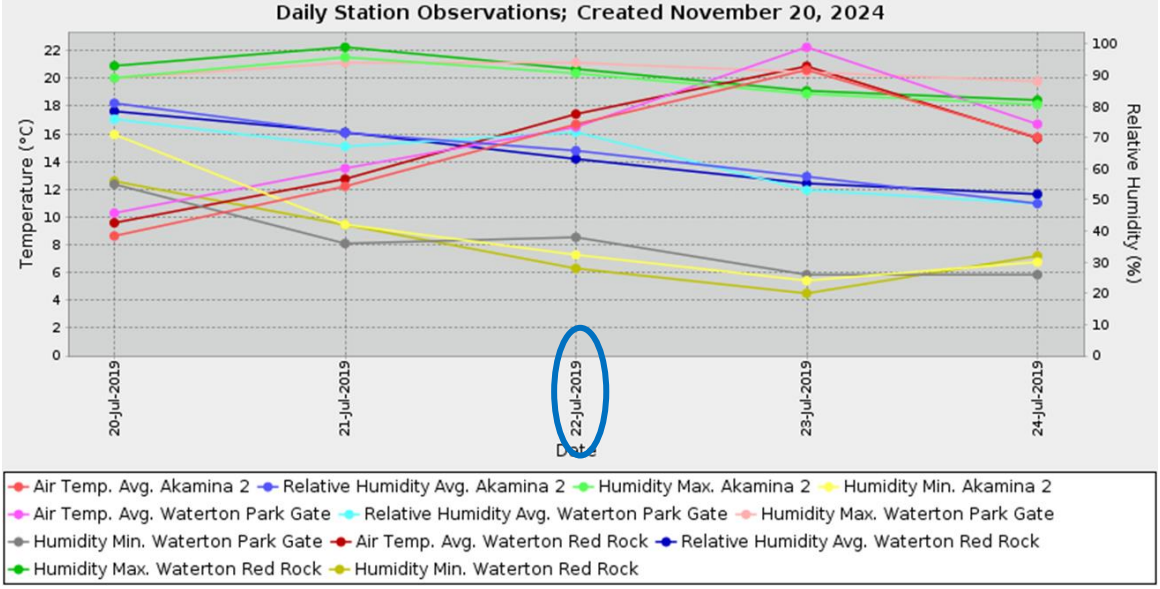
Daily Station Observations; Created November 20, 2024
Temperature (°C)
Relative Humidity (%)
20-Jul-2019
21-Jul-2019
22-Jul-2019
23-Jul-2019
24-Jul-2019
Date
Air Temp. Avg. Akamina 2
Relative Humidity Avg. Akamina 2
Humidity Max. Akamina 2
Humidity Min. Akamina 2
Air Temp. Avg. Waterton Park Gate
Relative Humidity Avg. Waterton Park Gate
Humidity Max. Waterton Park Gate
Humidity Min. Waterton Park Gate
Air Temp. Avg. Waterton Red Rock
Relative Humidity Avg. Waterton Red Rock
Humidity Max. Waterton Red Rock
Humidity Min. Waterton Red Rock

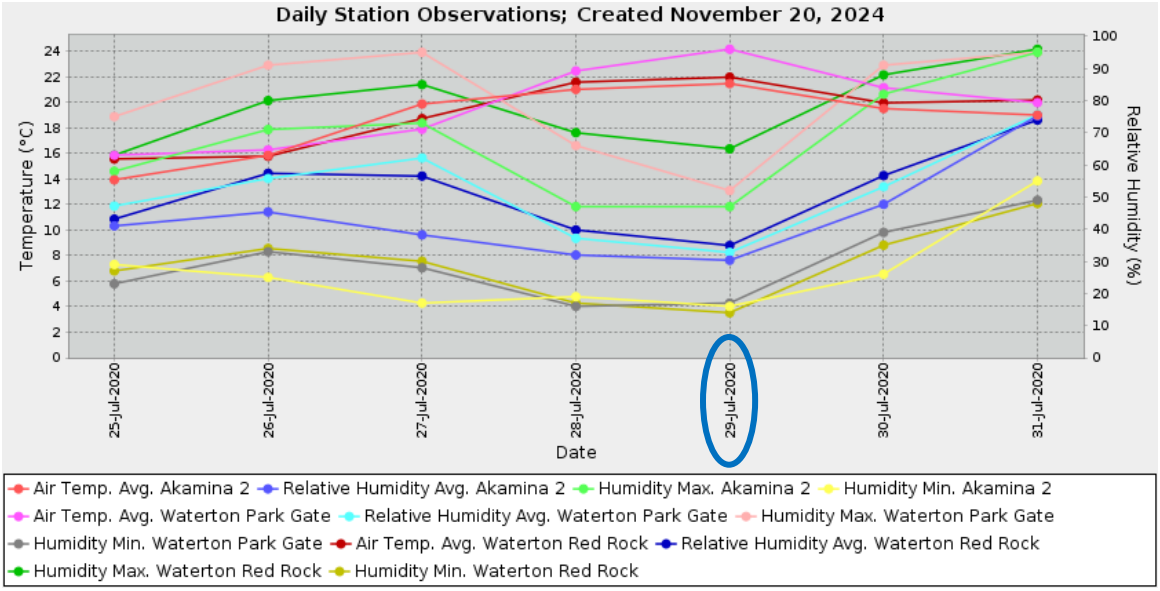
Daily Station Observations; Created November 20, 2024
Temperature (°C)
Relative Humidity (%)
25-Jul-2020
26-Jul-2020
27-Jul-2020
28-Jul-2020
29-Jul-2020
30-Jul-2020
31-Jul-2020
Date
Air Temp. Avg. Akamina 2
Relative Humidity Avg. Akamina 2
Humidity Max. Akamina 2
Humidity Min. Akamina 2
Air Temp. Avg. Waterton Park Gate
Relative Humidity Avg. Waterton Park Gate
Humidity Max. Waterton Park Gate
Humidity Min. Waterton Park Gate
Air Temp. Avg. Waterton Red Rock
Relative Humidity Avg. Waterton Red Rock
Humidity Max. Waterton Red Rock
Humidity Min. Waterton Red Rock

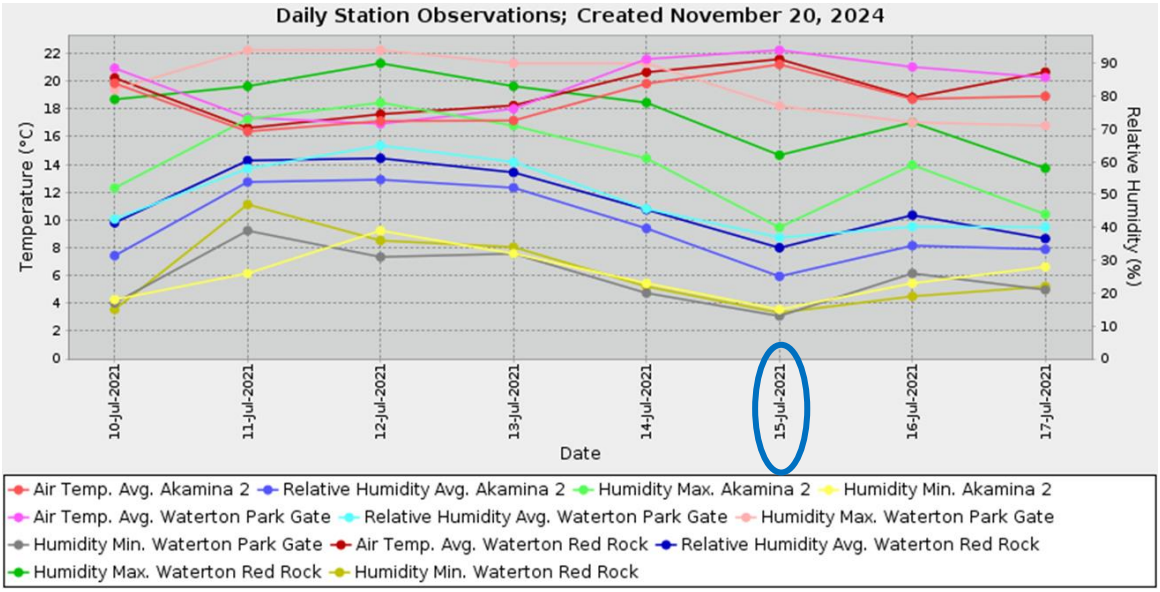
Daily Station Observations; Created November 20, 2024
Temperature (°C)
Relative Humidity (%)
10-Jul-2021
11-Jul-2021
12-Jul-2021
13-Jul-2021
14-Jul-2021
15-Jul-2021
16-Jul-2021
17-Jul-2021
Date
Air Temp. Avg. Akamina 2
Relative Humidity Avg. Akamina 2
Humidity Max. Akamina 2
Humidity Min. Akamina 2
Air Temp. Avg. Waterton Park Gate
Relative Humidity Avg. Waterton Park Gate
Humidity Max. Waterton Park Gate
Humidity Min. Waterton Park Gate
Air Temp. Avg. Waterton Red Rock
Relative Humidity Avg. Waterton Red Rock
Humidity Max. Waterton Red Rock
Humidity Min. Waterton Red Rock

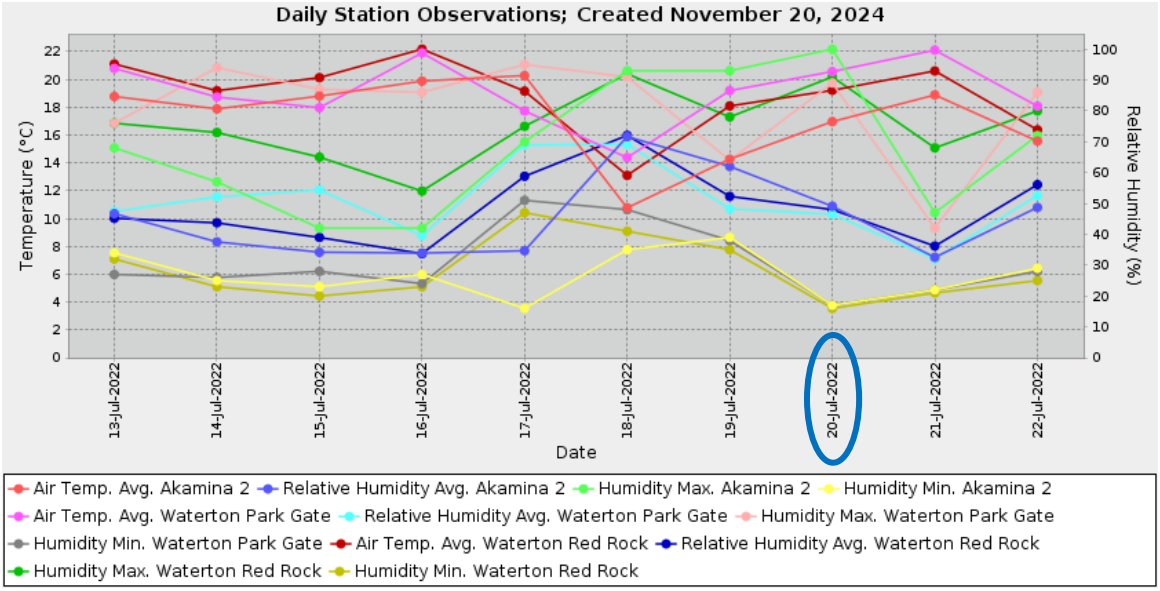
Daily Station Observations; Created November 20, 2024
Temperature (°C)
Relative Humidity (%)
Date
13-Jul-2022
14-Jul-2022
15-Jul-2022
16-Jul-2022
17-Jul-2022
18-Jul-2022
19-Jul-2022
20-Jul-2022
21-Jul-2022
22-Jul-2022
Air Temp. Avg. Akamina 2
Relative Humidity Avg. Akamina 2
Humidity Max. Akamina 2
Humidity Min. Akamina 2
Air Temp. Avg. Waterton Park Gate
Relative Humidity Avg. Waterton Park Gate
Humidity Max. Waterton Park Gate
Humidity Min. Waterton Park Gate
Air Temp. Avg. Waterton Red Rock
Relative Humidity Avg. Waterton Red Rock
Humidity Max. Waterton Red Rock
Humidity Min. Waterton Red Rock

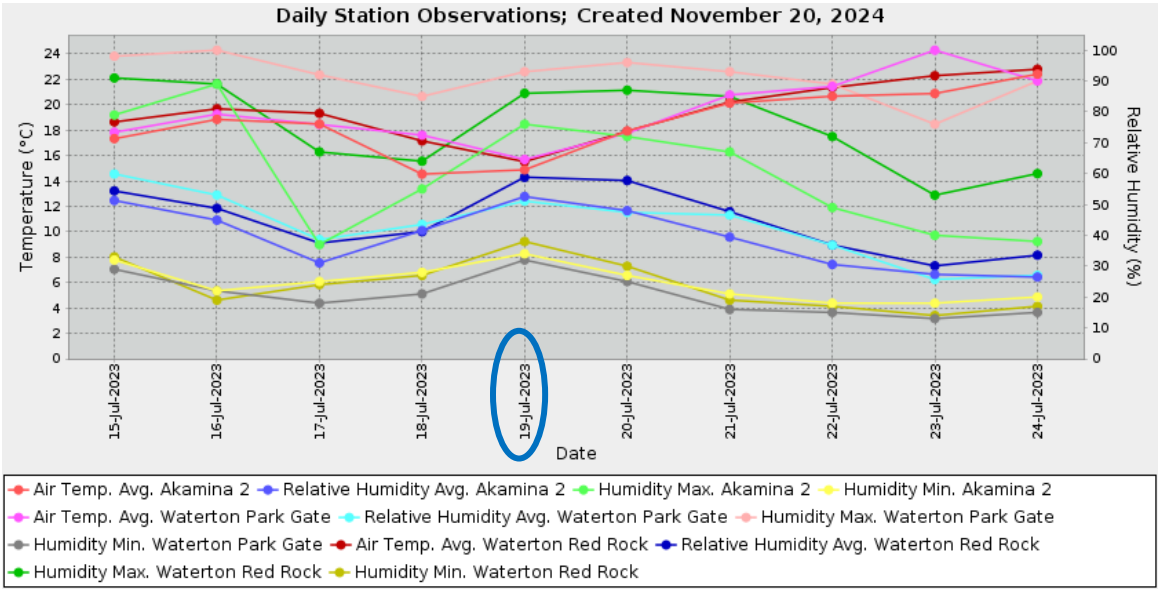
Daily Station Observations; Created November 20, 2024
Temperature (°C)
Relative Humidity (%)
Date
15-Jul-2023
16-Jul-2023
17-Jul-2023
18-Jul-2023
19-Jul-2023
20-Jul-2023
21-Jul-2023
22-Jul-2023
23-Jul-2023
24-Jul-2023
Air Temp. Avg. Akamina 2
Relative Humidity Avg. Akamina 2
Humidity Max. Akamina 2
Humidity Min. Akamina 2
Air Temp. Avg. Waterton Park Gate
Relative Humidity Avg. Waterton Park Gate
Humidity Max. Waterton Park Gate
Humidity Min. Waterton Park Gate
Air Temp. Avg. Waterton Red Rock
Relative Humidity Avg. Waterton Red Rock
Humidity Max. Waterton Red Rock
Humidity Min. Waterton Red Rock

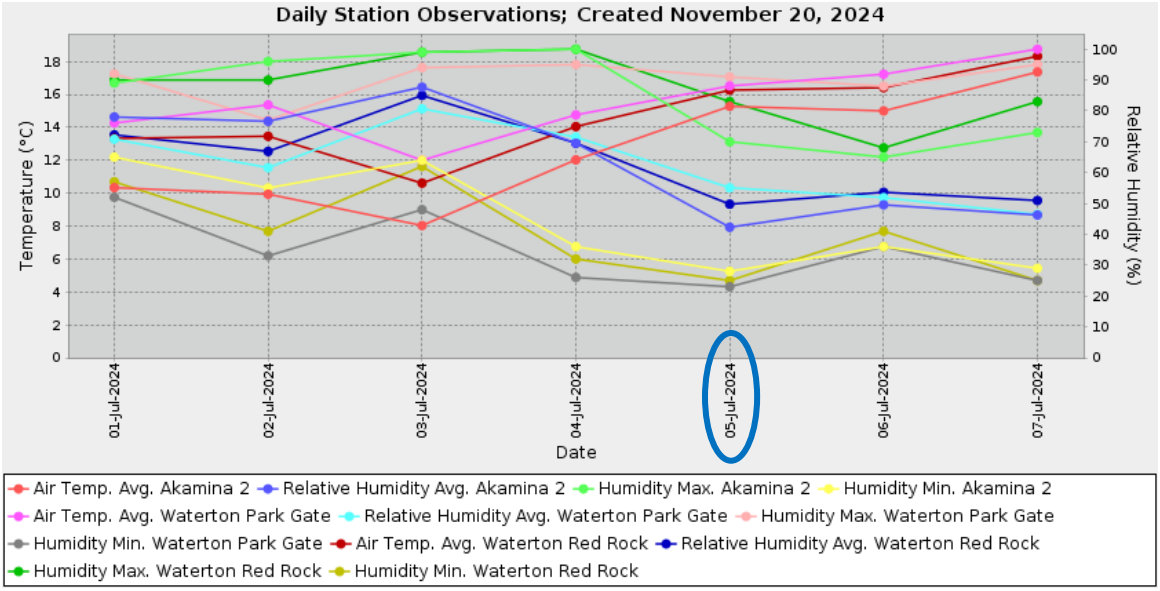

Figure E: The weather data from the Government of Alberta website (https://acis.alberta.ca/weather-data-viewer.jsp) for the flight dates (circled in blue) and surrounding dates for each survey, showing the air temperature and humidity for three local stations around the survey area.

It can be noted that in 2019, the mean relative humidity on the date of the flight is around 60%, while every other flight date has a relative humidity between 35 and 50%, making the 2019 relative humidity a minimum of 10% higher than any other survey. Relative humidity describes the amount of water vapour in the air relative to air temperature. Therefore, a higher relative humidity at the same temperature, as each flight occurs between 17°C and 22°C based on the closest weather station (Akamina 2), suggests a higher concentration of atmospheric water vapour. One of the atmospheric particulates that most interferes with the SWIR channel region is water vapour, and therefore, if this channel is attenuated, the normalized difference equation will return higher values, as a smaller intensity response will be recorded in the SWIR channel compared to the NIR channel.

This difference was accounted for by multiplying the aNBR by 1.1, to account for the approximately 10% attenuation in the SWIR channel. While still imperfect, this correction factor brings the 2019 datasets to a more comparable and correct form for analysing spatiotemporal change in the burned areas of Cameron Valley. This correction likely can be further improved with a laboratory analysis of the impacts of humidity on the sensor response, however, since the environment is highly variable in which the data was collected, this correct works well enough to reduce the error in the datasets and in the eventual vegetation cover change analysis presented in chapters 2 and 3.

Appendix C: Alternate Fractional Cover Modelling Methods and Results

Chapter 2 of this thesis discusses a method of transferring vegetation cover models from field to airborne scales using equations relating greenness to fractional cover. This method works for as it addresses the mixed pixel effect at each scale. However, even with all possible controls in place, there is still some effect from mixed pixels and from annual environmental impacts, resulting in a noisy model at best. Therefore, independent validations of the results based on different methods are presented here, to show that while the environment is highly variable, there are multiple potential ways of presenting and predicting the same results in this post-fire mountainous valley.

The first alternate method is referred to as the binary thresholding method. This method starts out the same way as presented in chapter 2, with using the binary threshold of GCC to determine the proportion of the 1m area photo that is green or not-green, thereby determining the fractional cover. The GCC and Fcov were related logarithmically as this is the relationship which best fit the data statistically, as shown in figure 2.9.

The method changes at the RPAS scale, as a binary threshold of GCC =0.37 was set based on a manual sensitivity analysis, so all values below the threshold at the 2cm grid cell were determined to have no cover and above had some amount of cover greater than 0%. The 2cm binary raster was then aggregated to 1m using the mean, to generate a percentage of Fcov over the 1m area, to compare with the field data using nearest neighbour.

At the airborne scale, the aNBR was generated at 1m grid cell, which did leave significant gaps in the data due to variance in density due to flying height, data density, and overlap. Endmember analysis which used the zonal statistics over 20 sites each of known vegetated and non-vegetated areas allowed for the determination of a threshold point at -0.499. Pixels below this value were set to zero and above were set to 1. The binary raster was aggregated to 5m (combination of 25 pixels) to generate a percent Fcov at the airborne scale. The resulting comparison between RPAS Fcov and airborne lidar Fcov over a 5m scale as generated by the binary threshold method is demonstrated in Figure E. While very noisy as expected, the equation through the data gives a reasonable spatial model of vegetation regeneration, which is comparable to those presented in chapters 2 and 3.

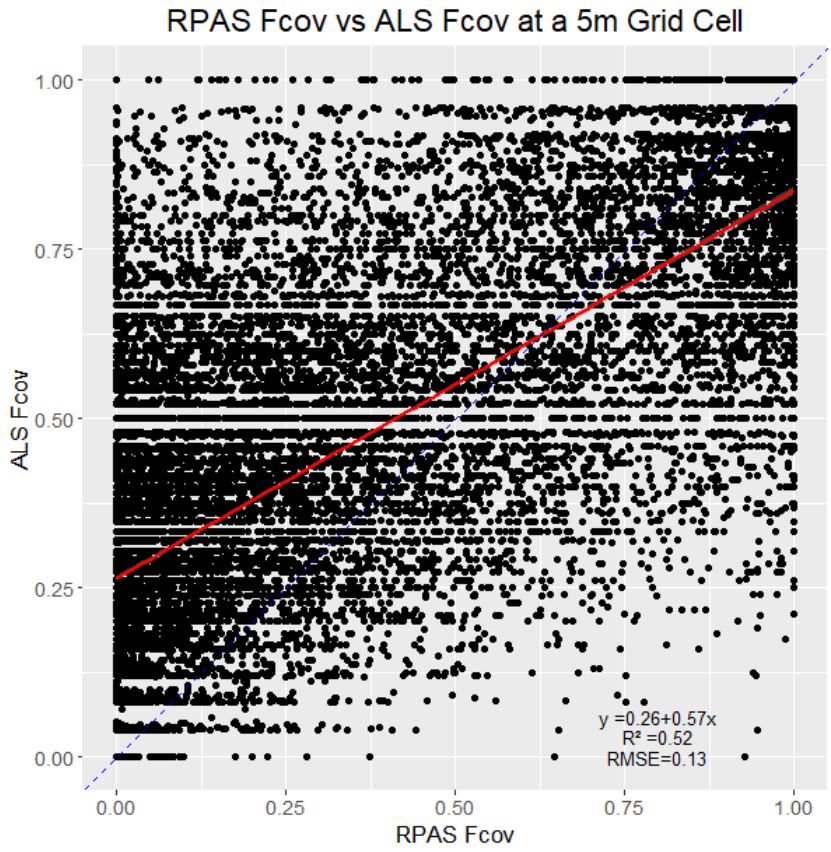

Figure F: The resulting comparison of RPAS Fcov and airborneR Fcov over a 5m grid cell.

In addition to the grid cell mathematical models, zonal models were developed over RPAS survey areas (or 'zones', figure 2.2 in Chapter 2) to compare fractional cover and height between zones that represented different environmental conditions. To measure vegetation cover and height over a consistent zone at each scale, the mean GCC, Fcov, and height of all of the annual field plots in the respective RPAS survey polygon was calculated to describe regional change from year to year at the field scale. For the RPAS scale, the mean GCC, Fcov, and height values of the survey zones were compared from year to year. The airborne lidar data were clipped to the extent of the survey zones and the descriptive statistics of the aNBR and the CHM were calculated for inter-annual comparison. Linear regression analysis was run on these zonal comparisons, between field and RPAS, then RPAS and airborne lidar, as it is expected that these scales are directly related. The regressions comparing the zonal height models between scales are presented in Figure F, and the regressions comparing the greenness and cover of each scale are presented in Figure G.

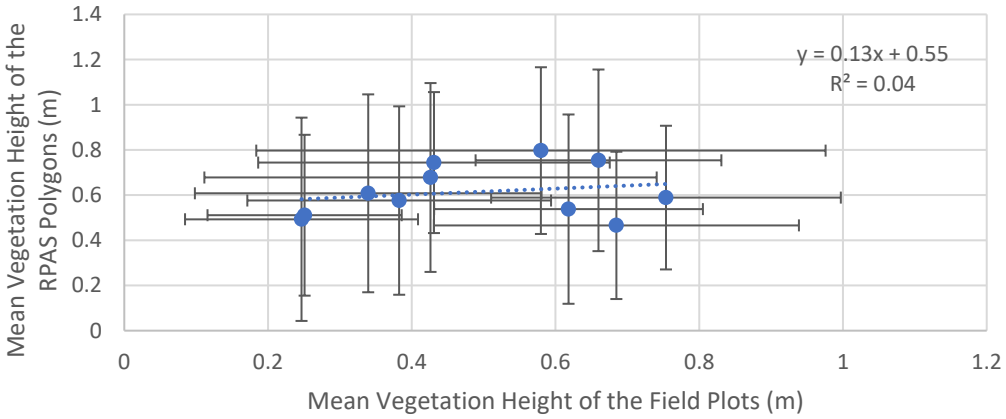

1)

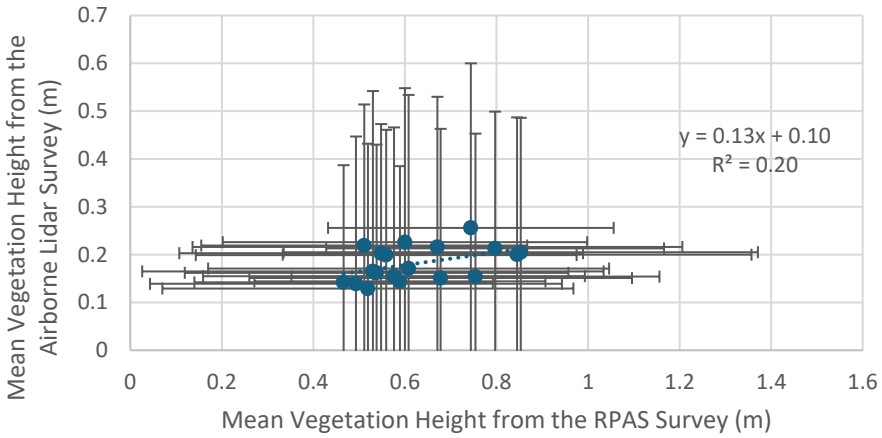

2)

Figure G: 1) The comparison of the mean field plot height measurements in each RPAS polygon and the mean of the associated RPAS CHM, and 2) the mean of the RPAS CHM surveys, compared to the mean of the airborne CHM over the same associated areas for zonal height comparisons.

Height was not effective as a transferrable model over the zonal areas, which supports the results presented in chapter 2, where structural lidar features are not effective in the early stages of post-fire regeneration. However, it is expected that these results will also improve as the woody vegetation begins to dominate the region in the next 5 to 10 years.

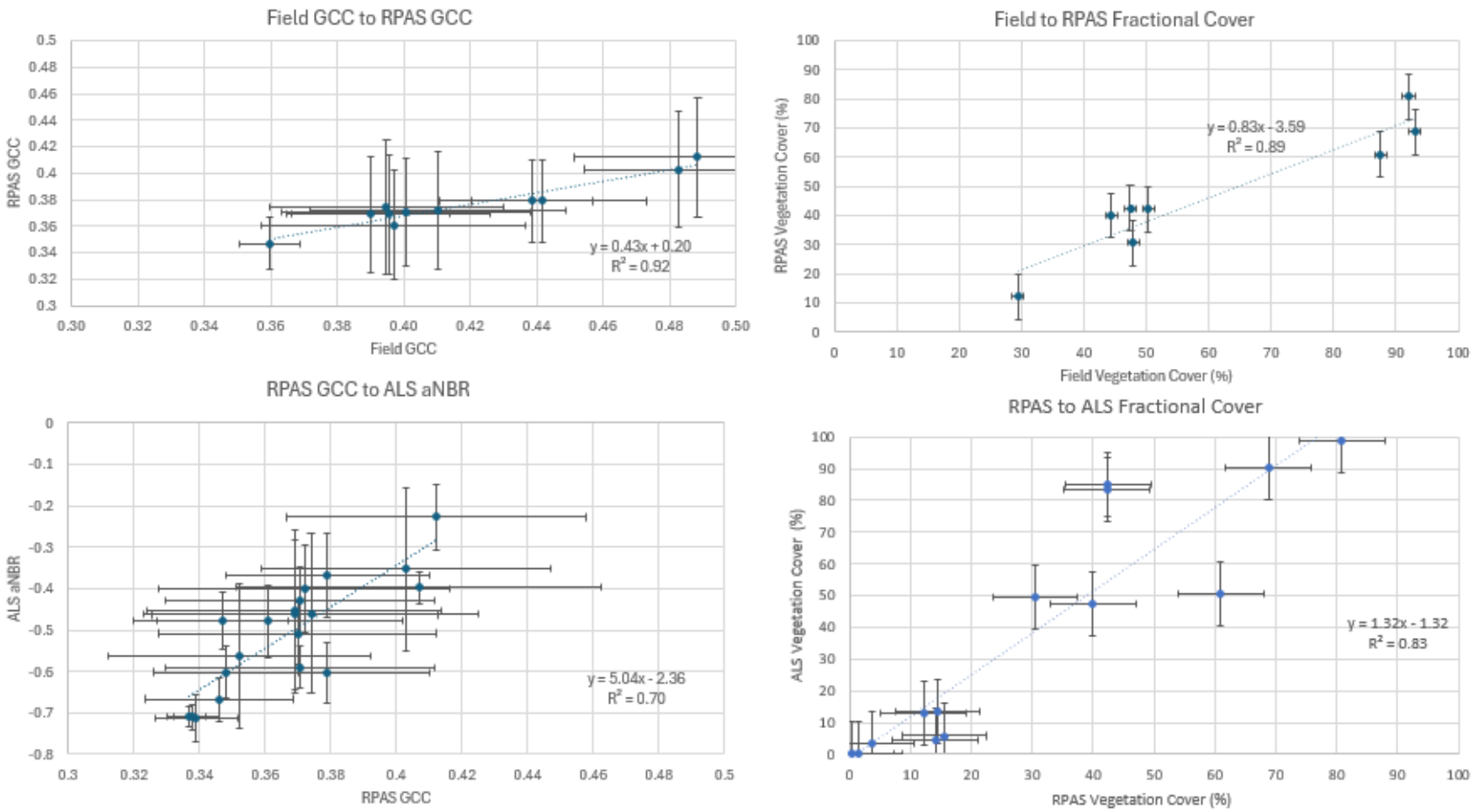

Figure H: The regression models between each scale of data over the RPAS polygon zones, comparing the mean values of greenness and cover to determine whether measurements can be scaled up on the zonal scale, comparing i) field GCC to RPAS GCC (r^2=0.92), ii) field cover to RPAS cover (r^2=0.89), iii) RPAS GCC to aNBR (r^2=0.70) and iv) RPAS cover to airborne lidar cover (r^2=0.83)

Overall, the zonal statistics of the field and RPAS GCC were correlated (Figure F.1, r^2 =0.86), showing that the greenness can be upscaled at the zonal area scale, based on the mean values of the GCC for each site for each year. The same pattern followed for the Fcov models derived from greenness over the RPAS zones (Figure F.2, r^2=0.89). The mean RPAS GCC and the aNBR were also significantly correlated (Figure F.3, r^2 =0.70), as were the RPAS and airborne lidar Fcov (Figure F.4, r^2 =0.83). Therefore, to upscale from field plots to airborne measurements of Fcov at the zonal comparison area, the equation system is presented in Equation A.

Equation A: The system of equations for converting from greenness to Fcov from field to airborne scales over the RPAS zone:

$$\text{Field (Fcov)} = 2.08\text{Ln(FieldGCC)}+2.43$$

$$\text{RPAS Fcov} =0.83\text{(FieldFcov)}-3.59$$

$$\text{Airborne Lidar Fcov} = 1.32\text{(RPAS Fcov)}-1.32$$